Politecnico di Milano

PhD Dissertation

Turbulence skin-friction reduction by traveling waves: a DNS study

---

PhD Candidate:
Wenxuan Xie

Advisor:
Prof. Maurizio Quadrio

Preface

Vehicles traveling in air or water, such as planes, cars or submarines, experience significant aero- or hydrodynamic drag, including pressure drag, wave drag, turbulence drag, etc. Drag reduction has attracted the attention of the research community, owing to its potential for reduction in both energy consumption and pollutant emissions. The work in this dissertation focuses on a family for turbulence skin-friction drag reduction by traveling waves, which have attracted people's interests both from academia and industry. Although being completely based on DNS based numerical simulations, experimental practices are considered for the DBD plasma actuator implementation in this dissertation.

Chapter 1 reviews the turbulent wall flows and the basic turbulence structures in the near-wall region. The streaks and quasi-streamwise vortices lying in the near-wall region have been found closely correlated with the turbulence skin-friction drag. Various flow control techniques have been proposed for reducing the turbulence drag, out of which, the family of traveling waves have been paid attention to in the community. The state-of-the-art of the research on traveling waves is summarized and it is noted that there are still critical information missing in order to draw definite conclusions on their performances.

Chapter 2 starts with a full parametric study on the wall velocity based spanwise traveling wave, which was believed to be closely related to the widely acknowledged work on body force based spanwise traveling wave. By sampling the parameter space with high resolution, the global performances on drag reduction and net energy saving are obtained.

In Chapter 3, the body force based spanwise traveling wave is retrospected due to the unexpected discoveries in the study of its wall velocity based counterpart. The second part in this chapter deals with a similar study on the body force based streamwise traveling wave following similar approach. The similarities between the body force and wall motion based techniques are confirmed.

Chapter 4 summarizes various flow statistics including the mean profiles, turbulence intensities, Reynolds stress, FIK identity, etc. from the flows subjected to different types of traveling wave, all with similar drag reduction values. The importance of the proper scaling is emphasized while interpreting the flow statistics.

Chapter 5 considers the experimental setup of the traveling wave by Dielectric Barrier Discharge (DBD) plasma actuators. The ideal sinusoidal shaped traveling wave could be difficult in experimental implementation due to the finite size of the control devices, which is known as the discretization effect. A DNS based modelling of the discretization effect of the DBD plasma actuator concludes that the traveling wave generated by sparse DBD plasma arrays contributes negatively to the skin-friction drag. A dense DBD plasma array, on the other hand, could be technically challenging.

In Chapter 6, a newly proposed flow control framework CPI (Constant Power Input) is introduced, which could discover the best strategy for power allocation in flow control problems. Then the drag reduction problem in a turbulent pipe flow by streamwise traveling wave is studied under the CPI framework.

The whole dissertation is concluded in Chapter 7, together with possible directions for future development based on the content of this dissertation.

I would like to take this chance to thank my advisor Prof. M. Quadrio for his guidance throughout my PhD study and the development of this dissertation. The visiting period at Prof. Kwing-So Choi's research group at Nottingham with supports from Prof. Choi himself, Dr. T. Jukes and Dr. R. Whalley is also deeply acknowledged. The resource demanding computational works in this dissertation will not be possible without the grants from super-computing facilities at CINECA and the generously offered super-computing resources at the University of Salerno.

Acknowledgements also go to my family and friends for their consistent supportive attitude on me and my PhD study.

Wenxuan Xie
Milan, Italy

Contents

Chapter 1

Introduction

This chapter introduces the fundamental of the flow structures within the wall turbulence and their links with the turbulence skin-friction. Different flow control techniques for drag reduction are briefly discussed, out of which, the traveling wave techniques are discussed in greater detail. The traveling wave flow control techniques have gained people's attention because of their large drag reducing capacities. However, there are still crucial information regarding the traveling wave techniques and their performances unknown, which is the focus of this whole dissertation.

1.1 Wall turbulence

A wall-bounded turbulent flow could be divided into three distinct regions, namely the viscous sublayer, logarithmic region and the outer region, lies in the order from the wall outwards [Pop00]. The turbulence production exceeds dissipation within the viscous sublayer, while it is exactly the other way around in the outermost outer region. Therefore, the turbulence energy is exported from the viscous sublayer all the way to the dissipation dominating outer region to maintain the turbulence there [CDAC13]. The logarithmic region is in between, where the dissipation and production are considered equal. It has been realized that the near-wall layer, being the seat of turbulence energy production, turbulence intensities, plays a crucial role in the turbulence dynamics [JP99].

The study of near-wall turbulence flow is interesting not only because rich phenomena happen in that region, but also because it is technologically important in engineering. Schoppa and Hussain [SH00] stated that the near-wall vortical coherent motions drastically increase the drag and heat transfer in the turbulence boundary layers on transport vehicles and in industrial devices. The term 'coherent motion' does not have a universally accepted definition, the definition given by Robinson [Rob91] is adopted in this dissertation, which defines the coherent motion as: *a three-dimensional region of the flow over which at least one fundamental flow variable (velocity component, density, temperature, etc.) exhibits significant correlation with itself or with another variable over a range of space and/or time that is significantly larger than the smallest local scales of the flow.* In spite of the fact that other authors may literally define the coherent motion or coherent structure differently from the one favored by Robinson [Rob91], the existence and the prominent role played by such structures in turbulence boundary dynamics had been widely acknowledged.

There exist controversial arguments over the self-sustaining mechanism of wall turbulence, nevertheless, a number of consensuses have been reached in the community after more than 50 years research [Rob91], e.g. the existence of the high and low velocity streaks lying in the wall layer of the flow and the different shaped vortices and the important roles they play in the turbulence production.

Kline et al. [KRSR67] visualized the flat plate turbulent boundary layer by hydrogen bubbles and observed the well organized streaky structures within the layer. Fig. 1.1 visualizes the streaks developed in the boundary layer at a distance to the wall $y^+ = \frac{yu_\tau}{\nu} = 4.5$, where u_τ is the friction velocity and ν is the kinematic viscosity of the fluid. The flow is from top to bottom of the picture and the photograph was taken from the top of and perpendicular to the flow field. Although being termed as the 'laminar sublayer' in Kline et al [KRSR67], the flow shows both three-dimensional and unsteady characteristics. The long streaks, which are regions of low streamwise velocity u, is formed by clustering bubbles by the spanwise velocity component w. Therefore the spanwise variation in the streamwise velocity u correlates strongly with the spanwise velocity w. The streaks waver and oscillate within the sublayer and intermittently hitting the outside layer. As the wall normal distance increases, the streaks ejected from the wall entangle with the outer region of the flow and become less distinctive. The streak bursting process is strikingly violent, which suggests that it plays a dominant role in transferring momentum between the inner and outer regions of the boundary layer.

Attempts have been thrown to physically interpret the formation of such near-wall streaky structures. There exists no generally accepted theory on the formation mechanism of the streaks and different conceptual frameworks exist for streak origin [CB05]. A plausible explanation given by Lighthill [Lig63] suggested that the stretching and compression of the spanwise component of vorticity (primarily due to the wall normal gradient of the streamwise ve-

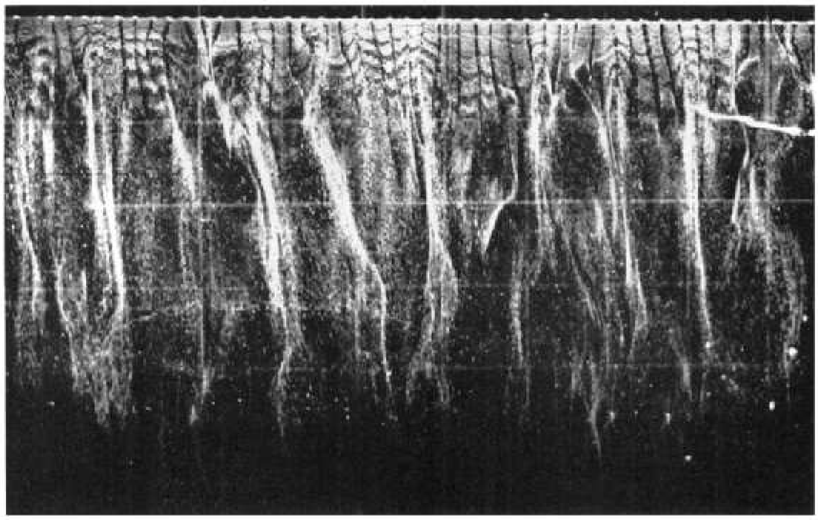

Figure 1.1: Photograph of the structure of a flat plate turbulent boundary layer at $y^+ = 4.5$. Taken from [KRSR67].

locity) would lead to spanwise variation in the streamwise velocity near the wall. The streamwise vorticity so generated would collect the low speed fluid near the wall and the streaks are formed as a result. Blackwelder and Eckelmann [BE79] experimentally discovered that as a result of strong mean velocity gradient, counter-rotating streamwise vortices exist, which 'pump' low-speed fluid away from the wall and the 'streaks' are formed as a consequence. Another view suggests that the velocity streaks are formed by the combination action of lift-up, shear and diffusion within the near-wall layer, the detailed mechanisms of which could be found in [CB05] where references that support this view are also listed.

The main topic of the dissertation, turbulence skin-friction drag, is found directly linked with the formation of streaks and streamwise vortices close to the wall [OJ94]. A modern survey on the aerodynamic drag on a commercial aircraft is shown in Fig. 1.2. More than 50% of the total aerodynamics drag comes from the viscous effect, in which the turbulence skin-friction plays as a key contributor. Therefore, a number of works have been dedicated to the study of reducing the turbulence skin-friction drag, by various types of flow control techniques. It is widely acknowledged that the suppression of wall turbulence requires attenuation of the quasi-organized wall-normal motions associated with quasi-streamwise vortices and the formation of the streaks [TL12].

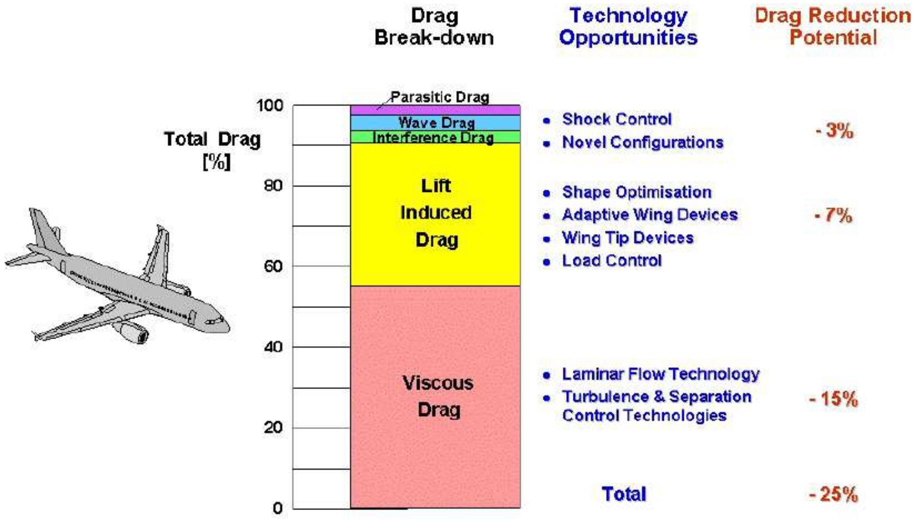

Figure 1.2: The drag break down of a modern commercial aircraft. Taken from [Sch06].

1.2 Flow control techniques

The flow control techniques are categorized into two big families: passive control and active control. The passive flow control does not require external energy input when it is operating and the active control needs external energy expenditure to actively manipulate the flow [GeH00].

Riblet is an example of skin-friction reduction by passive control with success, which is inspired by the biological surfaces [GMJ11]. The riblets grooved in the flow direction on the wall, which is believed to reduce the the skin-friction by increasing the spanwise friction of the wall [Jim94] and act as longitudinal fences that affect the evolution of quasi-streamwise vortices [KC03]. Such technique has been tested on commercial aircraft Airbus A320, on which over 70% of its surface is covered by riblets. An overall 2% drag reduction was obtained, based on fuel consumption [GMJ11].

Another example of the passive flow control in turbulence skin-friction reduction is adding polymers or surfactants into the flow. In spite of the fact that the polymers or surfactants are 'actively' injected into the fluid, the interaction between them and the flow are still passive, it is thus considered as a passive approach. The turbulence production is depressed by the long molecular chains of the polymers and string-like chains of surfactants. The molecular chains interact with the turbulence bursting cycle, and as a result, a turbulence skin-friction reduction up to 70% has been reported in [Vir75].

The biggest advantage of passive flow control is that when it is operating, no external energy is needed. Therefore, the drag reduction is always the net energy saving, the difference of which is crucial in the assessment of active control techniques. The active control approach needs the flow to be actively manipulated by the system, the process of which is certainly driven by extra external energy. The net energy saving is calculated by subtracting this extra energy expenditure from the energy saved due to drag reduction. Frohnapfel et al. [FHQ12] introduced a novel approach in flow control that unifies the consideration of energy expenditure and drag reduction. The active flow control approach could be further divided into two groups: the open-loop control and closed-loop control. Open-loop control device simply implements the control activities predetermined in the control algorithm while the closed-loop control device acts according to the system's feedback and analysis of the flow status [GeH00].

The closed-loop control requires actuators to excite the flow and sensor networks to extract the feedback information from the flow, which is a challenging task because of the high complexity. One of the first attempts in closed-loop control of wall turbulence is performed by numerical simulation by Choi et al. [CMK94]. Their so-called 'opposition control' applies a wall-normal velocity on the boundary opposite to the one measured on some wall-parallel plane [Mar09]. The 'opposition control' have recorded a drag reduction of 25% and also a net saving. However, in addition to the complexity regarding the control algorithms, the manufacture of the required actuators and sensors is also not without difficulties [KSF09].

The open-loop control techniques are relatively simple since it only requires actuators. However, the external forcing is at finite amplitude, which demands a considerable amount of energy with respect to feedback techniques [Qua11]. Thus, it is crucial to assess the energetic performance by comparing the energy saved due to the reduced drag and the energy required for flow control, which is not sufficiently addressed by many authors. Due to the relative high energy efficiency and low complexity, a number of different techniques within this category for turbulence drag reduction have been studied extensively, most of which are concentrating on active spanwise motions [Ela12], especially in the form of traveling waves.

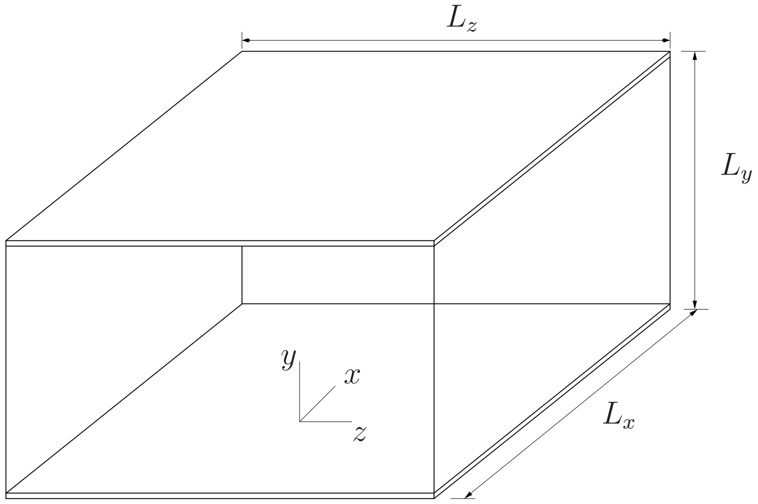

Figure 1.3: Reference system and computational domain employed in the present work for channel flow.

1.3 Important notations

It is necessary to introduce some details of the conventions which will occur consistently throughout this dissertation and also used by other authors, in order to avoid confusions on the basic concepts. The computational domain of the channel flow is sketched in Fig. 1.3, together with the reference system. The x axis is designated to point in the same direction as the flow, which is also known as the streamwise direction; the y axis is perpendicular to the upper and lower wall of the channel, therefore is always referred as the wall-normal direction; z axis crosses the flow transversely, is conventionally called as the spanwise direction or alternatively the transverse direction. The respective velocity components in x, y and z directions are u, v and w.

In this dissertation, unless otherwise stated, all quantities are scaled in outer units. Quantities in physical units are denoted by the superscript '*'. When using outer units, the length scale is the channel's half height h^* and velocity scale is the centerline velocity U_P^* of a laminar Poiseuille flow with the same flow rate. The Reynolds number in outer unit is therefore defined as $Re_P = \dfrac{U_P^* h^*}{\nu^*}$. The capital letter U^* indicates time and spatial averaging of the streamwise velocity u^* on $x - z$ plane, therefore:

$$U^*(y^*) = \overline{\langle u^*(x^*, y^*, z^*) \rangle_{x,z}} = \frac{1}{L_x^* L_z^* T^*} \int_0^{L_x^*} \int_0^{L_z^*} \int_0^{T^*} u^*(x^*, y^*, z^*) \mathrm{d}x^* \mathrm{d}z^* \mathrm{d}t^*, \tag{1.1}$$

where L_x^* and L_z^* are the lengths of the channel in x and z directions. The spatial averaging is expressed by the angled bracket $\langle\cdot\rangle$ together with the subscript indicating the direction of the averaging operations. $\langle\cdot\rangle_{x,z}$ indicates an average on the $x-z$ plane and $\langle\cdot\rangle_x$ or $\langle\cdot\rangle_z$ indicates an average in either x or z direction.

The time averaging operator $\bar{\cdot}$ is defined as:

$$\overline{f^*} = \frac{1}{T^*}\int_0^{T^*} f^*(t^*)\mathrm{d}t^*, \tag{1.2}$$

where T^* is the duration over which the time averaging operation takes place.

The quantities in inner units or wall units are denoted by the superscript '+', where the non-dimensionalisation is with the fluid viscosity ν^* and friction velocity u_τ^*. Reynolds number in inner unit is expressed as $Re_\tau = \dfrac{u_\tau^* h^*}{\nu^*}$. It is worthwhile to note that although sometime it is claimed that the quantities are scaled in 'wall units', the employed friction velocity is that of the uncontrolled or reference flow. However, the Re_τ of the reference flow and a controlled drag reducing flow could be quite different [Qua11]. Therefore, the dissertation employs two different inner scalings: either by the reference flow's friction velocity $u_{\tau,0}^*$ where the subscript '0' denotes quantities from the reference flow or by the flow's own friction velocity u_τ^*.

The friction coefficient is a measure of the skin-friction drag, defined as:

$$C_f = \frac{2\tau_w}{\rho U_b^2}, \tag{1.3}$$

where τ_w is the mean wall-shear stress, ρ is the density of the fluid and U_b is the mean flow rate in the channel. In order to quantify the effect of the forcing on the friction coefficient, the control performance indices proposed by Kasagi et al. [KHF09] are adopted. The drag reduction rate $R \equiv (P_0 - P)/P_0$ is defined as the percentage reduction of the required pumping power P with respect to the pumping power in the uncontrolled flow P_0, and corresponds to a percentage reduction in the friction coefficient. The net energy saving rate S is defined as $S \equiv (P_0 - (P + P_{in}))/P_0$, and additionally accounts for the power P_{in} required to enforce the control action. However, it is impossible for us to compute P_{in} by considering the actual efficiency of a real actuator. Hence, P_{in} only factors in the efficiency of the process by which an ideal actuator interacts with the flow.

1.4 Drag reduction by traveling waves

Many authors have attempted with different wall turbulence control techniques based on in-plane wall motion and obtained substantial turbulence skin-friction reductions [Qua11]. The first among the wall motion based techniques is the so called oscillating wall control, the control law of which is written as:

$$w = A\sin(\omega t), \tag{1.4}$$

in which, w is the spanwise velocity of the wall, A is a dimensionless velocity depicting the amplitude of the oscillation and ω is the frequency of the oscillation. The control law shown in Eq. (1.4) was first proposed and studied by Jung et al. [JMA92], in which the turbulence suppression by the oscillating wall was reported. Baron and Quadrio [BQ96] have shown the drag reduction potential of the wall oscillation, and more interestingly, the possible positive net energy saving. Quadrio and Ricco [QR04] performed a critical assessment of the drag reduction caused by the wall oscillation with parametric study and the optimal operating condition was identified. The turbulence near wall structures were found reorganized and turbulent events are pushed away from the wall by the oscillation [DCISO02].

Du et al. [DSK02] together with an earlier paper from the same group Du and Karniadakis [DK00] are the first ones discussing the traveling wave concept. In stead of letting the wall to oscillate uniformly, they prescribed a sinusoidal distributed Lorentz force (a type of body force) acting in the spanwise direction z and modulated along the spanwise direction z of the flow. Meanwhile, the wave travels in the spanwise direction z with time. The mathematical formula that describes their traveling wave is written as:

$$f_z = A_f e^{-(y+h)/\Delta}\sin(\kappa_z z - \omega t), \tag{1.5}$$

in which the f_z is the body force acting on the bulk fluid, the subscript z indicates the direction of the forcing. $A_f e^{-(y+h)/\Delta}$ is the intensity of the force, which is maximum at the wall ($y = -h$) and decays as y increases. Subscript 'f' indicates the forcing is based on body force. Δ is named the penetration length which depicts how fast the body force decays with y and is typically very small. κ_z is the wavenumber along the span of the channel and the sinusoidal wave is traveling at frequency ω. It was found that such wave could reduce the skin-friction drag by up to more than 30% when the wave parameters are properly chosen. Moreover, the near-wall turbulence cycles are significantly modified.

Quadrio et al. [QRV09] proposed streamwise traveling wave based on spanwise wall forcing for turbulence skin-friction drag reduction, which could be realized by shifting the direction of the wave in Eq. (1.5) from z to x. However, the type of forcing discussed in [QRV09] is a prescribed in-plane wall velocity distribution modulated along the streamwise direction x, which is mathematically formulized as followed:

$$w = A\sin(\kappa_x x - \omega t), \tag{1.6}$$

where w is the spanwise velocity imposed on the channel's upper and lower walls. ω and κ_x are the traveling wave's frequency and wavenumber, respectively. A is a dimensionless velocity, which is the amplitude of the traveling wave. They performed a rather complete parametric study in the wave's parameter space and obtained a maximum drag reduction of 48% and a net saving of 18%. More recently, Quadrio and Ricco [QR11] analytically expressed the Generalized Stokes Layer (GSL) generated by the streamwise traveling wave in laminar channel flow in terms of the Airy function of the first kind. Given that the turbulence convection velocity is sufficiently different from the traveling wave's phase velocity, and that the time scale of the turbulence near-wall structure's life time is larger than that of the forcing, the laminar GSL solution describes the space-averaged turbulent spanwise flow very well. Moreover, they found that the turbulence drag reduction is scaled with the thickness of the GSL.

The state-of-the-art of the turbulence drag reduction by traveling waves before the start of this PhD dissertation is summarized in Fig. 1.4. Four quadrants in the figure corresponds to four different types of traveling wave based on the forcing type and the traveling direction of the wave. The quadrant of streamwise traveling wave of wall velocity (StTW_w), has been studied extensively in [QRV09] is colored red, which indicates a full understand of its performance. The quadrants of spanwise traveling wave of body force (SpTW_bf) and spanwise traveling wave of wall velocity (SpTW_w), has been studied in [DSK02] and [ZWL04], respectively. However, their studies are based on rather limited number of sampling points in the parameter space (about 10 in [DSK02] and only 2 in [ZWL04]) and no indication of the energetic performance was discussed. Therefore, they are labeled as partially understood by the light red color. The last quadrant, streamwise traveling wave of body force, has not yet been visited before, thus is left blank here. The acronyms of the waves are composed of 'St' or 'Sp' (the direction of the traveling wave, streamwise or spanwise) + 'TW' (stands for traveling wave) + 'w' or 'bf' (wall velocity based or body force based forcing). It was hoped that by the end of this dissertation, all four quadrants would be filled with red color after exhaustive parametric studies.

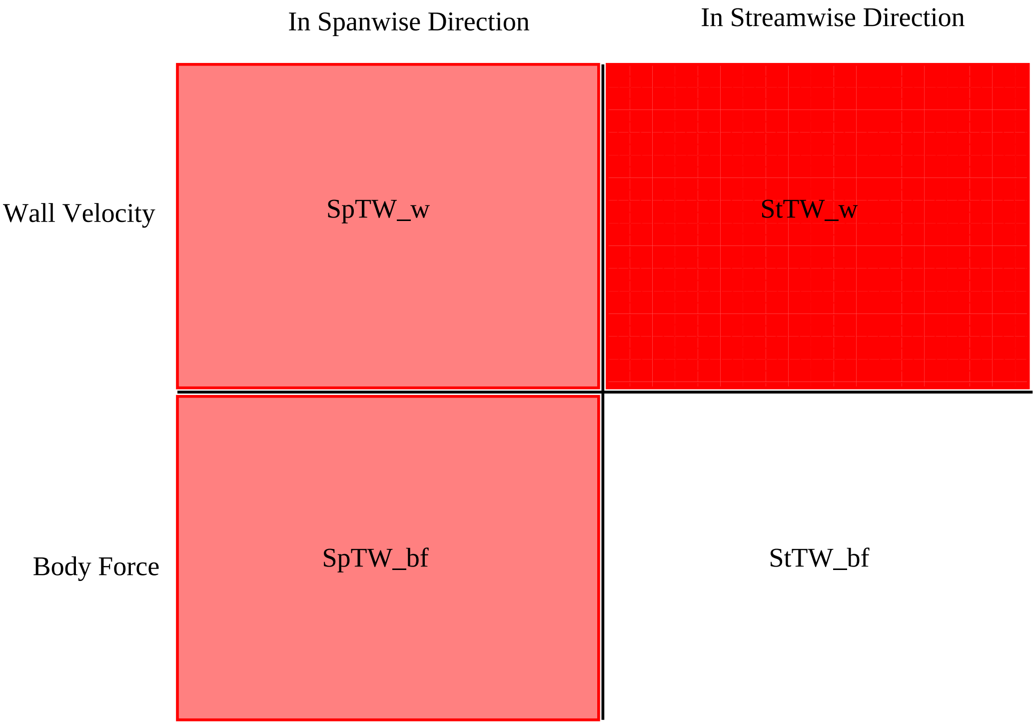

Figure 1.4: The state-of-the-art of the research on turbulence drag reduction by traveling waves. Different quadrant corresponds to a combination of the direction of the traveling wave and the forcing type as shown in the figure. Red color indicates the quadrant is completely understood, light red indicates that there have been previous studies, but the result is limited, blank indicates no body has visited the case before.

Chapter 2

SpTW_w: Spanwise-traveling waves

Du et al [DSK02] studied the drag reduction by SpTW_bf (Eq. (1.5)) in a turbulent channel flow, which is built on an idealized Lorentz force model. An alternative version of SpTW based on in-plane wall velocity or wall motion, which is known as SpTW_w, was first proposed by [ZWL04]. The traveling wave is only imposed on the wall of the channel, thus the mathematical formula is simpler comparing with the body force version of traveling wave:

$$w = A\sin(\kappa_z z - \omega t), \tag{2.1}$$

in which w is the spanwise velocity on the wall and A is the amplitude of the wall velocity.

Two major differences between Eq. (1.5) and (2.1) are: 1) the Eq. (1.5) is imposing a body force on the near wall bulk flow while Eq. (2.1) is imposing an in-plane velocity distribution directly on the wall, 2) the term $e^{-(y+h)/\Delta}$ which depicts the speed of wall normal decaying of the body force in Eq. (1.5) disappears in Eq. (2.1). However, since typically Δ has a very small value and the body force actually only affects a very thin near wall layer of bulk fluid, it is expected that these two versions of spanwise traveling wave would behave similarly. Zhao et al. [ZWL04] compared the SpTW_w with SpTW_bf and confirmed the qualitative similarities of drag reduction between these two type of waves based only on extremely limited number of cases (one for each wave). An extensive parametric study is therefore needed in order to fully understand the drag reducing and energetic performances of SpTW_w.

2.1 Method

In the simple geometric setting of the indefinite plane channel flow, the wall-based spanwise traveling wave SpTW_w described by Eq. (2.1) is studied with Direct Numerical Simulations (DNS). The goal is to fully explore the three-dimensional parameter space made by frequency ω, wavenumber κ_z and amplitude A.

The code employed in our work, described in [LQ06], is a mixed-discretization pseudo-spectral parallel solver of the incompressible Navier-Stokes equations, based on Fourier expansions in the homogeneous directions and high-order, explicit compact finite-difference schemes in the wall-normal direction. The sketch of the computational domain and the reference system was already shown in Fig. 1.3.

The value of the Reynolds number is $Re_P = 4760$, chosen to allow direct comparison with several previous studies [QRV09]. This corresponds to $Re_\tau = 200$ for the no-control case. As the simulations are carried out at constant flow rate, the pressure gradient in the streamwise direction is left free to oscillate in order to enforce the constancy of the flow rate. The pressure gradient along the spanwise direction is zero. The equations of motion are integrated forward in time, starting from the same initial condition (if not otherwise stated) made by a fully developed channel flow in statistical equilibrium, without wall forcing. The time integration, which is carried out with a partially implicit scheme with Crank-Nicholson for the viscous terms and 3rd-order low-storage Runge-Kutta for the convective terms, is carried out for 1000 outer time units, corresponding to roughly 8400 viscous time units.

The dimensions of the computational domain (further discussed below) are $L_x = 4.8$, $L_y = 2$ and $L_z = 3.2$. A Fourier expansion with 96×128 Fourier modes (further increased according to the 3/2 rule when computing the non-linear terms, in order to remove the aliasing error completely) is used in the streamwise and spanwise directions, and 100 non-equally spaced collocation points discretize the wall-normal direction. The streamwise and spanwise resolutions are $\Delta x^+ = 10$ and $\Delta z^+ = 5$, and the wall-normal resolution varies smoothly from $\Delta y^+ = 1.2$ at the wall to $\Delta y^+ = 6.6$ at the centerline.

At three values $A = 0.1$, 0.2 and 0.5 for the amplitude of the waves, the performance of SpTW_w is studied in some detail by scanning the $\omega - \kappa_z$ plane with 77 or 94 (see explanation below) different combinations of parameters. Overall, this corresponds to some 250 simulations, carried out with the main objective of investigating how the waves alter the friction coefficient C_f.

2.1.1 Domain size

The sizes L_x and L_z of the computational domain are certainly a little marginal for obtaining truly truncation-independent results. The use of rather small values as reported above is clearly motivated by the need to keep the computational cost of the entire parametric study manageable. An identical strategy was successfully employed by Gatti and Quadrio [GQ13] to investigate by DNS the oscillating-wall technique (1.4) at higher values of the Reynolds numbers. In that paper, they show how the use of such domain sizes (admittedly rather small but still significantly larger than the "minimal flow unit" described by Jiménez and Moin [JM91] to be able to sustain turbulence) does provide us with a reliable estimate of the various drag reduction trends, apart from a slight overestimate of its absolute values. To verify this in the present case, we have carried out two additional simulations with standard domain size of ($L_x \times L_y \times L_z = 4\pi \times 2 \times 2\pi$ as in [KMM87]), while keeping the spatial resolution in viscous units unchanged. One case corresponds to the uncontrolled reference flow while the other corresponds to a drag reducing case (namely $\omega = 1.0$, $\kappa_z = 1.96$ and $A = 0.5$). The comparison between the standard and moderate domain is plotted in Fig. 2.1 in terms of the friction coefficient, computed at the wall.

As expected, the quantities from the smaller-domain simulations do present larger temporal fluctuations, owing to the smaller contribution from the spatial averaging. However, the time-averaged values are quite close, both with and without drag reduction: in the uncontrolled case, the friction coefficients are $C_f = 7.92 \times 10^{-3}$ and 7.76×10^{-3} in the standard domain and the moderate domain, respectively; in the drag reducing case, the friction coefficients are $C_f = 5.84 \times 10^{-3}$ and 5.72×10^{-3}, in the standard domain and the moderate domain, respectively. Therefore, the skin-friction level in the moderate domain is underpredicted by about 2% in the uncontrolled case, and by 2% in the drag-reducing case, amounting to an almost negligible error in the estimate of drag reduction. Even though the error might not always be that marginal, a 1% to 2% difference is unlikely to affect any conclusion that will be drawn.

2.2 Results and discussions

2.2.1 Drag reduction

The analysis of the results begins by examining the values of the drag reduction rate R and net energy saving S, visualized in Fig. 2.2. Note that only cases under condition $\omega \geq 0$ and $\kappa_z \geq 0$ are considered in the study.

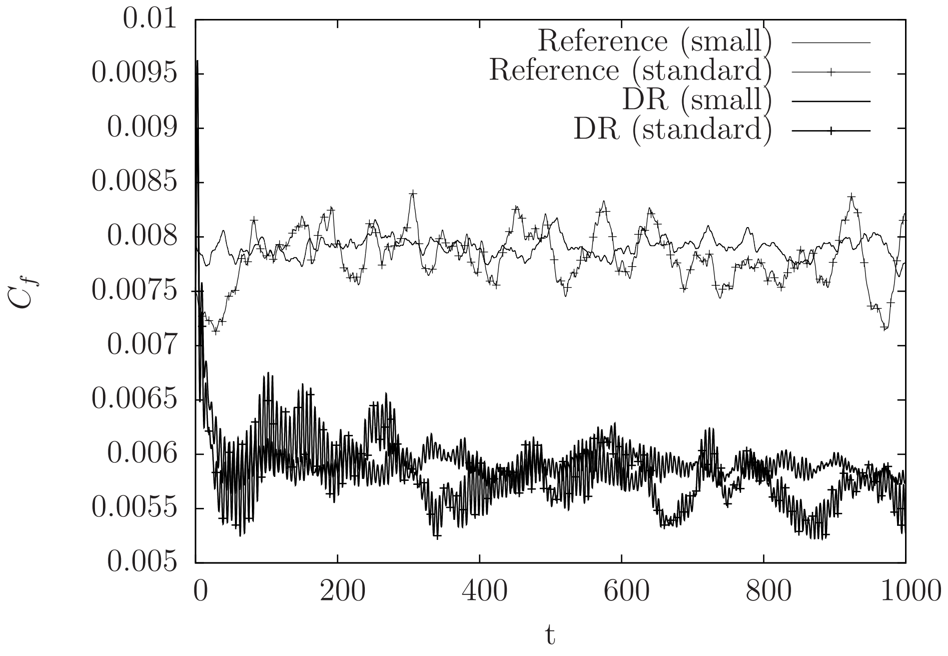

Figure 2.1: Time history of the wall-normal derivative of the space-mean streamwise velocity profile: comparison between simulations in a computational domain of standard and smaller size, for the uncontrolled case and a case with drag reduction at $\omega = 1.0$, $\kappa_z = 3.92$ and $A = 0.5$.

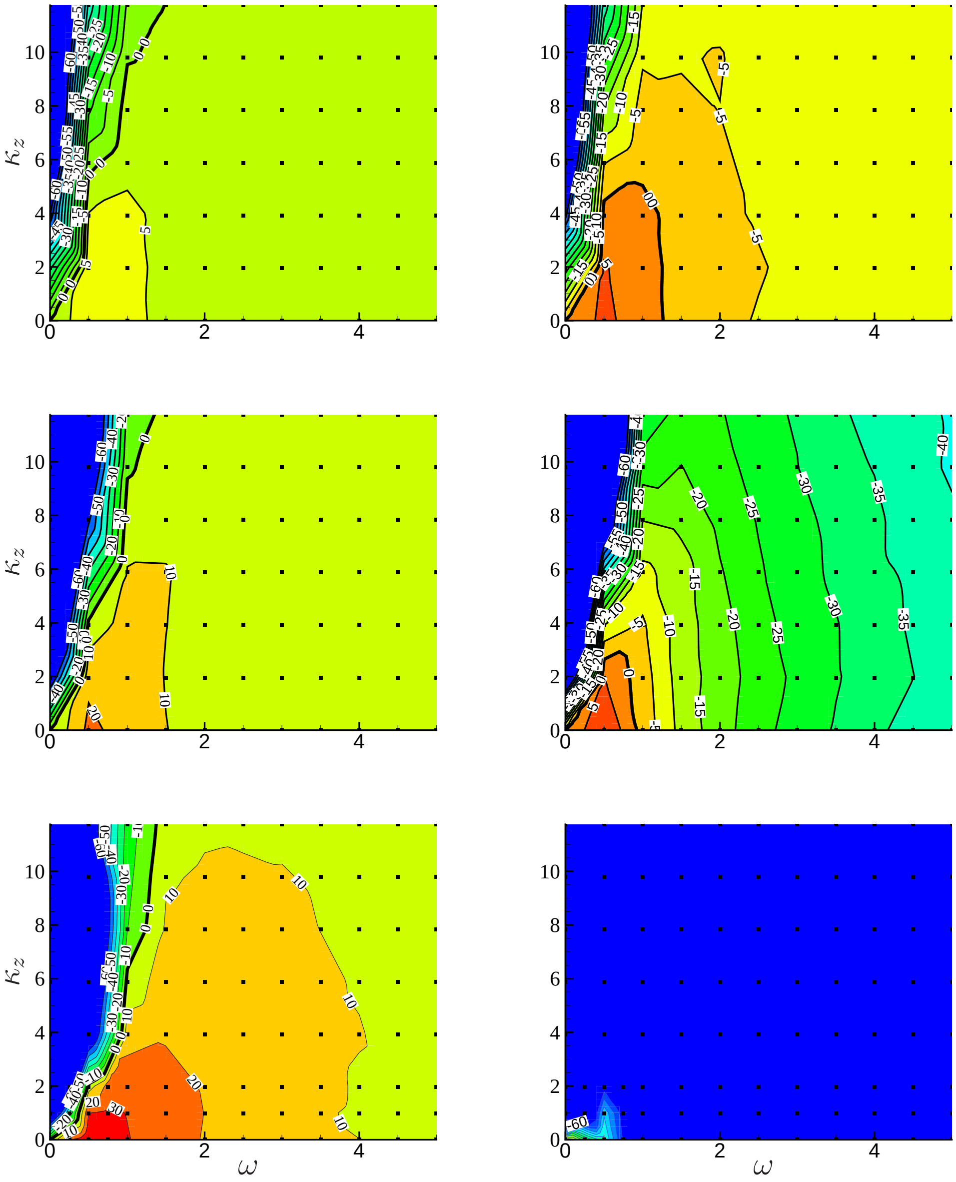

Figure 2.2: Maps of drag reduction $100R$ (left) and net energy saving $100S$ (right), for $A = 0.1$ (top), $A = 0.2$ (middle) and $A = 0.5$ (bottom). Contours spacing is 10 for the maps of R, and 5 for the maps of S; the zero contour level is highlighted by a thicker line. The small dots indicate where a DNS has been carried out. Note that the color maps cut off values smaller than -60 and therefore large negative values in the maps ($R < -60$ or $S < -60$) cannot be identified.

The positive wave frequency ω indicates that the wave travels in the positive direction of z, vice versa. The direction of the traveling wave, either in $+z$ or $-z$ directions, should not make any difference in the drag reducing or energetic performances. Similarly, the sign of the wavenumber κ_z reflects the initial phase of the traveling wave at $t = 0$, which should not affect the simulation results given the integration time is sufficiently long. The figures show contour lines on the two-dimensional $\omega - \kappa_z$ planes, corresponding to forcing amplitudes of $A = 0.1$, 0.2 and 0.5 (from top to bottom). Contours of R are shown in the left column, and the contours for S are to the right. Each dot on the maps represents a point where a DNS has been carried out. Given the relative sparsity of the DNS datapoints, to assist the visualization the contour lines are drawn based on a two-dimensional linear interpolation of the resulting drag reduction values.

We first consider the left column in Fig. 2.2, that features the drag reduction R. The three plots exhibit a common trend, with R being larger as the wave number κ_z decreases for a given value of frequency ω. At any amplitude, the largest values of R are observed at $\omega \approx 0.5$ and $\kappa_z = 0$. Hence, the largest drag reduction can be obtained when the traveling wave loses its dependence upon the spanwise coordinate, and becomes a spatially uniform temporal oscillation of the wall, as in Eq. (1.4). Indeed, $\omega = 0.5$ corresponds to an oscillation period of about 100 viscous time units, which is known [QR04] to be the optimal period for the oscillating wall, at any amplitude. By comparing the three maps, it is found that the value of R increases as the wave amplitude A increases, which is again a known result from the oscillating-wall studies. At $A = 0.5$, which corresponds to $A^+ = 12$, $R = 0.38$ which agrees well with available results on the oscillating wall. There are more DNS cases carried out (93 in total) on the plane $A = 0.5$ where the drag reduction is the largest since the region with large R should be scanned in higher resolution in order to obtain more accurate results on the maximum R value and its location. Two regions can be identified on the maps, defined by the contour level $R = 0$ (thick line) that separates the region of positive R from that with negative R. By increasing the amplitude A both regions of $R > 0$ and $R < 0$ see their peak values increase, leading to stronger gradients of R near the line $R = 0$ for larger A. The overall shape of both regions, however, is not significantly changing with A.

2.2.2 Energy budget

In spite of the fact that drag reduction assumes large values when the forcing amplitude increases, a look to the global energy budget instructs that this is not energetically convenient. From a global energetic perspective, one should consider not only drag reduction itself, but also the net benefit that is attainable after the energy required to enforce the control action is accounted for. The simulations do not model the detailed dynamics of a specific actuator, and simply enforce a suitable distribution of velocity at the boundary. Hence, by assuming actuators of unit efficiency, one can determine an upper bound for the energetic performance of the control strategy, by comparing the achieved savings to the energy requirement of the control actuated with ideal actuators.

Following [QR04], the power P_{in} required to create the spanwise traveling wave described by Eq.(2.1) is:

$$P_{in} = \frac{L_x L_z}{t_f - t_i} \int_{t_i}^{t_f} w(\tau_z^{(l)} + \tau_z^{(u)}) \mathrm{d}t, \tag{2.2}$$

where τ_z represents the spanwise component of the wall-averaged wall-shear stress and the superscripts l and u refer to the values on the lower and upper wall of the channel. P_{in} is time-averaged from the initial time t_i up to the final time t_f, with t_i properly chosen to discard the effects of the initial transient.

The right column of Fig. 2.2 presents the values of S for three wave amplitudes: $A = 0.1$, 0.2 and 0.5 from top to bottom. The level of S is significant lower for large A, which means the power required to create such waves with large A becomes larger than the power saved from drag reduction. The cases on the map with the largest R ($A = 0.5$) are characterized by the lowest net energy saving, the value of which is negative almost everywhere on the $\kappa_z - \omega$ plane, except for the origin, which represents the uncontrolled case.

The pattern of S in the plane appears to be similar to that of R. The global maximum of S is always found at $\kappa_z = 0$ and $\omega = 0.5$, the very same location where maximum R occurs (except for $A = 0.5$ as mentioned before). Therefore, the global optimal control strategy will always be the temporal spanwise wall oscillation, which consistently outperforms the spanwise traveling waves.

2.2.3 Spanwise flow rate

In most of the simulations, a non-negligible and often significant spanwise flow rate is observed as shown in Fig. 2.3. To the author's knowledge, this result has not been previously reported.

In the numerical simulation of a turbulent channel flow, two approaches (with differences and implications discussed in [FHQ12,HQF14]) are typically

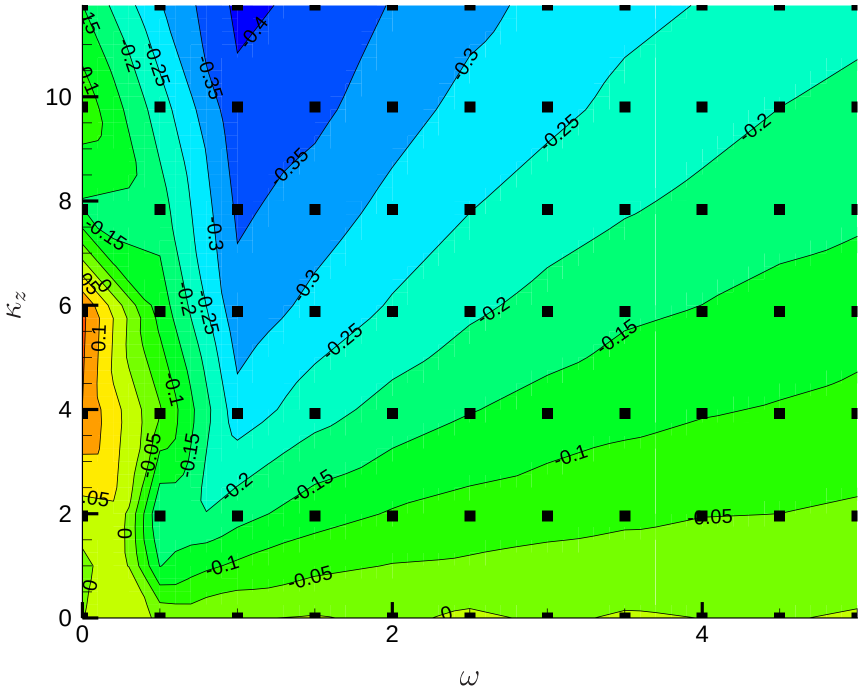

Figure 2.3: Map of spanwise flow rate on the $\omega - \kappa_z$ plane for $A = 0.5$.

used to drive the flow against viscous drag: constant pressure gradient (CPG) or constant flow rate (CFR). The present simulations use CFR as a driving strategy. A similar choice must be carried out for the spanwise direction, and CPG for the spanwise direction is used in the simulation, with of course a null value of the imposed constant pressure gradient. As the spanwise width L_z of the computational domain is always an integer multiple of the wavelength $2\pi/\kappa_z$ of the spanwise-traveling wave defined by Eq. (2.1), the integral of the forcing velocity over the wall area is null.

Thus, the explanation for the results shown in Fig. 2.3 should be sought in a different reason than forcing asymmetry. The figure clearly shows that, for a given wave intensity $A = 0.5$, the flow rate consistently possesses a negative sign in the whole $\omega - \kappa_z$ plane, if exception is made for the $\omega = 0$ axis, where both positive and negative values are present, without an apparent pattern. It is noted that a positive sign for the spanwise flow rate implies that it is in the same direction of the spanwise traveling wave, whereas a negative value indicates the opposite. The very small (both positive and negative) values on the $\kappa_z = 0$ axis are easily attributed to limited statistical sampling, as the oscillating wall induces a spanwise mean flow that obeys the Stokes laminar solution that, after the initial startup, does not present any asymmetry. Hence on this axis the values converge to zero after further time average. In the remaining plane, the flow rate exhibits a mixed behaviour; in particular, the plot shows quite a different behaviour at left / right of the line $\omega = 1$.

Flow rate at large ω

In the region with $\omega > 1$, the contour lines resemble straight lines emanating from the origin of the plane. As on such lines the phase speed $c = \omega/\kappa_z$ of the traveling waves is constant, this suggests a link between the spanwise flow rate and c. The mass flux takes place in the opposite direction of the spanwise traveling wave. The origin of the spanwise flow rate here can be traced to a viscous streaming mechanism, similar to that previously demonstrated [MKSK06, HF09] to play a role when streamwise-traveling waves of blowing and suction are applied at the wall of a turbulent channel flow. In particular, Hoepffner and Fukagata [HF09] discussed how traveling waves of blowing and suction could generate a backward mass flux in a channel in absence of an applied pressure gradient. In their paper, they illustrated the process by which a fluid particle undergoes less viscous effect while being blown away from the wall and higher viscous effect while being sucked towards the wall. The difference in the viscous effect causes the particle to move in the opposite direction of the traveling wave and eventually a net flux appears in the originally quiescent fluid in the channel.

It is surmised that a broadly similar mechanism is at work here, notwithstanding the obvious difference that at the wall here the spanwise velocity component creates a wave traveling along the spanwise direction, while in their case the wall-normal velocity component creates a wave traveling along the streamwise direction. Indeed, it is straightforward to see that the control action Eq. (2.1), while providing a spanwise modulation of the spanwise velocity component, also alters the continuity equation at the solid wall and directly induces a wall-normal motion. On the impermeable wall, as the no-slip condition $u = 0$ holds for the streamwise component, the continuity equation becomes:

$$\frac{\partial v}{\partial y} + \frac{\partial w}{\partial z} = 0. \tag{2.3}$$

By substituting Eq. (2.1) into Eq. (2.3), the wall normal velocity at the wall has to satisfy:

$$\frac{\partial v}{\partial y} = -A\kappa_z \cos\left(\kappa_z z - \omega t\right), \tag{2.4}$$

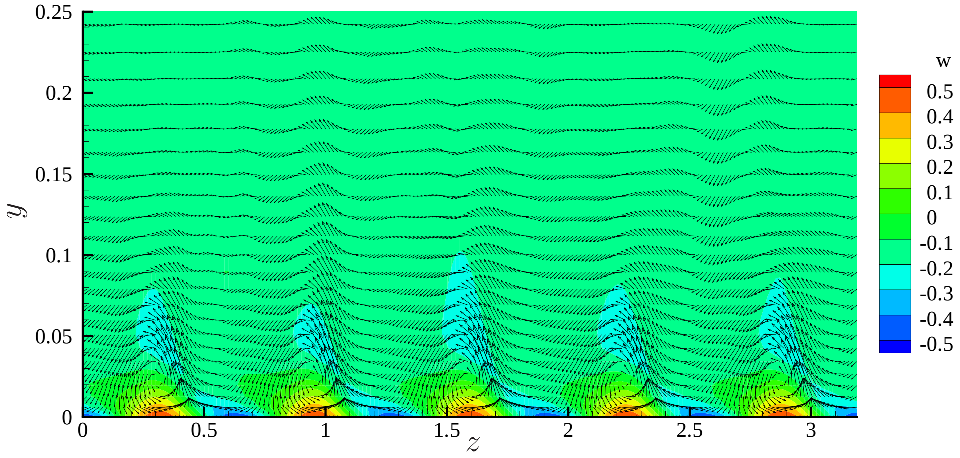

Figure 2.4: Cross-stream velocity field (averaged in streamwise direction) induced by the spanwise velocities in a turbulent channel flow subjected to SpTW_w ($\omega = 2$, $\kappa_z = 9.8$, $A = 0.5$). The arrows represent the velocity vectors on a cross-flow $y - z$ plane ($y < 0.25$). The colored contour shows the spanwise velocity, red for positive values and blue for negative values.

in order to fulfill continuity. Therefore, although the wall-normal component obeys an homogeneous no-slip condition, the spanwise forcing creates a distribution of wall normal velocity that resembles the traveling wave of blowing and suction discussed in [MKSK06, HF09]. Fig. 2.4 illustrates the instantaneous patterns of wall-normal velocity (averaged in streamwise direction) induced by the spanwise traveling wave in a near wall cross-section ($y < 0.25$) of the channel for a turbulent channel flow subjected to SpTW_w. The figure makes clear that the SpTW_w create a sort of "blowing and suction" effect, that explains the insurgence of spanwise flow rate.

To substantiate this claim more quantitatively, the amount of flow rate between that of SpTW_w and that described by Hoepffner and Fukagata in [HF09] are compared. They calculated the mean flux normalized by $|Q_0|$ as a function of the Reynolds number Re_w for 5 different wave amplitudes ϕ. Their Reynolds number Re_w is defined based on the phase velocity c of the traveling wave:

$$Re_w = \frac{ch}{\nu}; \tag{2.5}$$

for a sinusoidal wave, the quantity $|Q_0|$ is given by the equation:

$$Q_0 = -\frac{\phi L}{2\pi}, \tag{2.6}$$

where L is the wavelength of the traveling wave.

In order to compare between the spanwise flow rate generated by the in-plane spanwise wall motion and the flux generated by the blowing and suction wave, the very same notations are adopted. The case at $A = 0.5$, $\omega = 4$ and $\kappa_z = 1.96$ is considered as an example. The phase velocity based Reynolds number, the reference flux and the wave amplitude of this flow are $Re_w = 9500$, $|Q_0| = 0.01ch$ and $\phi = 0.02c$, respectively. From Fig. 2.3, it is possible to observe that the spanwise flow rate in this simulation case is about $-0.05U_P h$. Therefore, the induced normalized flow rate turns out to be near -2, which is of the same order as the values observed in Figure 4 of Ref. [HF09].

In spite that there exists a 'streaming' analogy between the traveling wave of blowing and suction and spanwise in-plane wall velocities, quantitatively the two flow rates are not directly comparable. The 'streaming' effect in the traveling wave of blowing and suction is explained in [HF09]. When the traveling wave is applied, the blowing jet will pull the fluid particle towards the centerline and at the same time drag the particle in the opposite direction of the traveling wave; on the other hand, the suction jet will push the fluid particle towards the wall and at the same time push the particle in the wave's direction. In inviscid fluid, after one cycle of the wave, the fluid particle is expected to return to its original point. However, the viscosity will break such a symmetry because when the particle is traveling in the wave's direction, it is close to the wall and will experience higher viscosity effect but when the particle is traveling in the opposite direction of the wave, it is close to the centerline and will experience less viscosity effect. Therefore, the particle will move upstream after each period. Eventually a significant net flux could be seen.

In the case of traveling wave of spanwise wall velocity, all the arguments above are still valid as a result of the 'synthetic' blowing and suction jets. However, on top of that, when the particle is pushed towards the wall, it will be affected by the spanwise moving wall (in the opposite direction of the wave). Therefore, during this process, the particle may not travel downstream but instead travels upstream! Even if the particle still travels downstream, the velocity is largely diminished by the wall velocity. Therefore at a given level of vertical jet velocities, the 'synthetic' wave is expected to produce a larger flux compare to the blowing and suction wave.

Flow rate at small ω

The part of the $\kappa_z - \omega$ plane shown in Fig. 2.3 where $\omega < 1$ shows an entirely different behaviour, that cannot be explained by the streaming effect. In this

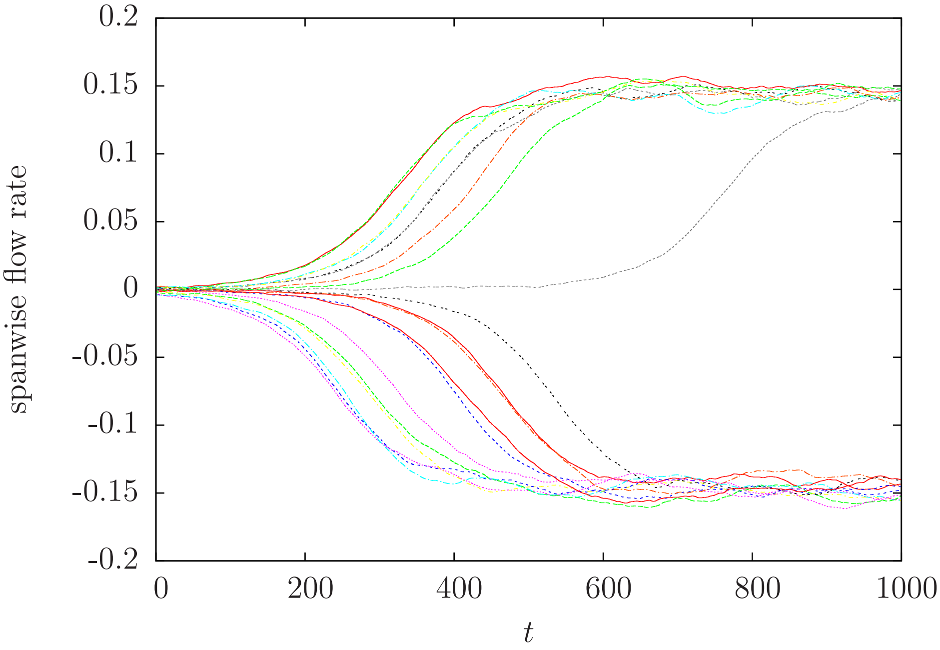

Figure 2.5: Time history of the spanwise flow rate obtained in 20 simulations each starting from a different initial fields

part of the plane the contour lines show complicated wiggling patterns of the spanwise flow rate; this is particularly evident when the points on the κ_z axis are considered. There, $\omega = 0$ and the control law reduces to:

$$w = A \sin\left(\kappa_z z\right), \tag{2.7}$$

which is a stationary wave which is symmetric with respect to the z axis. As symmetry is not broken by the preferred traveling direction of the wave, one would expect the mean flow rate to be null, while Fig. 2.3 clearly speaks for the contrary and suggests a symmetry breaking.

The only possible source for a lack of symmetry resides in the initial velocity field from which the simulations are started. The initial velocity field is identical for every computational case depicted in Fig. 2.3, and being a single realization of a turbulent flow field over a finite domain does not respect full statistical symmetry. As soon as there exist a trivial spanwise flow rate in the initial velocity field (which is almost always the case), relatively, the standing 'synthetic' wave starts to travel in the opposite direction of the spanwise bulk flow. As discussed before, the streaming mechanism 'pumps' the flow in the opposite direction of the traveling wave, therefore, the original trivial spanwise flow will be continuously pumped by the 'synthetic' wave until the streaming effect balances with the friction. This suggests that zero flow rate, which is a required consequence of statistical symmetry, will only emerge after ensemble averaging the results computed over an ensemble of different initial conditions. To verify this hypothesis, the case with $\omega = 0$, $\kappa_z = 3.92$ is picked, and launched it 20 times by starting the simulations from different initial turbulent fields. These 20 initial fields have been preliminarily computed with a standard turbulent channel flow simulation, where snapshots of the instantaneous field were recorded at time intervals (100 outer time units) much larger than the integral timescale of the process, so that they have sufficient time to decorrelate. Fig. 2.5 shows the time history of the spanwise flow rate for all the 20 cases. It can be seen that 9 out of 20 eventually end up with a positive value of 0.15, and the remaining 11 end up with the negative value of -0.15. Therefore, on ensemble averaging on a sufficiently large number of samples (initial fields), the mean spanwise flow rate is observed to be zero, and the ensemble averaging preserves the symmetry of the flow.

2.2.4 Modification of the streak pairs

In Fig. 2.6, the color contours of the streamwise velocity u on the wall-parallel $x - z$ plane at distance $y^+ = 4$ to the wall are plotted. These three plots correspond to the reference case, a drag increasing (DI) case (R=-0.89) at $A = 0.5$, $\kappa_z = 3.92$, $\omega = 0.5$ and a drag reducing (DR) case (R=0.16) at $A = 0.5$, $\kappa_z = 3.92$, $\omega = 1.0$ from top to bottom, respectively. In the reference flow, the streaky structures composed of high/low speed fluid could be easily identified from the red (high speed) and blue (low speed) colors. The streaks are about 80-100 wall units apart from each other in the spanwise direction, which is in good agreement with [DSK02].

The streaky patterns are subjected to drastic modifications when the SpTW_w is applied on the channel's walls. The most prominent change is that in both the DI and DR flows, the near-wall streamwise velocity present strong streamwise elongated structures. In the DI flow, the near wall $x - z$ plane is dominated by two high velocity (red) ridges, which are separated by two narrow low velocity (blue) stripes. In the DR flow, there exist two low speed ribbons along the streamwise direction and the high/low speed streaks are largely eliminated which are in line with what were found in [DSK02].

Intuitively, one would conject that the existence of the low speed ribbons in the DR flow's boundary layer is responsible for the lowered mean streamwise velocity profile in the near wall region. As a result, the wall normal gradient of the streamwise velocity is decreased as a consequence, and so is the drag coefficient C_f. It is therefore highly interesting to delve more into the mechanism that drives the formation of the low speed ribbons. Fig. 2.7

visualizes instantaneous spanwise velocity colored contour of the DR flow on the cross-sectional $(y - z)$ plane. The choice of the cross-section's position in x direction is trivial since the flow should be statistically x invariant. As in Fig. 2.6, the red color here indicates high spanwise velocity while the blue color indicates high negative spanwise velocity. From the snapshot in Fig. 2.7, we notice that a wall-normal jet is created by the traveling wave between the high speed (spanwise) and the low speed (spanwise) regions. As the wave travels along z direction, the bluish low speed fluid is lifted up by the wall-normal jet which could eventually cover the reddish high speed region. The low spanwise speed fluid is originally from a layer closer to the wall and therefore is of low streamwise velocity. Thus, the low streamwise speed fluid is ejected upwards and the 'ribbons' are built up. Once the phase velocity of the traveling wave turns out to be optimal, the 'ribbons' could steadily stay above the spanwise speed fluid and large R values might be expected. This hypothesis could be verified by a side-by-side comparison between the near-wall streamwise velocity and spanwise velocity contour plot of the DR case, which is shown in Fig. 2.8. The near-wall streamwsie and spanwise velocity contours at $y^+ = 4$ (scaled by canonical $u_{\tau,0}$) plane in Fig. 2.8 are taken at the same instance and it is clearly shown that the spanwise positions of the low speed 'ribbons' approximately correspond to the high spanwise velocity regions by comparing their corresponding contour lines shown in Fig. 2.8

2.3 Summary

This chapter deals with the problem on turbulence drag reduction by SpTW_w. It is found that similar to its body force based counterpart SpTW_bf, it achieves maximum drag reducing at $R = 38\%$ and records maximum net saving at $S = 10\%$. However, both optimum drag reducing and energetic performances are found when $\kappa_z = 0$, which corresponds to the wall oscillation motion. Flow visualization suggests the modification of the near-wall structures, including the 'ribbons' formed in DR case and the bulky high speed stripes appeared in the DI case.

The spanwise flow rate generated by symmetric SpTW_w is reported for the first time which is explained by the viscous streaming effect known in the traveling wave of blowing and suction case. The irregularities which could not be explained by the streaming effect are found to be linked to the asymmetry in the initial fields.

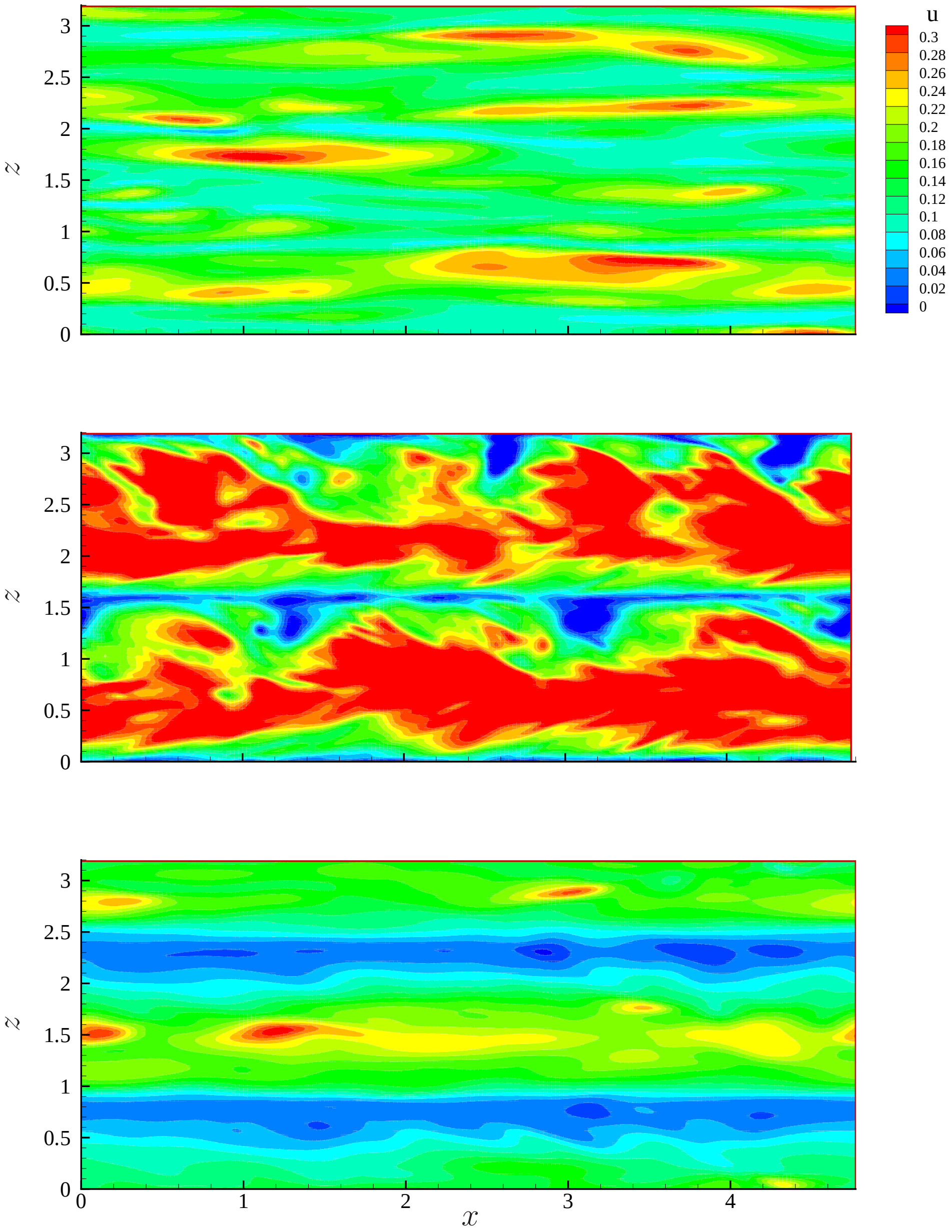

Figure 2.6: Contours for the streamwise velocity component u in a wall-parallel cut of the computational domain at $y^+ = 4$. Top: uncontrolled flow; bottom left: drag increase at $A = 0.5$, $\omega = 0.5$, $\kappa_z = 3.92$; bottom right: drag reduction at $A = 0.5$, $\omega = 1.0$, $\kappa_z = 3.92$.

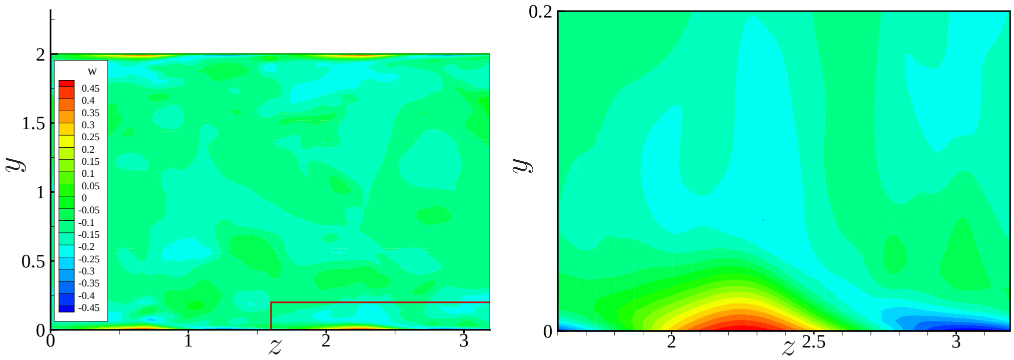

Figure 2.7: The colored contour of the DR flow's spanwise velocity on the cross-sectional $y - z$ plane of the channel. The plot on the right is a zoom in of the bottom right corner of the crosssection bounded by the red box.

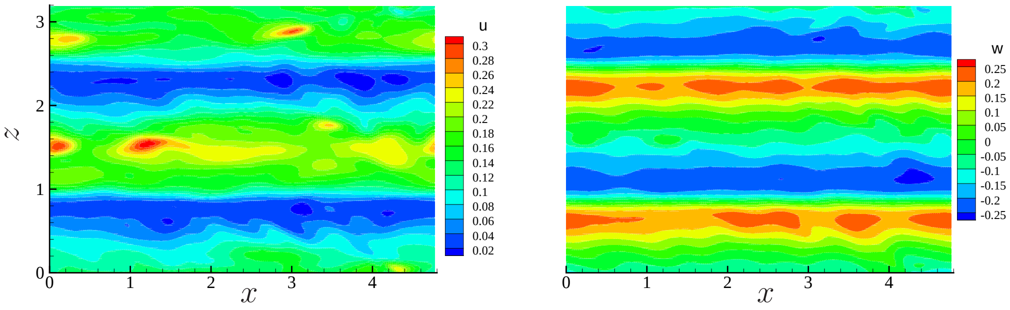

Figure 2.8: Left: the instantaneous near-wall ($y^+ = 4$) streamwise velocity contour of the DR flow. The black lines are the contour lines correspond to $u = 0.05$, which bounds the low speed ribbons. Right: the instantaneous near-wall ($y^+ = 4$) spanwise velocity contour of the DR flow. The black lines are the contour lines correspond to $w = 0.15$, which bounds the high spanwise velocity regions.

Chapter 3

SpTW_bf and StTW_bf: exploiting a volume force

The first part in this chapter revises the SpTW_bf proposed in [DSK02], the control law of which is already shown in Eq. (1.5). The second part in this chapter discusses the StTW_bf, which has not been studied before. The corresponding control law is derived by a change of the wave direction from spawise direction z to streamwise direction x as followed:

$$f_z = A_f e^{-(y+h)/\Delta} \sin(\kappa_x x - \omega t). \tag{3.1}$$

Both waves will be studied by full parametric study in their own 4-D parameter space. By the end of this chapter, it is expected that the Fig. 1.4 could be concluded with all quadrants red. The full study of the turbulence flow control family of spanwise velocity based traveling waves will not only provide a complete reference to academia research and industrial application, but also deepen the current understanding of turbulence drag reducing mechanism.

3.1 Method

As illustrated in Eq. (1.5) and (3.1), both SpTW_bf and StTW_bf are characterized by 4 wave parameters: the force amplitude A_f, the penetration depth Δ, the wavenumber κ (either in the streamwise or spanwise direction) and the wave frequency ω.

The results from the previous chapter on SpTW_w serve as a very good reference to choose reasonable 4-D parameter combinations from the whole parameter space for SpTW_bf. The wave frequency ω is sampled in the interval [0.5, 10] and the reason for ignoring the very low frequency region is that

wave parameters	values
ω	0.5, 0.75, 1, 2, 4, 6, 8, 10
κ_z	0, 1.96, 3.92, 5.88, 7.84, 9.8
A_f	0.1, 0.5, 1, 2
Δ	0.01, 0.02, 0.04, 0.1

Table 3.1: The wave parameters selected for the parametric study of SpTW_bf.

as seen from the previous chapter, the low frequency region is dominated by cases with large drag increment. The wavenumber κ_z is chosen in the interval [0, 9.8], which is comparable to that of the SpTW_w study. There is no prior knowledge on the force amplitude A_f since the relationship between the body force and wall velocity is unknown. However, it has been noticed that when the wall velocity (so is the body force needed) grows too large, the net energy saving is already impaired while the drag reduction is still increasing. Therefore, the force amplitude A_f fall into a moderate range which spans from 0.1 to 2.0, which includes the parameter range in [DSK02]. The penetration length Δ covers exactly the same range [0.01, 0.1] as in [DSK02]. The detailed parameters chosen for the parametric study of SpTW_bf are listed in Table 3.1.

Quadrio et al. [QRV09] gave a full parametric study on StTW_w. The build up of the 4-D parameter combinations in the parametric space for StTW_bf starts from their work and experience about body force gained from SpTW_bf. Fig. 2 in [QRV09] presents the map of R in the $\omega - \kappa_x$ plane for $A = 0.5$, on which, it is clearly seen that the local maxima and local minima form two elongated narrow regions. The red crest, where R is as large as 47%-48%, intersects with the κ_x axis at around $\kappa_x = 1$ and reaches the ω axis at $\omega = -0.5$. The blue ridge, where R is negative (drag increase) starts from the origin point and bounded between two zero R lines, corresponding to phase velocity $c \approx 0.35$ and $c \approx 0.6$. The same region sees rich information on the energetic performance as well. Therefore, the intervals that are probably containing interesting results are chosen for the wave frequency ω and wavenumber κ_x, i.e. $\omega \in [-2, 2]$ and $\kappa_x \in [0, 6.55]$. Note that in the case of streamwise traveling wave, the wave does not preserve symmetry about $\omega = 0$ as in the case of spanwise traveling wave. When ω is positive, the wave travels in the direction of the flow and negative ω indicates the opposite. The wave amplitude and penetration length are chosen to be in $A_f \in [0.2, 1.0]$ and $\Delta = [0.01, 0.03]$, which avoids the area where R is

wave parameters	values
ω	-2, -1.8, -1.6, ..., 0, 0.2, ..., 1.8, 2
κ_x	0, 1.31, 2.62, 3.93, 5.24, 6.55
A_f	0.2, 0.5, 1
Δ	0.01, 0.02, 0.03

Table 3.2: The wave parameters selected for the parametric study of StTW_bf.

high but S is extremely low. Table 3.2 provides the full list of the selected parameters.

The geometry of the simulation domain is identical to the one used in the study of Sptw_w and the resolution level, time integration length are kept unchanged as well. In total nearly 800 and 1200 DNS cases sample the whole 4-D parameter space for SpTW_bf case and StTW_bf, respectively.

The drag reduction $R \equiv \dfrac{P_0 - P}{P}$ and net energy saving $S \equiv \dfrac{P_0 - (P + P_{in})}{P_0}$ are still the key factors to look at for the evaluation of the control method. Extra attention has to be paid while calculating the net energy saving S. The net energy saving S accounts for the energy spent to enforce the flow control P_{in} in the total energy saving P_{tot}. The dimensionless expressions of P_{in} and P_{tot} are both physically meaningful, however, they are not scaled in the very same manner and therefore, one will have to convert them back to the dimensional form to make the direct comparison feasible.

We first look at the power saved due to flow control P_{tot}:

$$P_{tot} = \frac{U_b L_x L_z}{t_f - t_i} \int_{t_i}^{t_f} \left[(\tau_{x,0}^{(l)} - \tau_x^{(l)}) + (\tau_{x,0}^{(u)} - \tau_x^{(u)}) \right] \mathrm{d}t. \tag{3.2}$$

For simplicity, we can neglect the time integration and averaging since it does not affect the derivation in any sense since the dimensionality is still the same, which is the focus here. Furthermore, the upper and lower wall shear stress could be regarded as two equal quantities $\tau_{x,0}$ and τ_x. Therefore, the Eq. (3.2) could be re-written as:

$$P_{tot} = 2U_b L_x L_z (\tau_{x,0} - \tau_x). \tag{3.3}$$

In the DNS code, the wall-normal derivative of the mean velocity at the wall $\partial U/\partial y$ are calculated to describe the shear stress quantitatively. The exact relation between the shear stress on the wall and the streamwise velocity gradient in the wall-normal direction is expressed by:

$$\tau_x = \mu \frac{\partial U}{\partial y}. \tag{3.4}$$

Then, substitute Eq. (3.4) into Eq. (3.3) and obtain:

$$P_{tot} = 2U_b L_x L_z \mu \left[\left(\frac{\partial U}{\partial y} \right)_0 - \left(\frac{\partial U}{\partial y} \right) \right]. \tag{3.5}$$

In the code, the body-force f_z is the force acting on the fluid per unit mass. Thus, P_{in} is written as:

$$\begin{aligned} P_{in} &= \frac{1}{t_f - t_i} \int_{t_i}^{t_f} \int_0^{L_x} \int_0^{L_z} \int_0^{2h} \rho f_z w \ \mathrm{d}y\mathrm{d}z\mathrm{d}x\mathrm{d}t \\ &= \frac{\rho}{t_f - t_i} \int_{t_i}^{t_f} \int_0^{L_x} \int_0^{L_z} \int_0^{2h} f_z w \ \mathrm{d}y\mathrm{d}z\mathrm{d}x\mathrm{d}t \\ &= \frac{\rho L_x L_z}{t_f - t_i} \int_{t_i}^{t_f} \int_0^{2h} \langle f_z w \rangle_{x,z} \ \mathrm{d}y\mathrm{d}t. \end{aligned} \tag{3.6}$$

The spatial averaging operator $\langle \cdot \rangle$ has been defined in Chapter 1. Similar to the power saving, the time integration and averaging could be neglected for simplicity due to the same reason, one may obtain:

$$P_{in} = \rho L_x L_z \int_0^{2h} \langle f_z w \rangle_{x,z} \ \mathrm{d}y. \tag{3.7}$$

The underlined quantities in outer units are scaled following:

$$U = \frac{U^*}{U_P^*}, \ w = \frac{w^*}{U_P^*}, \ y = \frac{y^*}{h^*}, \ \text{and } f_z = \frac{f_z^*}{U_P^{*2}/h^*} \tag{3.8}$$

By substituting Equations (3.8) into Eq. (3.5) and (3.7), one obtains:

$$P_{tot}^* = \frac{2U_b^* U_P^* L_x^* L_z^* \mu^*}{h^*} \left[\left(\left\langle \frac{\partial U}{\partial y} \right\rangle_{x,z} \right)_0 - \left\langle \frac{\partial U}{\partial y} \right\rangle \right], \tag{3.9}$$

and

$$P_{in}^* = \rho^* U_P^{*3} L_x^* L_z^* \int_0^2 \langle f_z w \rangle_{x,z} \ \mathrm{d}y. \tag{3.10}$$

$$\begin{aligned}\frac{P^*_{tot}}{P^*_{in}} &= \frac{2U^*_bU^*_P}{{U^*_P}^2}\frac{\mu^*}{\rho U^*_P h^*}\frac{\left[\left(\left\langle\frac{\partial U}{\partial y}\right\rangle_{x,z}\right)_0 - \left\langle\frac{\partial U}{\partial y}\right\rangle_{x,z}\right]}{\displaystyle\int_0^2 \langle f_z w\rangle_{x,z}\,\mathrm{d}y} \\ &= \frac{2U_b}{Re_P}\frac{\left[\left(\left\langle\frac{\partial U}{\partial y}\right\rangle_{x,z}\right)_0 - \left\langle\frac{\partial U}{\partial y}\right\rangle_{x,z}\right]}{\displaystyle\int_0^2 \langle f_z w\rangle_{x,z}\,\mathrm{d}y}\end{aligned} \tag{3.11}$$

The numerator and denominator of the term $\frac{\left[\left(\left\langle\frac{\partial U}{\partial y}\right\rangle_{x,z}\right)_0 - \left\langle\frac{\partial U}{\partial y}\right\rangle_{x,z}\right]}{\displaystyle\int_0^2 \langle f_z w\rangle_{x,z}\,\mathrm{d}y}$ are two of the simulation's outputs. Eq. (3.11) successfully linked the two physical quantities P^*_{tot} and P^*_{in} with the dimensionless results from the simulation.

3.2 Results and discussions

3.2.1 SpTW_bf

Drag reduction

The results on drag reduction $100R$ are collected and summarized in Fig. (3.1) in four 3-D ($\omega - \kappa_z - A_f$) plots correspond to four different penetration lengths $\Delta = 0.01,\ 0.02,\ 0.04$ and 0.1. Each red dots represents one simulation carried out and the colored contour is drawn based on 3-D linear interpolation of the R values. In spite that only the surfaces of the 3-D plots are visible, it is still possible to observe that the pattern of drag reduction value R, which appears similar to what has been seen in Fig. 2.2.

Both the drag increasing DI region and the drag reduction DR region are confined within the region $\omega < 6$. When the frequency is higher, the wave barely affects the turbulence skin-friction drag of the flow. The mechanism of turbulence drag reduction by the spanwise traveling wave is still not fully understood, however many authors, e.g. Dhanak and Si [DS99], Choi [Cho00], etc. have agreed on the fact that the weakened streamwise

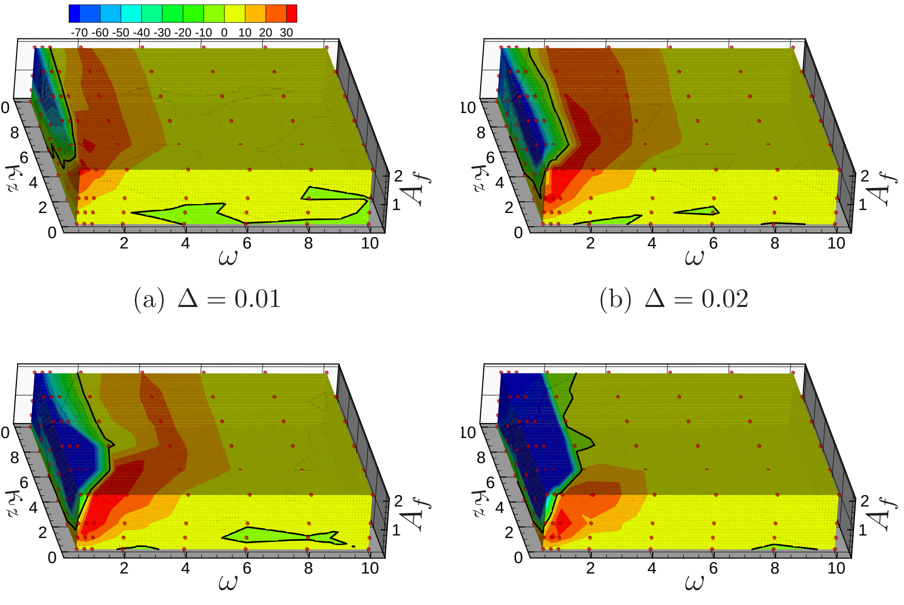

(a) $\Delta = 0.01$ (b) $\Delta = 0.02$

(c) $\Delta = 0.04$ (d) $\Delta = 0.1$

Figure 3.1: The 3-D maps of drag reduction value $100R$ at penetration lengths $\Delta = 0.01$, 0.02, 0.04 and 0.1, respectively. The small dots indicate where a DNS has been carried out. The color maps cut off values below -70.

vorticity, as a result from the interaction between the turbulence boundary layer and the flow control, is a key contributor to the reduced drag. In all of the 4 maps in Fig. 3.1, the DI regions locate at areas with very low wave frequency ω, which means the wave is 'quasi-standing' rather than traveling. Flow visualization shows that such waves will cause the streamwise vortices to intensify and cluster instead of being eliminated and spread out in the spanwise direction. As the value of ω grows, the value of drag reduction R rapidly increases and at certain point, R reaches its local maximum. As the wave frequency becomes higher, the drag reduction R quickly falls close to null value, which implies that the turbulence production process is barely altered by the weak interaction between the traveling wave and the turbulent flow.

Comparing the 4 maps in Fig. 3.1, it is found that, as the penetration length Δ increases, the 3-D global maximum R moves towards higher frequency ω and lower wave amplitude A_f. This relationship qualitatively agree with the condition of large R derived by Du et al [DSK02]:

$$I \times T^{+} \times \Delta \approx 1. \tag{3.12}$$

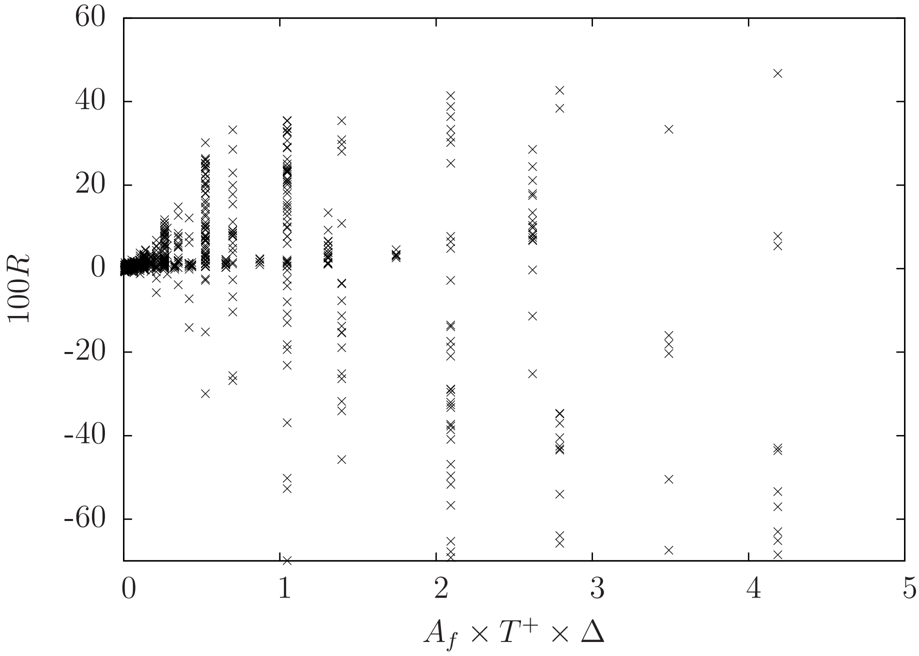

Figure 3.2: The product $A_f \times T^+ \times \Delta$ versus the drag reduction value R corresponding to the spanwise traveling waves.

Note that the notation I used in [DSK02] describes the body force intensity which corresponds exactly to A_f in the current study. However, the Eq. 3.12 is not exactly held by the simulation data. Fig. 3.2 plots the product $A_f \times T^+ \times \Delta$ versus the drag reduction value R of a part of the DNS cases. Under the condition as given by Eq. (3.12), the possible R value spans from approximately -0.7 up to 0.4, which means that condition Eq. (3.12) certainly does not guarantee large drag reduction. Moreover, it is easy to see from Fig. 3.2 that the large R ($R = 0.3$) cases may occur at a quite large range of values of $A_f \times T^+ \times \Delta$. It should also be pointed out that the using Eq. (3.12) is dubious because it mixes up the quantities in outer unit and inner unit.

One of our motivations in taking a retrospect of SpTW_bf is that in SpTW_w, the largest drag reduction R is always found in a special case of the traveling wave where the wavenumber $\kappa_z = 0$ (Fig. 2.2). The 4 3-D plots in Fig. 3.1 only enable the visualization of the surfaces of the 3-D domain. In order to capture the exact maximum R location, we plot 3 iso-surfaces of R ($100R = 20,\ 30,\ 40$) for the 4 maps of R, respectively in Fig. 3.3. The contour is constructed by linear interpolation, therefore at some parts the suface is quite wiggly. Nevertheless, it is clearly illustrated that by increasing the R value, the iso-surfaces quickly shrink and moving towards the plane where $\kappa_z = 0$ and eventually, all the 3-D global maximum R are obtained on that plane. Similar to SpTW_w, the body force based case also favors larger wavelengths, and the global maximum drag reduction R occurs at infinite wavelength $\lambda = \infty$, or $\kappa_z = 0$, which is also a special case of the traveling wave: the spanwise oscillatory excitation.

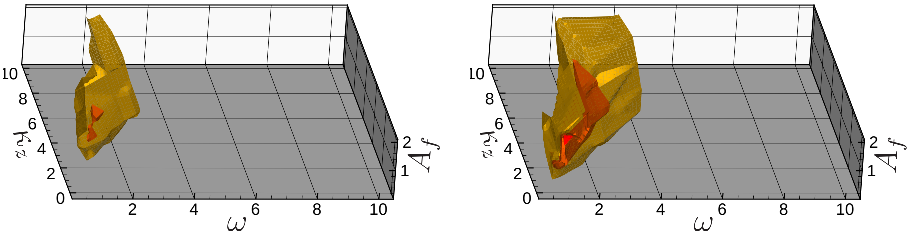

(a) $\Delta = 0.01$ (b) $\Delta = 0.02$

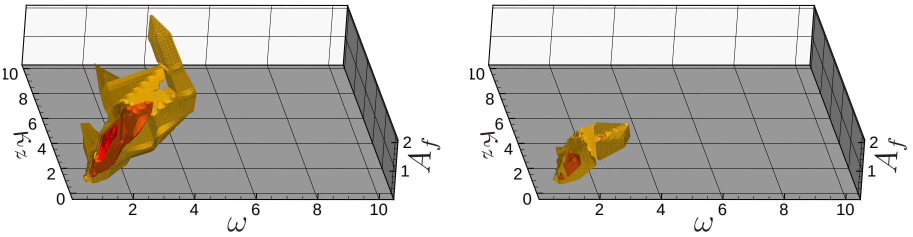

(c) $\Delta = 0.04$ (d) $\Delta = 0.1$

Figure 3.3: The isosurfaces of $100R$ at $20(yellow)$, $30(orange)$, $40(red)$ at 4 different penetration length Δ.

Fig. 3.3 also characterizes the role of the penetration length Δ. One of the key difference between the wall based and body force based control is that body force have one more parameter Δ to adjust. This extra degree of freedom offers the possibility of explicitly tuning the depth of the disturbance. The waves of intermediate penetration length are capable of larger drag reduction. Among the four different penetration lengths, $\Delta = 0.02$ and 0.04 enable better drag reduction performances compare to the very small or large penetration length. The overall global maximum drag reduction is achieved at $\Delta = 0.4$ together with the parameter combination $\omega = 1$, $\kappa_z = 0$, and $A = 2$. Table 3.3 listed the comparison between the global maximum drag reduction from SpTW_w and SpTW_bf. The amplitudes of the two waves are not directly comparable since they are intrinsically different physical quantities: one is dimensionless velocity and the other is dimensionless body force per unit mass. The spanwise velocity profile plotted

	R_{max}	wave parameters
wall velocity	38%	$\kappa_z = 0$, $\omega = 0.5$, $A = 0.5$
body force	47%	$\kappa_z = 0$, $\omega = 1$, $A_f = 2$, $\Delta = 0.04$

Table 3.3: The comparison between the global maximum drag reduction between two types of traveling wave: the wall motion and the body force based versions.

in Fig. 3.4 allows us to visually interpret the plain wave amplitudes. Fig. 3.4(a) and 3.4(b) show different spanwise velocity profiles from the optimum spanwise wall oscillation and optimum spanwise oscillatory body force along the wall normal direction at different phases during one period, respectively. Fig. 3.4 makes the comparison between the two different types of oscillatory motion possible since they are both translated into spanwise velocities. The maximum spanwise velocities in both Fig. 3.4(a) and 3.4(b) are about half of the reference velocity. However, the difference between the drag reduction R is almost 10% (Table 3.3), which is benefited from the fine tuning of the extra wave parameter Δ.

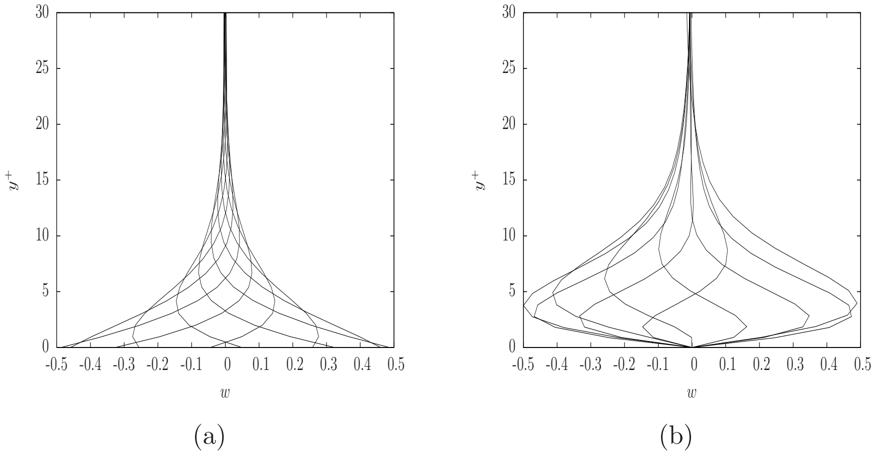

(a) (b)

Figure 3.4: Spanwise velocity profile with the global maximum drag reduction R performance: (a) spanwise wall oscillation ($\omega = 0.5,\ \kappa_z = 0,\ A = 0.5$), (b) collective spanwise body forcing excitation ($\omega = 1,\ \kappa_z = 0,\ A_f = 2,\ \Delta = 0.04$).

	S_{max}	wave parameters
wall velocity	10%	$\kappa_z = 0$, $\omega = 0.5$, $A = 0.2$
body forcing	12%	$\kappa_z = 0$, $\omega = 0.75$, $A_f = 0.5$, $\Delta = 0.04$

Table 3.4: The comparison between the global maximum drag reduction between two types of traveling wave: the wall motion and the body forcing based versions.

Energy budget

Similar to the drag reduction, the net energy saving S is shown in Fig. 3.5 by 4 sub-figures at 4 different penetration lengths. Fig. 3.5 suggests that for all four penetration lengths, the positive net energy saving generally only occurs when the wave amplitude A_f is small. As the amplitude A_f increases, the net energy saving tend to decrease, which is quite different from what we have seen on drag reduction. This follows the very same reasoning as the discussion in the previous chapter: as the wave amplitude increases, the energy required by the flow control system grows faster than the energy saved by the flow control.

The iso-surfaces for the net energy saving ($S = 0.05$) are shown in Fig. 3.6 to explore the global maximum net saving. All four cases have their relatively large S region near the corner of low frequency, low wavenumber and low wave amplitude in the parameter space, where the P_{in} is small while the drag reduction R is significant. By examining the results, it is found that when considering the net energy saving, the maximum value in the 3-D parameter space also occur only when the wavenumber $\kappa_z = 0$. In terms of net energy saving, the spanwise oscillatory body force is of a better performance than the more general spanwise traveling wave of body force.

The global maximum net energy saving in the 4-D parameter space is found with the wave parameters: $\omega = 0.75$, $\kappa_z = 0$, $A_f = 0.5$ and $\Delta = 0.04$ as summarized in Table 3.4. Although Table 3.3 revealed that the spanwise oscillatory body force is of a larger drag reduction potential, its net energy saving capability is very similar to the spanwise wall oscillation. The extra flexibility from tuning the penetration length enables a better adjustment of the body force, however, a price of extra control energy is paid for such a freedom.

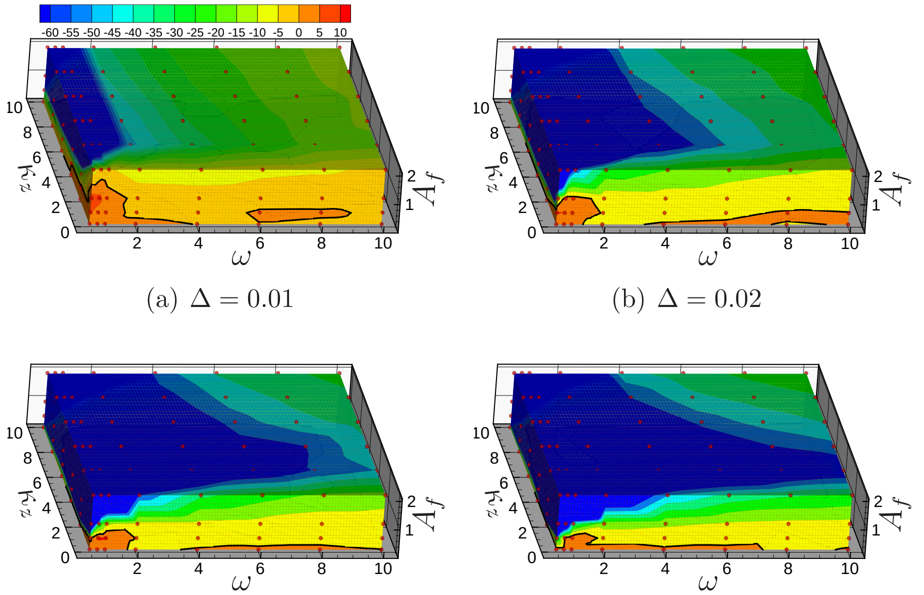

(a) $\Delta = 0.01$ (b) $\Delta = 0.02$

(c) $\Delta = 0.04$ (d) $\Delta = 0.1$

Figure 3.5: The maps for net energy saving $100S$ in the 3-D space $\omega - \kappa_z - A_f$ at different penetration lengths Δ. The small dots indicate where a DNS has been carried out. The color maps cut off values smaller than -60.

Near wall flow structures

The streamwise velocity contour is plotted in Fig. 3.7 on the $x - z$ plane parallel to the wall with a wall normal distance $y^+ = 4$ for one drag increase (DI) and one drag reduction (DR) case together with the reference flow case. The only difference between the DI and DR cases is the wave frequency: the DI case has a frequency of $\omega = 0.5$ while $\omega = 2$ in the DR case. Similar to Du et al. [DSK02], in the case of drag reduction, the high-low speed streak pairs are largely eliminated and a low speed ribbon is formed. This is also found in Fig. 2.6, except two 'low speed ribbons' are presented there. The number of "ribbon" is determined by the number of wave lengths that are fitted in the spanwise direction, the mechanism of which is explained by Fig. 2.7 . By using the same color scale in Fig. 3.7, the near-wall structure is not identifiable in the DI case since the streamwise velocity is largely amplified.

Kravchenko et al. [KCM93] has shown that the streamwise vorticity is highly correlated with the turbulence shear drag. In Fig. 3.8, vortices are plotted according to the λ_2 criterion proposed by [JH95] for the DI and DR case, in comparison with the reference flow without control. From Fig. 3.8 one can observe that the vortex intensity of the DI case is much larger than

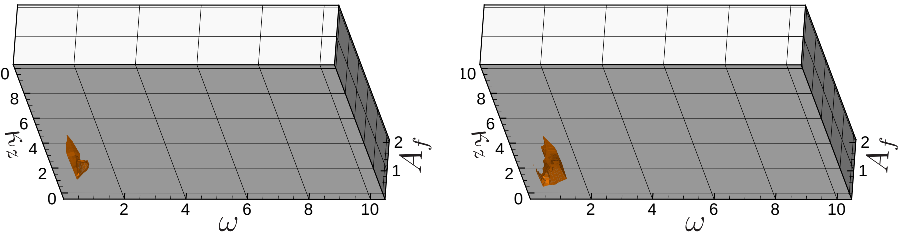

(a) $\Delta = 0.01$ (b) $\Delta = 0.02$

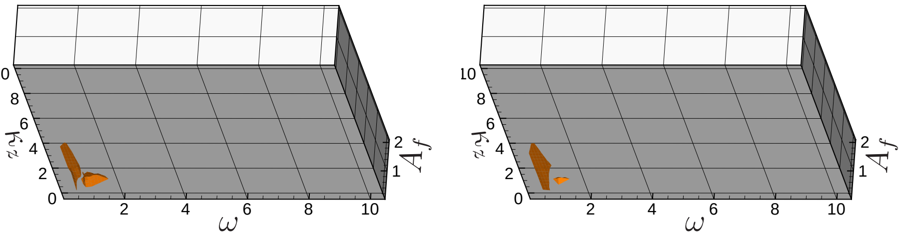

(c) $\Delta = 0.04$ (d) $\Delta = 0.1$

Figure 3.6: The isosurfaces for net energy saving S ($S = 5\%$) in the 3-D space $\omega - \kappa_z - A_f$ at different penetration lengths Δ.

the uncontrolled flow as expected. The vortices in the DI case also shows very strong clustering pattern which is not present in the uncontrolled flow. On the other hand, the vortices in the DR flow are much weakened. Both the DR and DI cases are subjected to the spanwise traveling wave with the same body force intensity A_f, wavenumber κ_z and penetration length Δ. Therefore the difference between the vorticity intensity and clustering is only due to the value of frequency ω, or the phase velocity $c = \dfrac{\omega}{\kappa_z}$. From Fig. 3.1, the DR cases generally have larger phase velocity than the DI cases, and this implies that while the body force acting on the flow tends to cluster the vortices, in the meantime the vortices are convected in the spanwise direction with the traveling wave.

Spanwise flow rate

As noticed in the previous chapter, the spanwise traveling wave of body force also induces net flux in the spanwise direction. This phenomenon could be explained by the "streaming" effect reported by Hoepffner and Fukagata [HF09] since the spanwise forcing creates 'synthetic' traveling wave of blowing and suction. The details of the mechanism could be found in their paper and

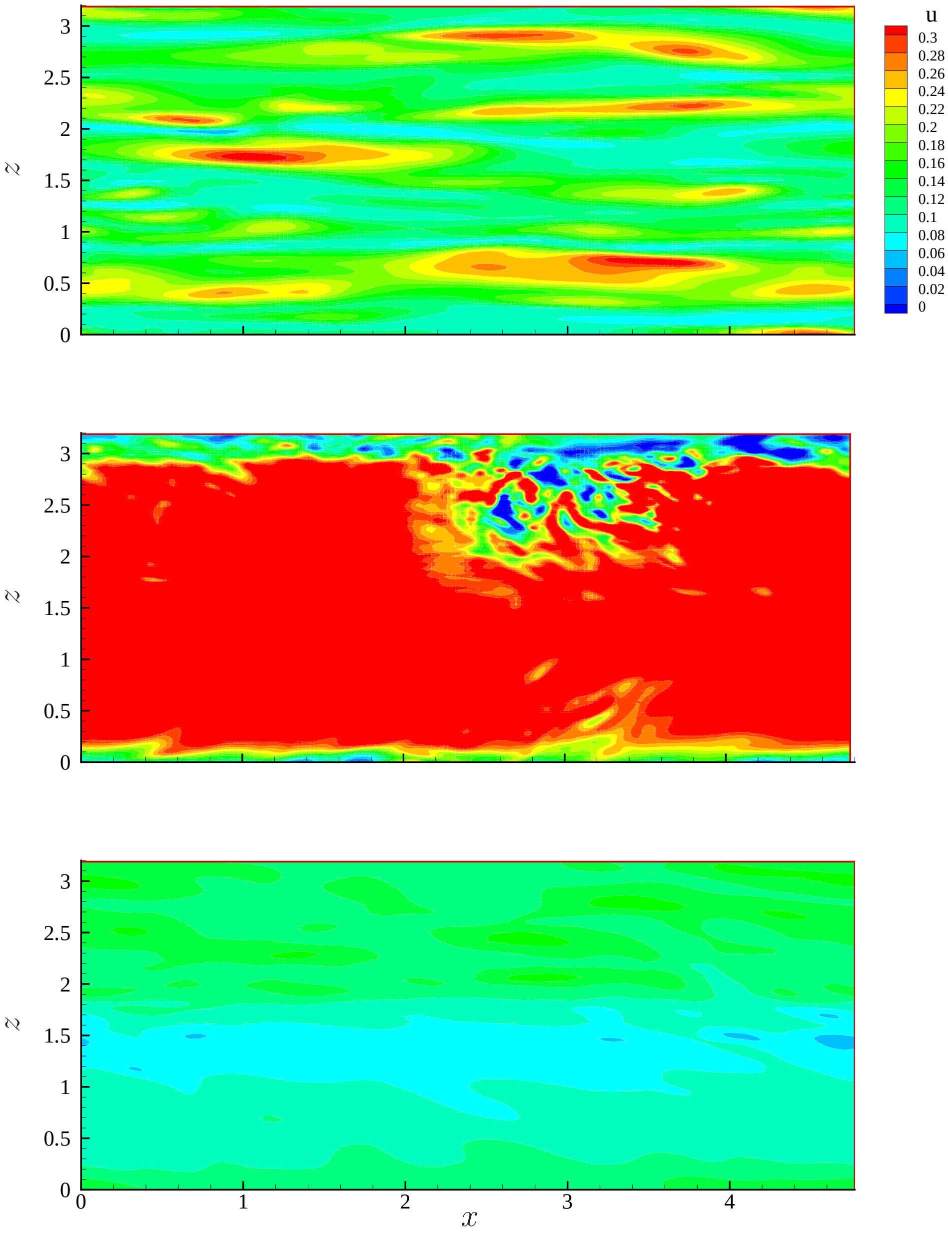

Figure 3.7: The streamwise velocity contour at $y^+ = 4$. From top to bottom: the uncontrolled flow; the DI case with $\omega = 0.5$, $\kappa_z = 1.96$, $A_f = 2$ and $\Delta = 0.02$; the DR case with $\omega = 2$, $\kappa_z = 1.96$, $A_f = 2$ and $\Delta = 0.02$.

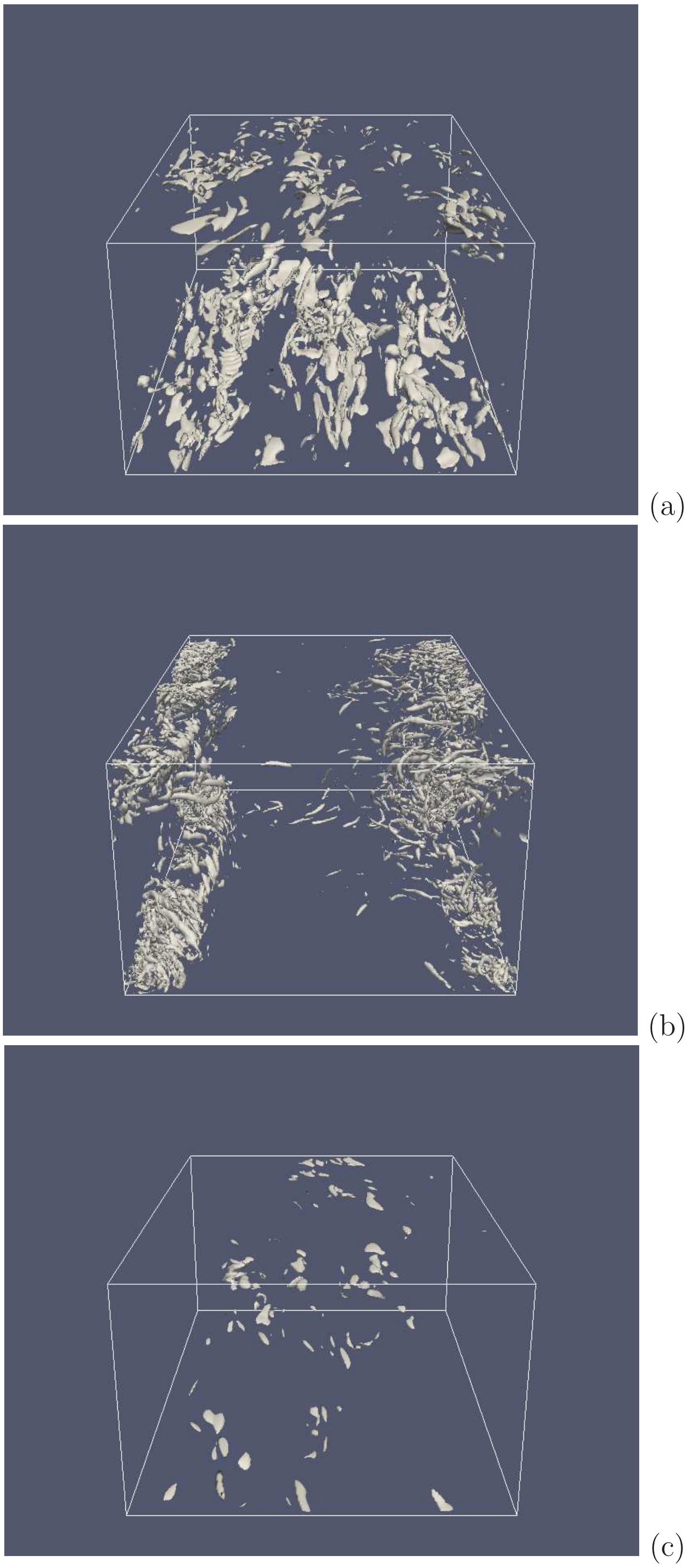

Figure 3.8: The λ_2 contour of the uncontrolled case (a), the DI case (b) and the DR case (c) . The contour is set at $\lambda_2 = -20$.

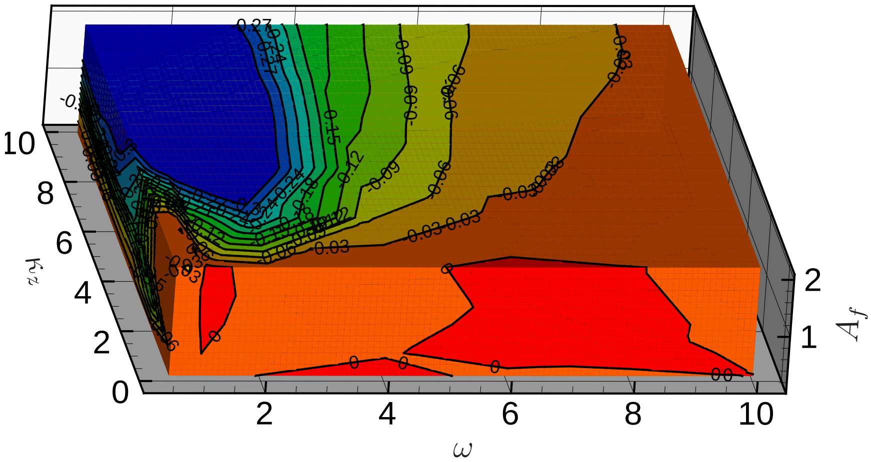

Figure 3.9: The map of the spanwise flow rate created by SpTW_bf in 3-D space $\omega - \kappa_x - A_f$ at penetration length $\Delta = 0.03$.

also in the previous chapter. In Fig. 3.9, the spanwise flow rate produced by the SpTW_bf wave at penetration length $\Delta = 0.03$ is plotted. The remarkable spanwise flow rate is easily explained by the arguments that have been made in the SpTW_w case in the previous chapter.

However, the flow rate in Fig. 3.9 does not show strong linear dependency on the phase speed as in the case of wall motion (Fig. 2.3). For a certain value of phase speed c_0, as the wave frequency ω increases, the interaction between the body forcing and the fluid becomes weaker since the wave is traveling too fast for the fluid to adapt. The less efficient interaction eventually leads to a lower spanwise flow rate due to the fact that the fluid could not take full advantage of the forcing.

3.2.2 StTW_bf

Drag reduction

The left column in Fig. 3.10 plots the drag reduction value R correspond to Δ = 0.01, 0.02 and 0.03 from top to bottom. It is possible to see the basic patterns appeared in the plots by only visualizing the surfaces of the 3-D parameter space. The three maps are qualitatively similar, where they all exist a ridge of large drag reduction (the red region) and a wedge shaped drag promoting region (blue color). Similar patterns are also reported in Quadrio et al. [QRV09].

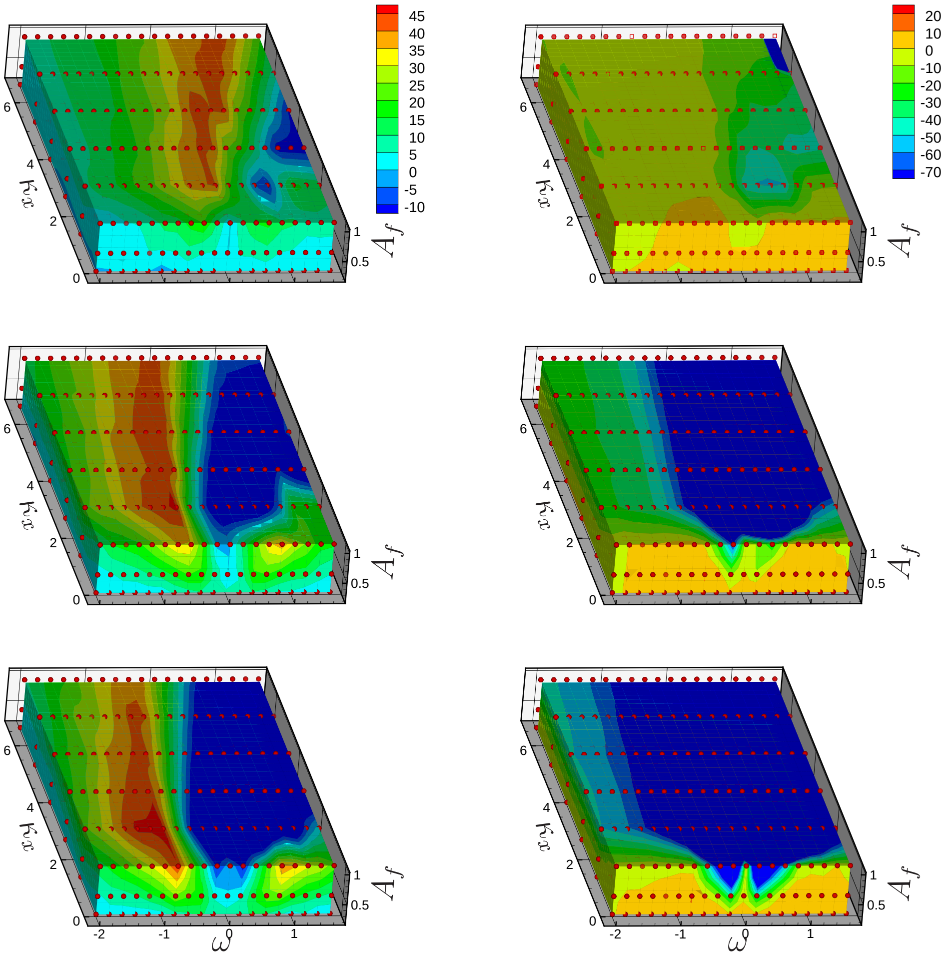

Figure 3.10: The 3-D maps of drag reduction value $100R$ (left column) and $100S$ (right column) at penetration lengths $\Delta = 0.01,\ 0.02,\ and\ 0.03$ from top to bottom, respectively. The small dots indicate where a DNS has been carried out. The color maps cut off values below -10 for $100R$ and -70 for $100S$.

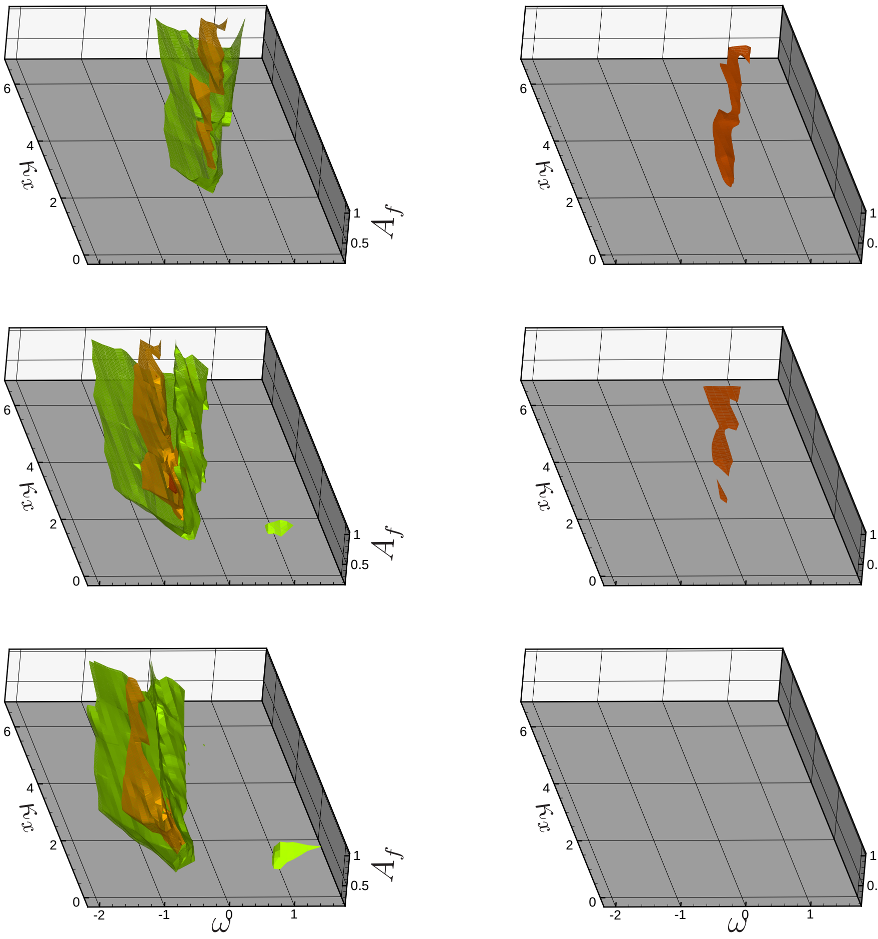

Figure 3.11: The iso-surfaces of drag reduction value $R = 0.3$, 0.4 and 0.45 (left column) and $S = 0.15$ (right column) at penetration lengths $\Delta = 0.01,\ 0.02,\ and\ 0.03$ from top to bottom, respectively.

However, as the penetration length Δ increases, the red ridge is shifting towards lower wave number κ_x and lower wave frequency ω. In the case of $\Delta = 0.03$, the whole large R region ($R > 0.3$) falls in the left half of the map where $\omega < 0$, or in other words, the wave is traveling in the opposite direction of the flow. Nonetheless, the penetration length Δ is not the only factor which might have caused such a 'shift'. If we examine each 3-D map individually, one can see that as the wave amplitude A_f grows, the ridge of large R also moves gradually to smaller ω. The large DI 'wedge' are bounded approximately by two straightlines starting from the origin [QRV09]. The angle between the two straightlines increases with the penetration length Δ as seen in Fig. 3.10.

Fig. 3.10 only enables the visualization of the surface of 3-D parameter space, where the results inside are also interesting, therefore the iso-surfaces of R and S in Fig. 3.10 are summarized in Fig. 3.11. The left column of Fig. 3.11 shows the iso-surfaces of R correspond to $\Delta = 0.01$, 0.02 and 0.03 from top to bottom, respectively. The iso-surfaces shown are with large drag reduction values $R = 0.3$, 0.4 and 0.45 (only the plot where $\Delta = 0.02$ has the $R = 0.45$ iso-surface). Fig. 3.11 makes the examination of the whole 3-D domain possible. It is clearly seen that in each sub-plot, as the drag reduction R increases, one has to move towards larger A_f. The maximum R occurs when $A_f = 1.0$, which is the largest forcing amplitude in the current study. Moreover, the hull shaped iso-surfaces indicate that the area of large drag reduction increase with the forcing amplitude A_f.

Similar to the SpTW_w and SpTW_bf cases, due to the consideration of the net energy saving, we did not push the drag reduction R to its real maximum value by simply increasing the wave amplitude A_f or the penetration length Δ. Therefore the maximum value of R in the present result is almost certainly not the absolute maximum in the full 4-D parameter space. However, the current parameter space is more than sufficient to give the whole picture necessary to assess the control method. The maximum drag reduction in Fig. 3.10 locates at $A_f = 1$, $\Delta = 0.03$, $\omega = -0.8$ and $\kappa_x = 1.31$ with value $R = 47\%$. Recall that in Quadrio et al [QRV09], the maximum R value found is $R = 48\%$, which is almost identical to our result.

As stated previously, by further tuning the wave amplitude A_f or the penetration length Δ, even higher R values could be expected and the body force based case will outperform its wall based counterpart by a few percentage. However, by a quick glance at the net saving maps on right column of Fig. 3.10, pursuing the absolute maximum R in the whole 4-D space is not of much interest in practice.

Energetic performance

The right column in Fig. 3.10 draws the net energy saving values S for $\Delta = 0.01$, 0.02 and 0.03, from top to bottom, respectively. Actually, the direct visualization of Fig. 3.10 does not reveal much new insights besides what we already envisaged: in general, the large wave amplitude A_f and penetration length Δ are associated with lower net energy savings due to the high demand of control power.

The right column in Fig. 3.11 shows a single iso-surface of net saving S for $S = 0.15$ in each sub-figure. In the first sub-figure, where $\Delta = 0.01$, the $S = 0.15$ iso-surface is completely lying on the plane $A_f = 0.5$. This is also where the global maximum net saving $S = 0.2$ is found ($\omega = 0.2$ and $\kappa_x = 2.62$), which is slightly higher than what have been reported in [QRV09]. By moving to the case $\Delta = 0.02$, the whole $S = 0.15$ iso-surface shifted down to the plane $A_f = 0.2$, which is the smallest wave amplitude in the current study. It is expected that by further increasing the penetration length to $\Delta = 0.03$, the $S = 0.15$ would move to even smaller wave amplitude, which is beyond the current parameter space. Therefore, when $\Delta = 0.03$, the net saving S is always smaller than 0.15 and no iso-surface is shown.

In general, the pattern exhibited in the energetic performance is very close to that of the drag reduction performance, i.e. the large net saving region shifts towards lower wave number κ_z and lower wave frequency ω.

Near wall flow structures

The instantaneous streamwise velocities on the wall-parallel $x - z$ plane at wall distance $y^+ = 4$ are plotted for the reference, a DR ($\omega = -1$, $\kappa_x = 1.31$, $A_f = 1$ and $\Delta = 0.03$) and a DI ($\omega = 0.2$, $\kappa_x = 1.31$, $A_f = 1$ and $\Delta = 0.03$) case in Fig. 3.12. The DR and DI cases have R values of 0.45 and -0.45, respectively.

Both DR and DI velocity fields exhibit streamwise modulation which is due to the body forcing provided by the flow control, however, the modulation in the DI case is much stronger. It is very apparent that the in the DR flow, streaky structures in the reference flow is largely eliminated and the near-wall velocity on average is very low. In the DI flow, the velocity fields are very much fractured into very small patches of high velocity and these small patches are modulated according to the wave. As we have argued before, the lowered near-wall velocity strongly linked with the reduced skin-friction drag while a more chaotic velocity distribution in general associates with intensified friction drag.

As mentioned before, the DI and DR cases only differ in the value of

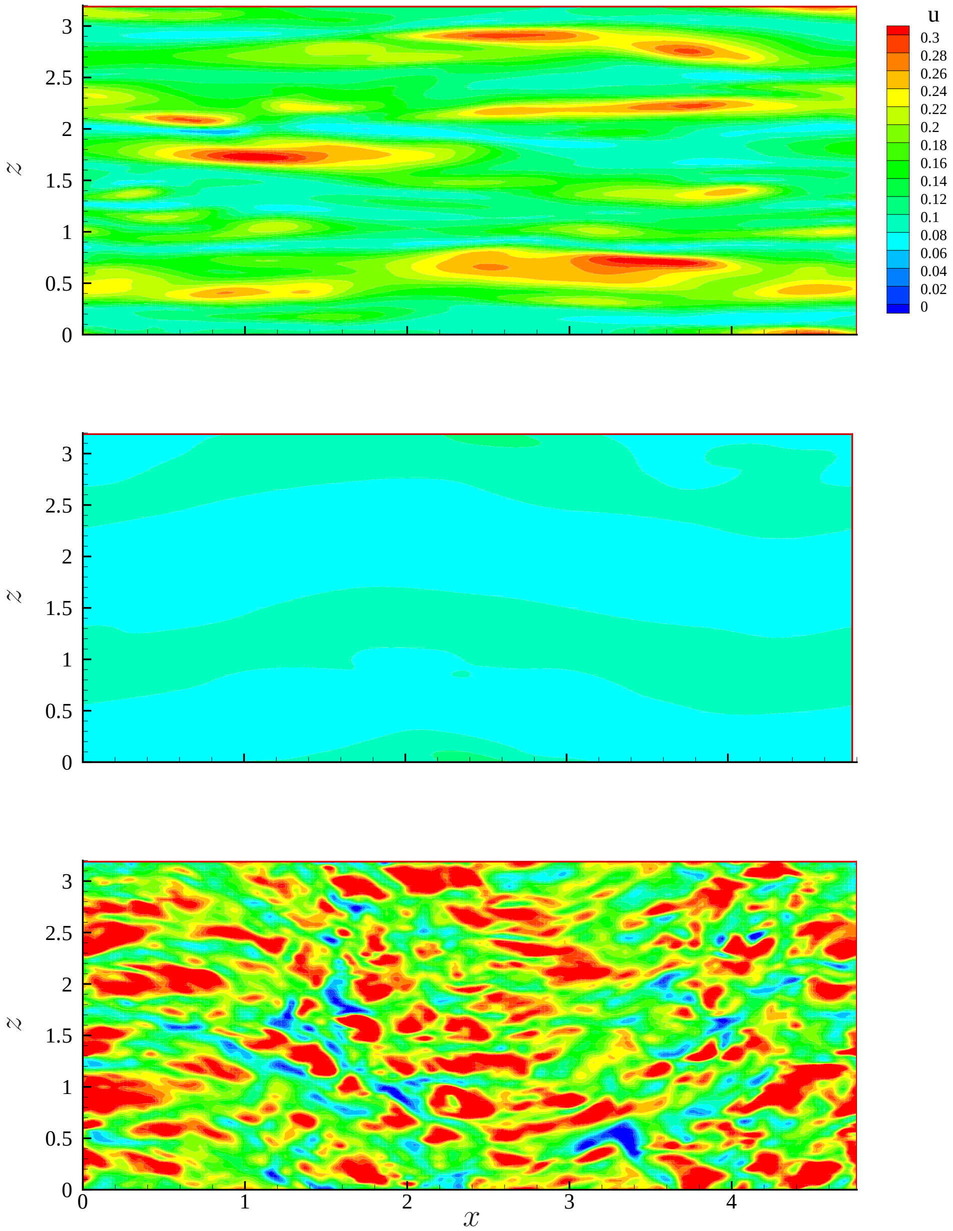

Figure 3.12: The streamwise velocity contours at $y^+ = 4$. From top to bottom: the uncontrolled flow, the DR case with $\omega = -1$, $\kappa_z = 1.31$, $A_f = 1$ and $\Delta = 0.03$, the DI case with $\omega = 0.2$, $\kappa_x = 1.31$, $A_f = 1$ and $\Delta = 0.03$.

wave frequency ω. Therefore, it is reasonable to conject that some certain phase speed are capable of collecting the near-wall structures and merge them into larger structures as in the DR flow, which could lead to drag reduction, while the unfavored frequencies are just working to further fracture the original structures into even smaller pieces, by which the skin-friction drag is escalated.

Chapter 4

Flow statistics

In the previous two chapters, three types of turbulent flow control realized by traveling waves have been presented and their drag reducing and energetic performances have been studied thoroughly by full parametric study in the waves' parameter spaces. All these three kinds of traveling waves are of great drag reducing capacity of at least 30%. Flow visualizations suggested that their near-wall turbulence cycles are altered dramatically in both DI and DR cases, and common flow structures exist. In order to have a further insight into the different traveling waves, analysis on several statistical properties of the flow are performed and compared across different waves in this chapter, including the mean velocity profile, the turbulence fluctuations, Reynolds stress, etc.

Certainly the DR flows are of much higher importance and more interests, therefore one DR case with similar R (about 0.3) value is chosen from the study of each type of wave. The chosen 3 cases are listed and numbered below:

1. Case 1 (SpTW_w): $\omega = 1$, $\kappa_z = 1.96$ and $A = 0.5$ ($R = 0.27$),
2. Case 2 (SpTW_bf): $\omega = 1$, $\kappa_z = 1.96$, $A_f = 2$ and $\Delta = 0.01$ ($R = 0.32$),
3. Case 3 (StTW_bf): $\omega = -0.8$, $\kappa_x = 1.31$, $A_f = 1$ and $\Delta = 0.01$ ($R = 0.28$).

All three cases are of similar drag reduction value R to make the them on the same ground for comparisons, which is not feasible otherwise.

4.1 Mean flow

The mean streamwise velocity profile U^+ of case 1, 2 and 3 are shown in Fig. 4.1 in comparison with that of the uncontrolled reference flow, non-

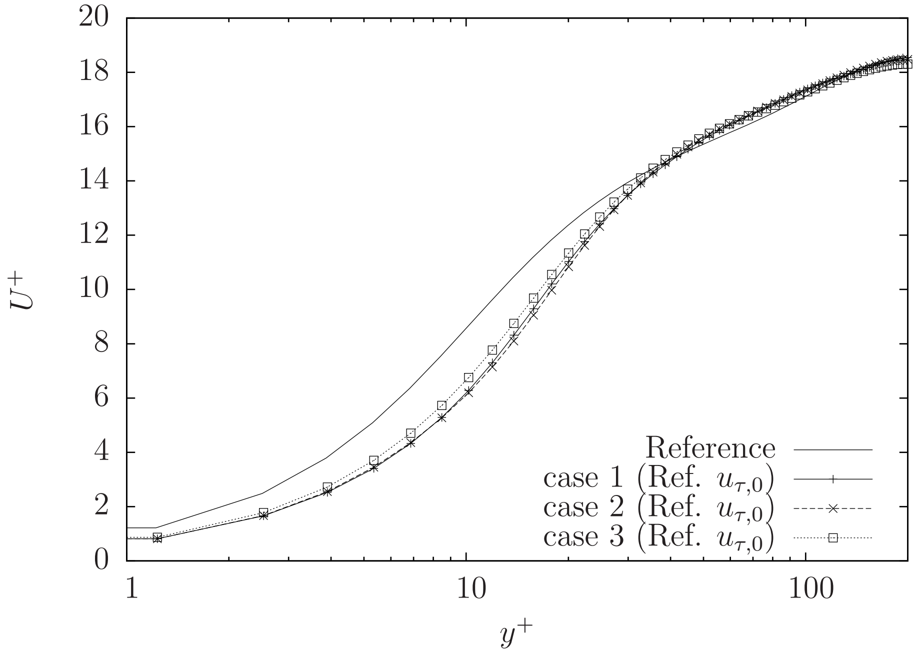

Figure 4.1: The mean velocity profiles of case 1, 2 and 3 in comparison with the uncontrolled reference flow. The velocities are scaled by canonical u_τ.

dimensionalized by the canonical viscous velocity u_τ.

The three curves of the controlled cases, although subjected to different wall turbulence control techniques, appear similar to each other. From the near-wall region where $y^+ < 10$, up to the bottom of the logarithmic law region $y^+ = 50$, the controlled flows have a smaller mean streamwise velocity than the uncontrolled flow. However, the simulation requires the mean streamwise flow rate to be the same for all cases, therefore, the near-wall velocity deficit in controlled flows are compensated by larger mean velocities in the logarithmic law and outer region where $y^+ > 50$ as shown in Fig. 4.1. Note that the mean profile from case 3 does not collapse well with that of the rest two cases right from the wall up to $y^+ = 50$, although case 3 has a similar R value as the other two cases, which indicates that the StTW alters the flow differently from the SpTW.

The friction coefficient C_f (Eq. 1.3) is proportional to the wall shear stress τ_w, therefore also to the wall-normal gradient of the mean velocity $\frac{\mathrm{d}U}{\mathrm{d}y}$. The lowered mean velocity profiles in the viscous sublayer $y^+ < 5$ suggest that their wall-normal gradients at the wall are also smaller than that corresponding to the uncontrolled flow, which coincides with the substantial positive drag reduction values reported.

Nevertheless, Fig. 4.1 is plotted by normalizing the velocities with the canonical viscous velocity $u_{\tau,0}$, which is calculated from the uncontrolled flow. It is known that in all of the three controlled cases, the skin-friction drag is reduced, so is their own viscous velocities u_τ (which is different in different cases). Therefore, more properly, the velocities ought to be normalized by each case's own viscous velocity u_τ, in order to eliminate the contributions from improper inner scaling. Different authors prefer different scaling approaches. In previous studies on spanwise wall oscillation for drag reduction, some works scaled the quantities with the reference flow's viscous velocity $u_{\tau,0}$ ([LSM94, XH05, ITYT06]) while some others used the controlled flow's own viscous velocity u_τ ([BQ96,Cho02,RW04]). Even when they are studying the same problem, which may lead to different views to the problem [QR11]. There is no simple right or wrong on the choice of scaling approaches, however, it is crucial to be aware of the physical meaning behind them.

Fig. 4.2 enables viewing the mean streamwise velocity profiles via properly scaled velocities. One of the most prominent differences between the profiles in proper inner unit and canonical inner unit lies in the near-wall region: the three curves of controlled flows collapse with the uncontrolled flow's profile in region $y^+ < 10$ in Fig. 4.2 and moreover, the as wall distance y^+ increases, the velocity profiles of controlled flows and the uncontrolled flow gradually diverge up to the centerline of the channel. The root of the differences lies of course in the choice of the scaling. Scaling with the proper inner unit, based on u_τ, is designed to make the wall shear stress τ_w^+ of different flows equalize and so is the wall-normal derivative of the mean streamwise velocity $\dfrac{\mathrm{d}U^+}{\mathrm{d}y^+}$. Therefore, the properly scaled near-wall mean streamwise velocity profiles of the reference flow, case 1, 2 and 3 collapse with each other. The area under the curve, which is the streamwise flow rate in each case, apparently are not the same anymore, which violates the constant flow rate condition imposed in the simulations. The 'violation' actually also roots in the choice of scaling. The constant flow rate constraint in the simulation is imposed in outer unit U_P. A more detailed discussion on the scaling issue could be found in Quadrio and Ricco [QR11] and Hasegawa et al. [HQF14].

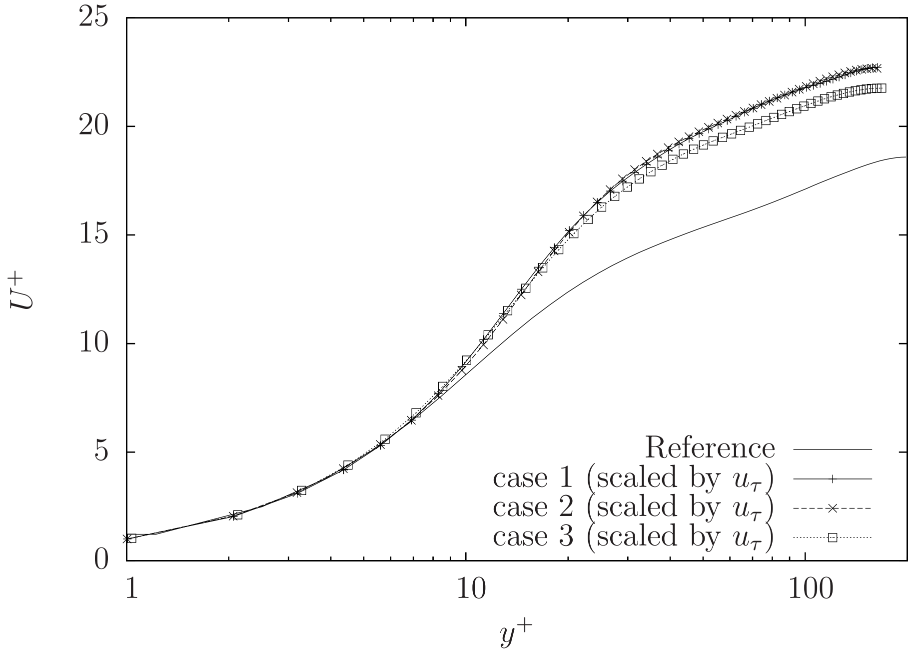

Figure 4.2: The mean velocity profiles of case 1, 2 and 3 in comparison with the uncontrolled reference flow. The velocities are scaled by the flow's own u_τ.

4.2 Turbulence intensities

The turbulence intensities, or root mean squares (RMS) of the velocity components normalized by the canonical viscous velocity u_τ are shown in Fig. 4.3. In the streamwise direction, the u_{rms} are largely declined by the traveling waves, in all three cases compare to the reference flow in the region $y^+ < 20$. Moreover, the peaks of the turbulence fluctuations u_{rms} are pushed towards the centerline of the channel by distances of 10 to 20 in wall units. Case 1 and case 2, which are controlled by SpTW, both exhibit higher near-wall turbulence fluctuation in the wall normal velocity v_{rms} than the uncontrolled flow, which is expected since as argued previously, the SpTW is capable of creating a 'synthetic' traveling wave of blowing and suction. The modulated vertical velocities would directly cause an increase in the turbulence fluctuation v_{rms}. The turbulence fluctuation of spanwise velocity w_{rms} is directly affected by the harmonic traveling wave acting either on the wall or on the near-wall bulk flow and w_{rms} values of the controlled flows could even reach several orders higher than the reference flow's fluctuation. Recall that case 1 is from the SpTW_w study, where the forcing is on the wall, therefore the maximum w_{rms} occurs right at the wall. The body forcing based case 2 and 3, on the other hand, have rigid walls and thus the peaks of w_{rms} locate very near the wall but not on the wall.

It has been seen that the turbulence fluctuations in the controlled flows are altered by the traveling waves, especially the streamwise velocity fluctuation u_{rms} are suppressed which is in line with the reduced drag. The same question should be addressed here: what if the velocity fluctuation changes its scaling from canonical inner unit to proper inner unit? Fig. 4.4 attempts to answer this question by plotting the RMS of the velocity components scaled properly, i.e. the normalization is performed by each case's own viscous velocity u_τ.

Qualitatively, the wall-normal and spanwise component of the velocity fluctuation v_{rms} and w_{rms} are almost identical to their canonical $u_{\tau,0}$ scaled counterparts. Thus, the arguments made on v_{rms} and w_{rms} are justified. The streamwise component u_{rms} of the controlled flows, on the other hand, almost have peak similar to the reference flow and still with a shift outwards from the wall. The differences between the profiles of u_{rms} are simply caused by the choice of scaling (by $u_{\tau,0}$ or u_τ). Therefore, it is important to consider the scaling issue before making definite statement.

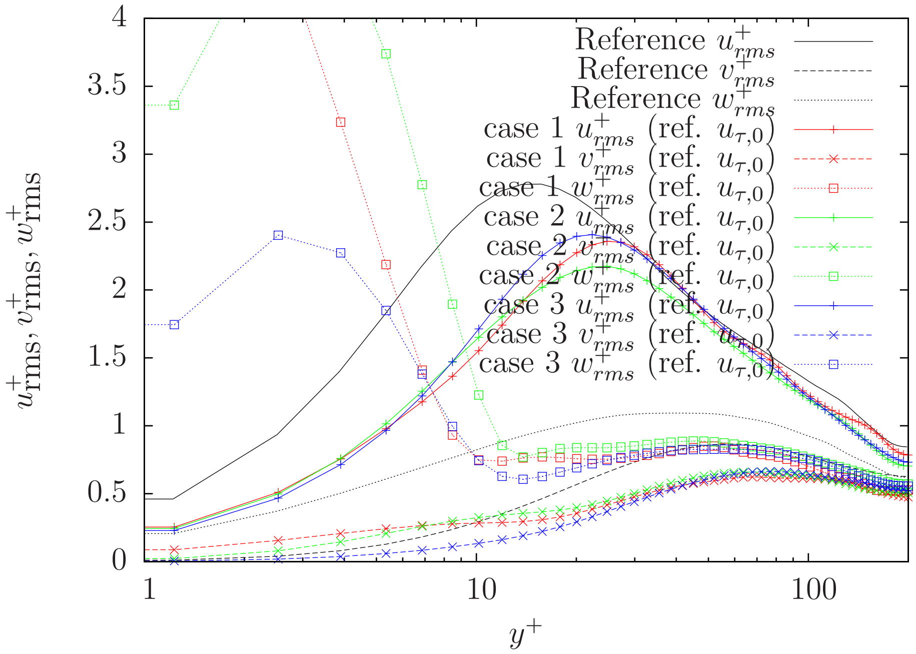

Figure 4.3: Turbulence intensity components of case 1, 2 and 3 in comparison with the uncontrolled reference flow. The velocities are scaled by canonical $u_{\tau,0}$.

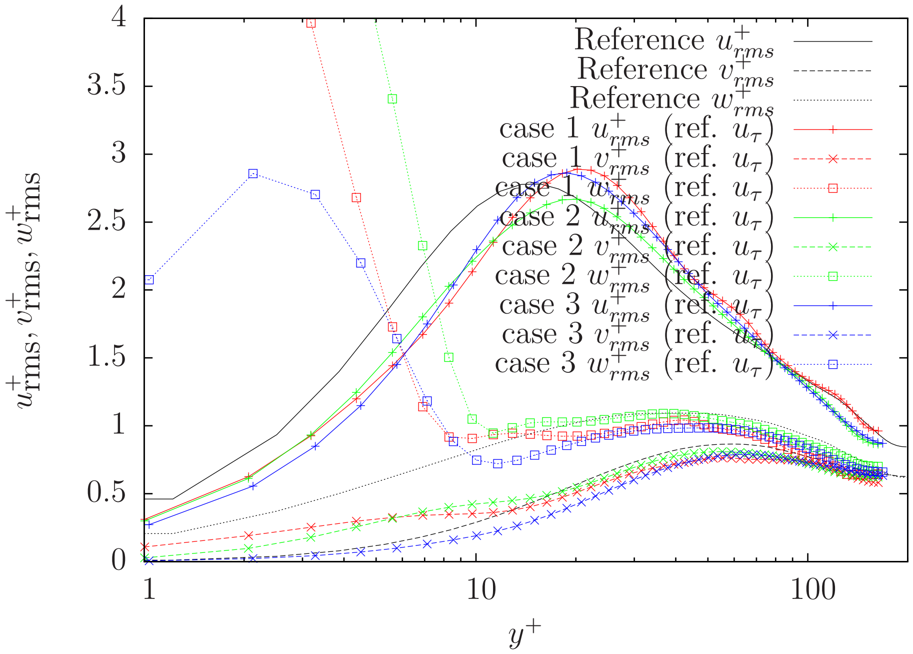

Figure 4.4: Turbulence intensity components of case 1, 2 and 3 in comparison with the uncontrolled reference flow. The velocities are scaled by the flow's own u_τ.

4.3 Lumley triangle

Lumley and Newman [JG77] demonstrated that all possible turbulence states must lie within the turbulence triangle in invariant coordinates, where the ordinate is the negative second invariant of the Reynolds stress anisotropy tensor II while the abscissa is the third invariante of that tensor III. Here we adopt the presentation of Lumley triangle given by Pope [Pop00], in which, two new variables η and ξ are defined as:

$$\eta^2 = -\frac{II}{3},\ \xi^3 = \frac{III}{2}. \tag{4.1}$$

The Lumley triangle represented in the $\xi - \eta$ coordinate system also bounds all possible turbulence states, which is shown in Fig. 4.5. Together with the Lumley triangle, the turbulence flow states from the case 1, case 2 and case 3 are plotted in Fig. 4.5 for different wall-normal distances y^+ (scaled by flow's own u_τ). Note that the contributions directly from the harmonic traveling wave have been removed. Generally, all three curves follow similar trends: as the wall distance increases, the turbulences first become more anisotropic until they have reached their maximum at about $y^+ = 10$, then they almost follow the axisymmetric or the 'cigar-shaped' turbulence boundary line [CL01] up to the outer region, which indicates the domination of the turbulence fluctuation u_{rms} over the rest two components v_{rms} and w_{rms}. It is observed that the differences among the 3 cases mainly lie in the near wall region, which is the top-right corner of the figure. In the near wall region $y^+ < 10$, case 2 and case 3 exhibit some 2-D characteristics which is due to the impermeability of the wall. On the other hand, case 1 already shows strong axisymmetric properties in the near wall region rather than 2-D characeristics, which implies that the turbulence fluctuation component w_{rms} is largely diminished in the near wall region. The difference is most probably due to the difference between wall based control and body force based control.

4.4 Reynolds stress and FIK identity

The Reynolds stress tensor directly reflects the state of the turbulent flow, and bear important links to the turbulence skin-friction drag. Due to the different physical natures of SpTW and StTW, the Reynolds stresses are plotted in different figures, the details of which are explained later.

Fig. 4.6 shows the components $\overline{u'u'}^+$ and $\overline{u'v'}^+$ of the Reynolds stress tensor for the reference, case 1 (SpTW_w) and case 2 (SpTW_bf) from top

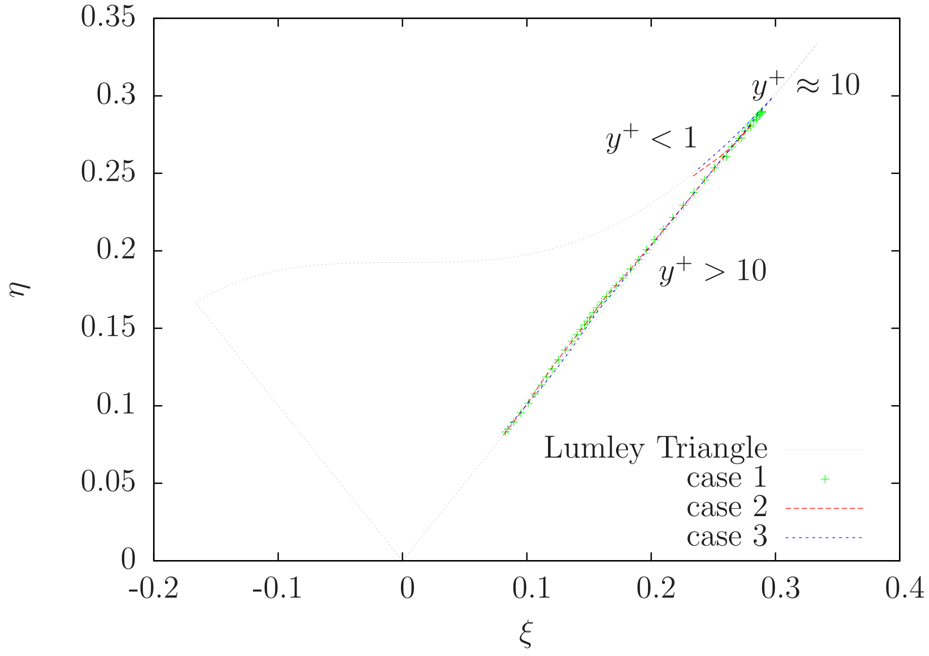

Figure 4.5: The Lumley triangle on the $\xi - \eta$ plane. Different symbols correspond to the turbulence states recorded from different flows (case 1, case 2 and case 3) measured at different wall-normal distances y^+, scaled by proper u_τ.

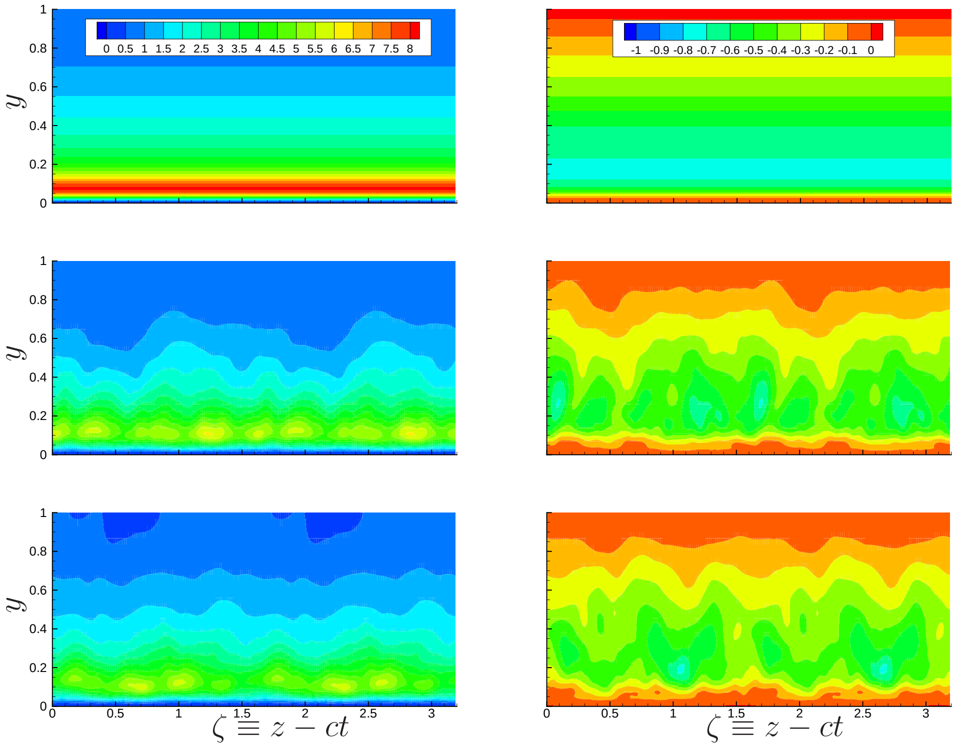

Figure 4.6: The phase-averaged Reynolds stress components $\overline{u'u'}^+$ (left column) and $\overline{u'v'}^+$ (right column) on the $y-z$ plane for the reference, case 1 (SpTW_w) and case 2 (SpTW_bf) from top to bottom. Scaled by canonical $u_{\tau,0}$.

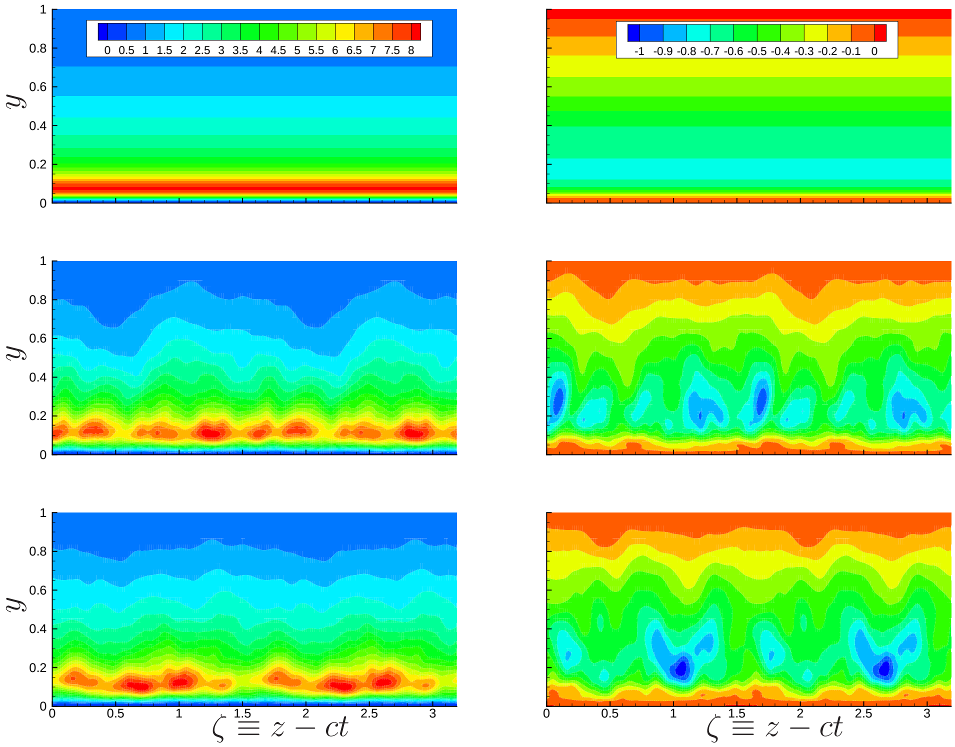

Figure 4.7: The phase-averaged Reynolds stress components $\overline{u'u'}^+$ (left column) and $\overline{u'v'}^+$ (right column) on the $y - z$ plane for the reference, case 1 (SpTW_w) and case 2 (SpTW_bf) from top to bottom. Scaled by flow's own u_τ.

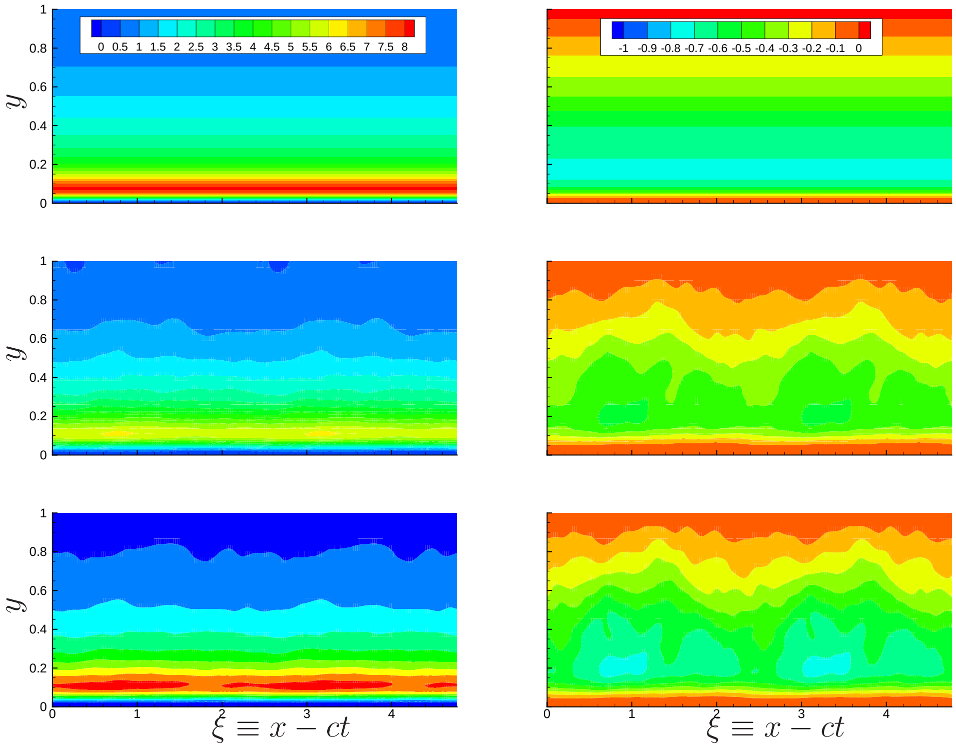

Figure 4.8: The phase-averaged Reynolds stress components $\overline{u'u'}^+$ (left column) and $\overline{u'v'}^+$ (right column) on the $x-y$ plane for the reference and case 3. Case 3 figures shown in the middle are scaled by canonical u_τ and in the botton row are scaled by the flow's own u_τ.

to bottom on the cross-section of the channel flow, which are scaled by the canonical $u_{\tau,0}$. In the reference flow, the averaging procedure is carried out, as usual, over the homogeneous directions and time. In the controlled flow, besides the same averaging operation, in the spanwise z direction, the flow is averaged at different oscillation phases $\zeta = z - ct$ (phase averaging). In the reference flow, the Reynolds stress components are confirmed not to depend on the z coordinate. In both case 1 and case 2, the Reynolds stresses are modulated in spanwise direction and the intensities are obviously weakened compare to the reference flow. Fig. 4.7 plots the same quantities but scaled properly by u_τ. The differences resulted from the different choices of inner unit are evident. Therefore, again it is highly important to interpret the results accordingly.

Fig. 4.8 shows the Reynolds stress components $\overline{u'u'}^+$ and $\overline{u'v'}^+$ for the reference and case 3 (StTW_bf) on the $x-y$ plane of the flow. Case 3 is shown with different inner unit based on $u_{\tau,0}$ and u_τ, respectively. Here, both flows are averaged in homogeneous direction z and time. Since the wave is modulated along x direction, case 3 is further averaged at oscillation phases $\xi = x - ct$. In this case, the attenuation of the Reynolds stress in the near wall flow is quite significant.

The attenuation of the Reynolds stresses, especially the component $\overline{u'v'}$ directly affect the wall friction. Fukagata et al [FIK02] derived an expression that links the Reynolds stress component $\overline{u'v'}$ and the drag coefficient analytically, which is now known as the FIK identity. It provides a way to quantitatively decompose total turbulent skin friction drag into contributions from a laminar term, a turbulent term, the spatial and temporal development term, etc.

Under the condition of constant flow rate, by exploiting the homogeneity of the flow in either the streamwise direction (case 1 and 2) or the spanwise direction (case 3), the FIK identity for the present control strategies, becomes:

$$C_f(z) = \frac{9}{Re_P} + \frac{27}{2}\int_0^1 (1-y)\langle -\overline{u'v'}\rangle \mathrm{d}y - \frac{27}{4}\int_0^1 (1-y)^2 (I_z'' + \frac{\partial \langle u \rangle}{\partial t})\mathrm{d}y, \quad (4.2)$$

where C_f is the friction coefficient defined in Eq. (1.3) and modulated along the spanwise direction; the notation $\langle f \rangle$ implies averaging a generic function $f(x,y,z,t)$ along the homogeneous direction (x for SpTW and z for StTW), whereas the fluctuations f' and f'' are defined as:

$$f'(x,y,z,t) = f(x,y,z,t) - \langle f \rangle (y,z,t), \quad (4.3)$$

$$f''(y,z,t) = \langle f\rangle(y,z,t) - \int_0^1 \langle f\rangle(y,z,t)\mathrm{d}y. \tag{4.4}$$

Note that Eq. 4.2 assumes homogeneity in x direction, which is thus only valid for case 1 and 2. In case 3, the body forcing is modulated in the streamwise direction, therefore the homogeneity occurs in the spanwise direction z. After a simple modification to Eq. 4.2, the friction coefficient decomposition for case 3 is written as:

$$C_f(x) = \frac{9}{Re_P} + \frac{27}{2}\int_0^1 (1-y)\langle -\overline{u'v'}\rangle \mathrm{d}y - \frac{27}{4}\int_0^1 (1-y)^2 (I''_x + \frac{\partial \langle u\rangle}{\partial t})\mathrm{d}y. \tag{4.5}$$

One has to note that in Eq. 4.5, the notation $\langle f\rangle$ still implies averaging operation in the homogeneous direction, but here, that direction is z instead of x. Therefore the definition of the fluctuations f' and f'' in Eq. (4.3) and (4.4) has to be changed accordingly.

It is worthwhile to be aware that Fukagata et al [FIK02] non-dimensionalized the variables by twice of the bulk velocity $2U_b$ and the centerline velocity U_P is used in this work. Therefore, in the limiting steady case, the Eq. (4.2) and (4.5) reduce to a slightly different form from that in the original paper.

The right hand side of Eq. 4.2 and 4.5 accounts for the laminar contribution (the first term), the turbulent contribution (the second term) and the inhomogeneous (spatial) and transient (temporal) contribution (the third term). The turbulent contribution and the spatial/temporal contribution weights linearly and quadratically decrease with distance from the wall, respectively.

If one applies an average along the inhomogeneous direction to both sides of Eq. 4.2 and 4.5, the global drag coefficient is decomposed as:

$$C_f = \frac{9}{Re_P} + \int_0^1 (1-y)\left\langle -\overline{u'v'}\right\rangle \mathrm{d}y. \tag{4.6}$$

where $\langle\cdot\rangle$ represents the averaging on the $x-z$ plane.

Note that the global drag coefficient is not a function of x or z anymore. It is noticed that after taking the mean in the inhomogeneous direction, the temporal/spatial term does not exist in the final equation. By this means, it becomes possible to decompose the global drag coefficient into only two terms: the laminar component and the turbulent component.

The integrand of the second term (the turbulent component) of Eq. (4.6) is shown in Fig. 4.9 for case 1, 2, 3 and the reference flow. The contribution of different dynamical terms to the drag is shown in Table 4.1. In Fig. 4.9, the turbulent components of case 1, 2 and 3 are all significantly smaller than that

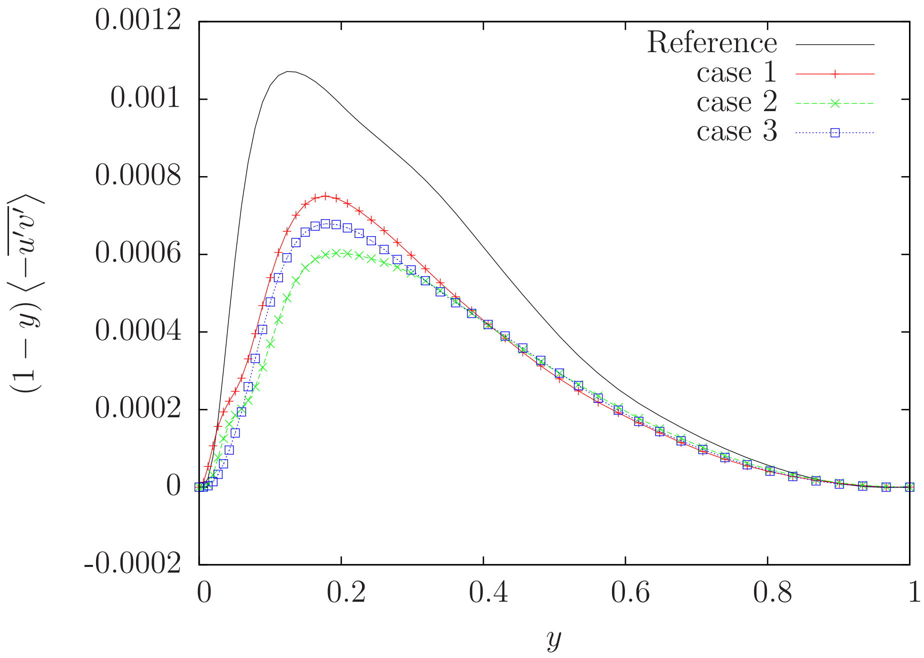

Figure 4.9: The distribution of the turbulent component along y axis for the uncontrolled, case1, 2 and 3.

of the reference flow. Qualitatively, it is possible to compare the turbulence drag of the three cases by measuring the area below the curves, even by naked eyes. The conclusion is hardly of any difference from the quantitative results summarized in Table 4.1, where the laminar and turbulent contribution is calculated based on the FIK identity and the total drag is a direct output from DNS. The minor discrepancies shown in the numbers in Table 4.1 might be due to the uncertainties associated with the DNS simulations. In region $y < 0.05$ or $y^+ < 10$ (scaled by reference u_τ), case 1 and case 2 show small 'bump' in their drag's turbulence components, which is not present in case 3. Thus, the 'bump' is associated with the SpTW control and contributes the turbulence skin-friction drag. The formation of the 'bump' might also be traced back into the synthetic blowing and suction jets created by the SpTW.

Drag Contribution (in 10^{-3})			
	Laminar	Turbulent	Total
uncontrolled	1.89	5.86	7.88
case 1	1.89	4.00	5.72
case 2	1.89	3.57	5.28
case 3	1.89	3.73	5.66

Table 4.1: The drag decomposition of the uncontrolled flow, case 1, case 2 and case 3.

Chapter 5

SpTW_bf: exploiting DBD plasma actuators

The flow control devices are typically of finite size, therefore the forcing generated by the device will exhibit strong discretization effect. For instance, the SpTW_bf studied in the previous chapter idealized the devices. In reality, the Lorentz force profile along the spanwise direction will look like what is shown in Fig. 5.1. This chapter deals with the numerical model DBD plasma actuators, which is used in turbulence flow control (e.g. [JCJS06a], [CJW11]). A numerical model for the DBD plasma actuator to capture its essential body force generating characteristics is built first, and then the SpTW_bf is revisited by using the validated numerical model in DNS to reveal the discretization effect of such a flow control device in wall turbulence control. The work in this chapter was performed while the author was on a 3-month visit to Prof. Kwing-So Choi's research group at the University of Nottingham.

5.1 DBD plasma actuator and its numerical model

As an alternative to the Lorenz force generating electro-magnetic control devices, plasma actuators are capable of providing an induced momentum to the fluid by using high voltage electrical discharges. In active flow control, plasma actuators have several advantages: 1) they are fully electrical with no moving parts; 2) they have very short response time (in the order of micro seconds); 3) they are easy to be attached on existing surface without the need of extensive modification to the underlying structure and 4) they are cheap to manufacture ([WCF$^+$13]).

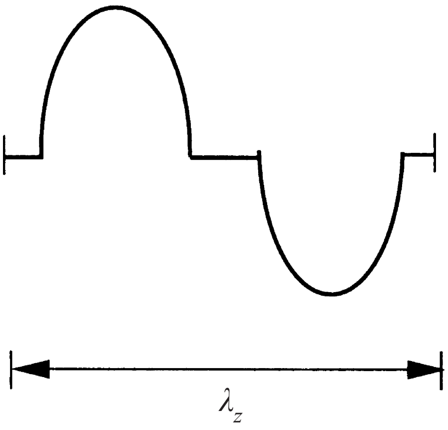

Figure 5.1: The sketch of the "two-bump" Lorentz force function in the spanwise direction of one wavelength. Taken from [DSK02].

The surface DBD plasma actuator is composed of two electrodes, one lying on the surface while the other one surrounded by the dielectrical material as shown in Fig. 5.2. When the AC voltage source is applied to the surface electrode and the electrode encapsulated in the dielectrical material is earthed, the potential difference between the two electrodes will increase. As soon as the difference exceeds the electric breakdown limit, electrons are emitted from the surface electrode and deposited on the dielectric surface. The air is therefore weakly ionized by the released electrons, and referred as 'plasma'. The plasma jet can be used to manipulate flow to provide desired control performances.

5.1.1 Numerical model of DBD plasma actuators

The complex working mechanism of the DBD plasma actuator is not in the scope of this dissertation, although it is highly important in the search for proper numerical models. Interested readers may refer to Jukes et al. [JCJS06b] and Corke et al. [CEW10] for more detailed description of the DBD plasma actuators. Our target is to build a model which describes the characteristics of the DBD plasma actuator reasonably in the DNS simulation. Since a direct measurement of the force field created by the DBD plasma jet in the boundary layer is impossible, many authors have proposed simplified models that can capture the DBD plasma characteristics fairly well. Shyy's model [SJA02] is widely used because of its simplicity and previous use in turbulence simulations [Ela12].

The schematic diagram of the field strength profile is illustrated in Fig.

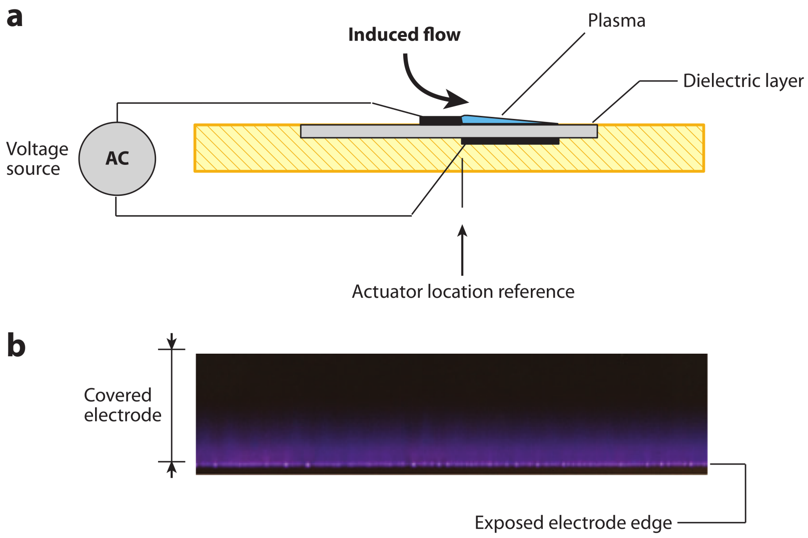

Figure 5.2: Schematic illustration of a single-dielectric barrier discharge plasma actuator. Taken from [CEW10].

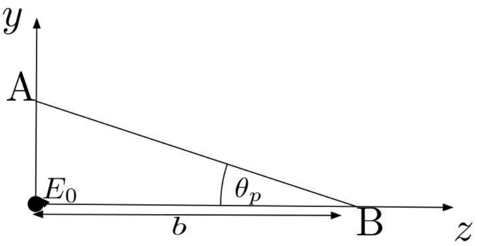

Figure 5.3: Schematic of the plasma profile. A-B represents the boundary where the electric field strength outside the line is too weak to ionise the air. E_0 is the point where the distance between the electrodes are minimum. Taken from [Ela12]

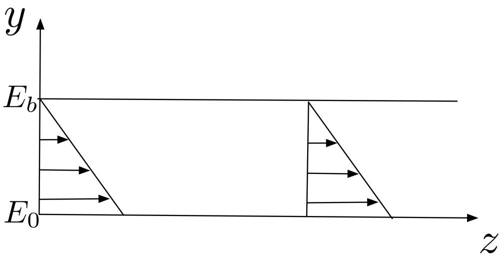

Figure 5.4: Schematic of the uniform plasma profile. Taken from [Ela12]

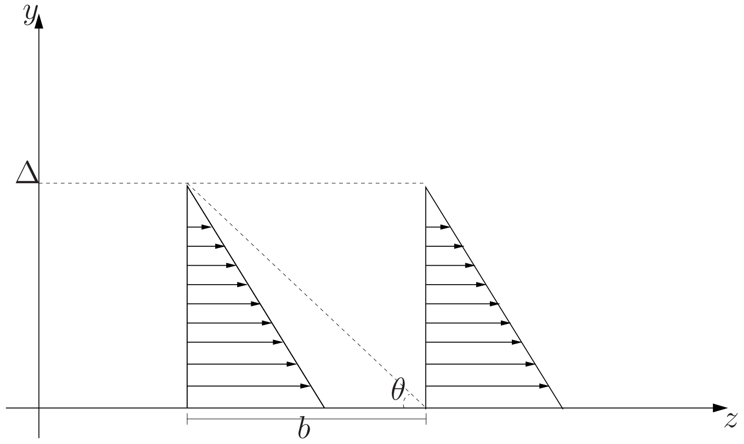

Figure 5.5: The profile of the body force F_z in the vertical y direction. b is the width of the body force generated by the plasma.

5.4. Note that Fig. 5.4 is directly taken from Elam [Ela12], in which the uniform plasma profile is already adapted from the original work from Shyy [SJA02], which is shown in Fig. 5.3. E_0 represents the point of minimum distance between the electrodes and hence maximum electric field strength, b is the width of the profile and θ_p is the angle that determines the profile height. The electric field strength E generated by the uniform plasma actuator model is written as ([Ela12]):

$$E(y,z) = E_0 - \frac{E_0 - E_b}{b\tan\theta_p} y. \tag{5.1}$$

Based on the electrical field strength variation shown Fig. 5.4, the body force profile is built as shown in Fig. 5.5. The body force is maximum on the wall where $y = 0$ and decreases linearly with wall distance. The body force deceases at $y = \Delta = b\tan\theta$. The wall normal dependency of the forcing intensity is uniform across the profile width b. However, such a forcing will create a step change in z direction cross the boundaries of the forcing profile, which is hardly the situation in the real flow, and will bring difficulties in numerical simulation, especially the spectral method based DNS. In order to avoid the problems associated with the step change, we multiply the forcing profile shown in Fig. 5.5 by a squared cosine window function. By such a windowing operation, we can maintain the force amplitude and the Fourier modes of the force decay to zero very rapidly, therefore the numerical challenges are avoided.

The DBD plasma actuator is modeled as a thin stripe of "plasma" area laid on the wall along x direction, which will create a body force f_z in the z

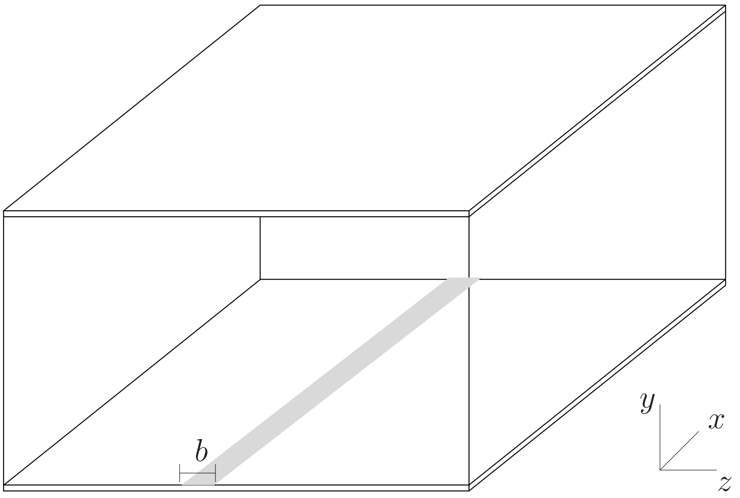

Figure 5.6: The sketch of the plasma "stripe" and the simulation domain. b is the width of the body force generated by the plasma.

direction. The body force f_z is invariant in x direction and the distribution of which is shown in Fig. 5.6.

In the 3-D simulation domain, the body force f_z is therefore expressed as:

$$f_z(x,y,z) = \begin{cases} A_f \cos^2(\frac{z}{b}\pi)\frac{\Delta - y}{\Delta}, & \text{if } z \in [-b/2, b/2] \text{ and } y \in [0, \Delta] \\ 0, & \text{otherwise} \end{cases} \tag{5.2}$$

Note that in Eq. (5.2), the midpoint of the DBD plasma forcing profile is assumed to be located at the origin point ($z = 0$), which should change accordingly as the position of the DBD plasma actuator changes.

5.1.2 Non-dimensionalization

Recall that in the DNS code, all the variables are non-dimensionalized by the reference length scale h^* (half of the channel height), and the reference velocity is chosen to be U_P^*. However, the reference velocity may vary for convenience. Temporarily, the reference velocity in this case is simply denoted as U_{ref}^* here, the meaning of which will be determined later. As a result, dimension-free time is scaled with $\frac{h^*}{U_{ref}^*}$ in the simulation. The Reynolds number is written as $Re = \frac{U_{ref}^* h^*}{\nu^*}$. In the previous chapters, we have been

Case	b	θ	A_f	U_0
1	0.1	10°	2	0.23
2	0.1	10°	3	0.30
3	0.1	10°	4	0.35
4	0.1	10°	5	0.41
5	0.1	10°	6	0.45
6	0.1	10°	7	0.50

Table 5.1: The force parameters of different cases.

using the centerline velocity U_P^* of a laminar channel flow which has the same flow rate as the underlying turbulent channel flow as the reference velocity, from which, the Reynolds number is then calculated. However, in this particular study of the starting vortex in quiescent fluid, there exists no explicit prescribed reference flow rate.

In [WC12], the lengths are made dimensionless following the operation $l = l^* U_0^* / \nu^*$, where U_0^* is the maximum velocity induced by the DBD plasma actuator to be determined later. Temporarily, the dimensionless quantities used in the DNS simulations are denoted with subscript 'DNS', thus, $l_{DNS} = l^*/h^*$. A simple substitution links the dimensionless lengths in [WC12] and DNS simulation:

$$\begin{aligned} l &= \frac{l^* U_0^*}{\nu^*} \\ &= \frac{l_{DNS} h^* U_0^*}{\nu^*} \\ &= l_{DNS} Re_{DNS} U_{0,DNS} \end{aligned} \tag{5.3}$$

Eq. (5.3) makes the comparison between the results from DNS and the experiment results from [WC12] feasible. Similarly, one can also find the relationship of dimensionless time of the DNS ($t_{DNS} = t^* U_{ref}^* / h^*$) and the experiment in [WC12] ($t = t^* U_0^{*2} / \nu^*$):

$$t = t_{DNS} Re_{DNS} U_{0,DNS}^2 \tag{5.4}$$

In the rest part of the chapter, unless otherwise stated, all the dimensionless quantities are scaled according to the DNS convention.

5.2 Model Validation

In the previous section, a rather simple model to represent the body force generated by the DBD plasma actuator has been built based on the the works

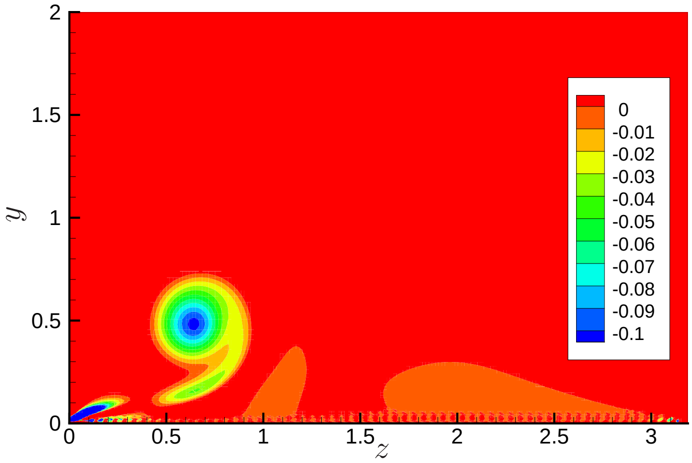

Figure 5.7: The starting vortex in Case 6, shown by visualizing the λ_2 value.

from other authors. Before implementing such a simple model in flow control problems, it is necessary to check the validity of the model to avoid unreasonable simplification. Whalley and Choi [WC12] experimentally investigated the starting vortex generated by the DBD plasma actuator in a channel of quiescent fluid. They have measured the dynamical evolution of the starting vortex caused by a sudden activation of the plasma actuator. For the validation of our simplified DBD plasma model, the very same experiment is performed numerically by DNS and the results will be compared accordingly. The vortex is recognized by the λ_2 criterion and the core of the vortex is localized by searching the point with the smallest velocity within the detected vortices. Fig. 5.7 enables the visualization of the starting vortex in Case 6, by showing the λ_2 value in the whole field.

In total, 6 different DNS tests were carried out, which are summarized in Table 5.1. The midpoint of the modeled DBD plasma forcing profile is located at $z = 0$. All the tests share the same parameter of forcing profile width $b = 0.1$ (which corresponds to $b^+ = 20$ in turbulent channel flow with $Re_\tau = 200$) and the profile angle $\theta = 10°$. The 20 wall unit profile width and the 10° forcing profile angle has been tested in [Ela12] and shown good agreement with experiments. Forcing profile width larger than 20 wall units might become a less practical assumption for real DBD plasma actuators, as suggested by Dr. Timothy Jukes in a private discussion. The tests are only different in the choice of force amplitude parameter A_f. The U_0 column in Table 5.1 is an a-posteriori parameter defined as the maximum velocity

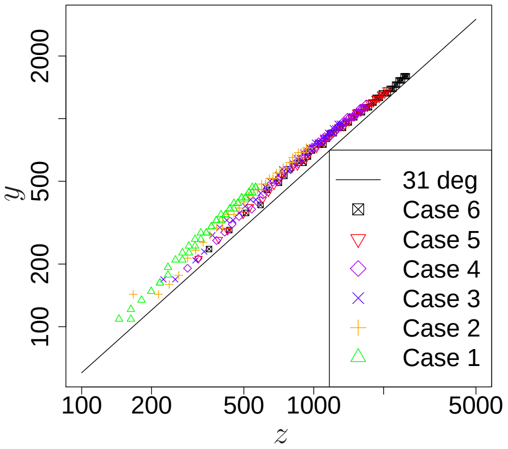

Figure 5.8: The trajectory of the vortex core from 6 DNS cases. The quantities are made dimensionless according to [WC12].

induced by the DBD plasma jet.

5.2.1 Vortex Trajectory

The smoke flow visualization and PIV experiments observe that as the DBD plasma is initiated, a starting vortex is created and travels at 31° to the wall [WC12]. The very same problem with 6 different DBD plasma forcing intensities have been performed, the parameter of which are shown in Table 5.1. The positions (z and y coordinates) of the vortex core are plotted in Fig. 5.8 at different moments during the simulation, for 6 different forcing intensities respectively. The 31° line starting from the origin point ($z = 0$, $y = 0$) is also presented in the figure to assist the visualization. The scattered points do not exactly collapse with the 31° line, however, the agreement is fairly good especially with large force amplitude A_f.

5.2.2 Vortex Evolution

The dynamical evolution of the vortex characterizes the time-dependent behaviour of the flow. Whalley and Choi [WC12] reported that the non-dimensional horizontal position of the vortex core z_c and the non-dimensional time t follow the relation: $z_c = 1.85t^{0.71}$ and a similar relation $y_c = 1.1t^{0.71}$ is maintained by the vertical position and the time. It is worth to note that here the non-dimensionalization is made according to the convention in [WC12],

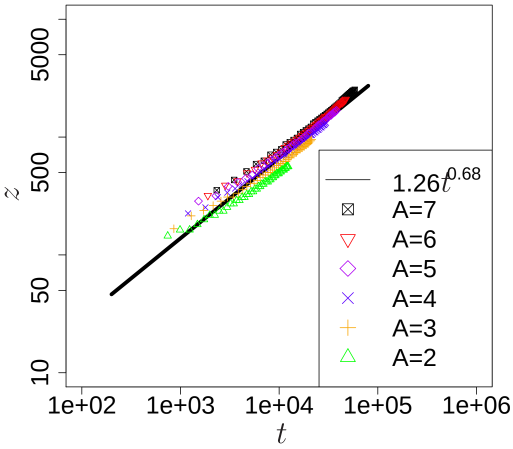

Figure 5.9: The x-position of the vortex core in 6 DNS cases. The quantities are made dimensionless according to [WC12].

moreover, the original notation x_c is changed to z_c since the horizontal axis used in this work is z. The coefficients are obtained from a linear least-square fitting of the experimental data. The results are quite similar to the analysis given by Cantwell [Can86] if one approximates the exponent 0.71 by a close rational number $\frac{2}{3}$.

Fig. 5.9 and 5.10 plot the dimensionless z and y positions of the vortex core as a function of dimensionless time (according to the convention in [WC12]) from the DNS tests, respectively. The black straight lines are drawn by linear fitting the scatter points, which suggest that $z_c = 1.26t^{0.68}$ and $y_c = 1.26t^{0.65}$. The fitted exponents 0.68 and 0.66 indicate strikingly good agreements with the rational number $\frac{2}{3}$ given by Cantwell [Can86] and Whalley and Choi [WC12].

After being validated in two different tests of dynamical behaviour of the starting vortex, it is convinced that the body force model in DNS given by Eq. 5.2 is able to mimic the essential flow control performances of real DBD plasma actuators fairly well. In the next section, the spanwise traveling waves (SpTW_bf) by different arrangement of the DBD plasma actuator models in turbulent channel flows will be presented and their drag reducing performances are evaluated.

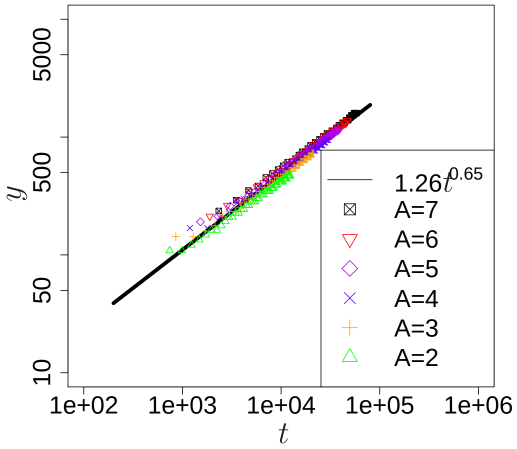

Figure 5.10: The y-position of the vortex core in 6 DNS cases. The quantities are made dimensionless according to [WC12].

5.3 DBD plasma actuators in turbulent channel flow

5.3.1 A direct comparison with experiment

Whalley and Choi [WC11] experimentally observed the near wall structure modified by the SpTW_bf generated by the DBD plasma actuators. The 4-phase discretized traveling wave is generated by the actuator array and is of wave length $\lambda^+ = 500$ and period $T^+ = 82$, both in wall units. They have tested two types of waves, namely the unidirectional and bidirectional forcings. The DBD plasma actuator is only activated in one direction per phase under unidirectional forcing and two opposite directions per phase under bidirectional forcing. They have measured the evolution of the near wall structures produced by the discretized traveling wave and also the mean velocity profile, which is shown in Fig. 5.11 (Fig. 5 in [WC11]).

This work implements almost identical experimental setup in DNS simulation of a turbulent channel flow (only the traveling wave with bi-directional forcing). The simulation domain is of size $L_x \times L_y \times L_z = 3.33 \times 2 \times 2.22$ differs from the previously used moderated sized domain. The upscaling of the simulation domain is required since fitting two wave lengths in the spanwise direction of the domain will require $L_z^+ = 1000$, i.e. $L_z = 2.22$ given that $Re_\tau = 450$. The Reynolds number is quite close to the value $Re_\tau = 435$ used in [WC11] and it is believed that the 3% difference in the Reynolds number

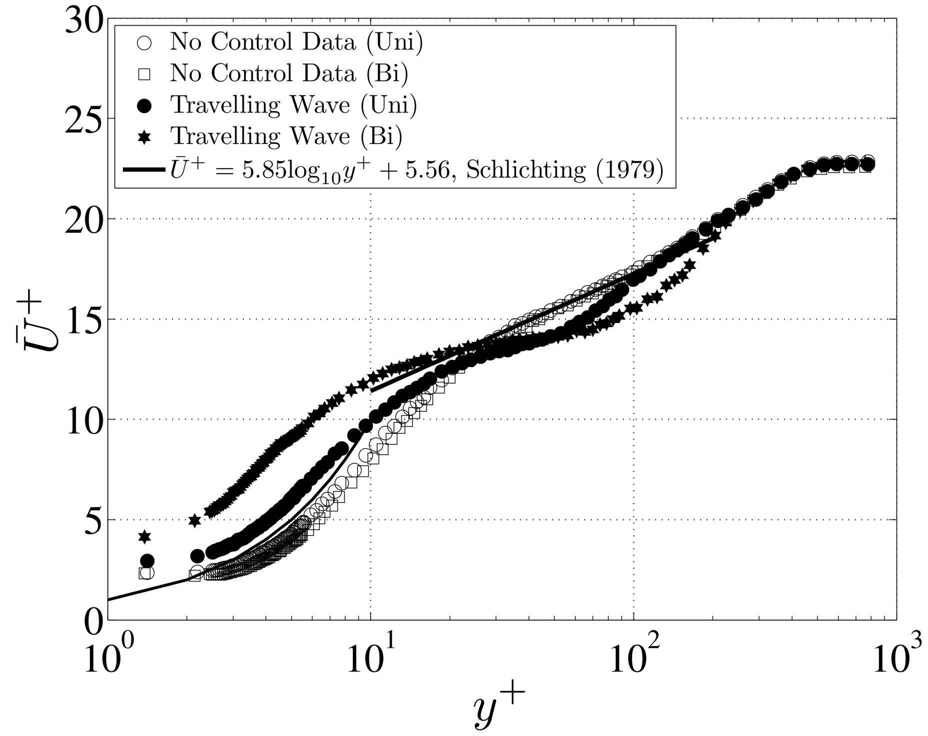

Figure 5.11: Mean velocity profile in turbulent boundary layer with spanwise traveling-wave excited by plasma. Taken from [WC11]

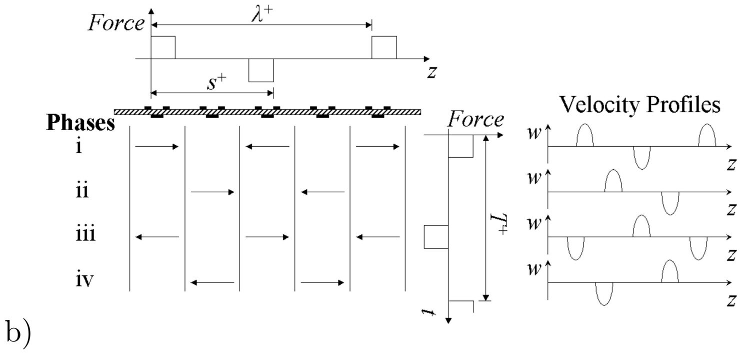

Figure 5.12: Schematic representation of bidirectional 4-phase spanwise traveling waves. Taken from [WC11].

will not bring significant difference in the conclusions. The wave frequency is chosen to be $\omega = 1.277$, which corresponds to period $T^+ \approx 82$ in wall unit. In total 8 DBD plasma actuators are aligned $\frac{\lambda^+}{4}$ away from each other in the spanwise direction. The activation of each actuator follows the 4-phase spanwise traveling wave schematic representation shown in Fig. 5.12 (Taken from Fig. 2(b) in [WC11]).

Fig. 5.13 shows the streamwise velocity profile from DNS study, which is quite close to the curve of bidirectional forcing in Fig. 5.11 qualitatively comparable, although in the near-wall region ($y^+ < 10$), the mean velocity is slightly less than that from the experiment and near the centerline, the flow rate of the controlled case from DNS surpasses that of the uncontrolled flow. However, this particular setting of traveling wave is not found to be able to reduce the turbulence skin-friction drag, which has been conjected in [WC11]. Compare to the uncontrolled case, the drag is increased by 150%. This could also be seen from Fig. 5.13, in which, in the near wall region, the wall normal gradient of the streamwise velocity is significantly higher than that of the uncontrolled flow.

5.3.2 A re-visit to SpTW_bf

In order to investigate in the drag reduction performance of such a discretized traveling wave, a parametric study is almost indispensable. However, it is possible to control the number of simulations to a very small number since the importance here is to understand the behaviour of the discretized traveling wave in comparison with the ideal sinusoidal traveling wave. The ideal SpTW_bf has been explored rather extensively and in this section, two drag

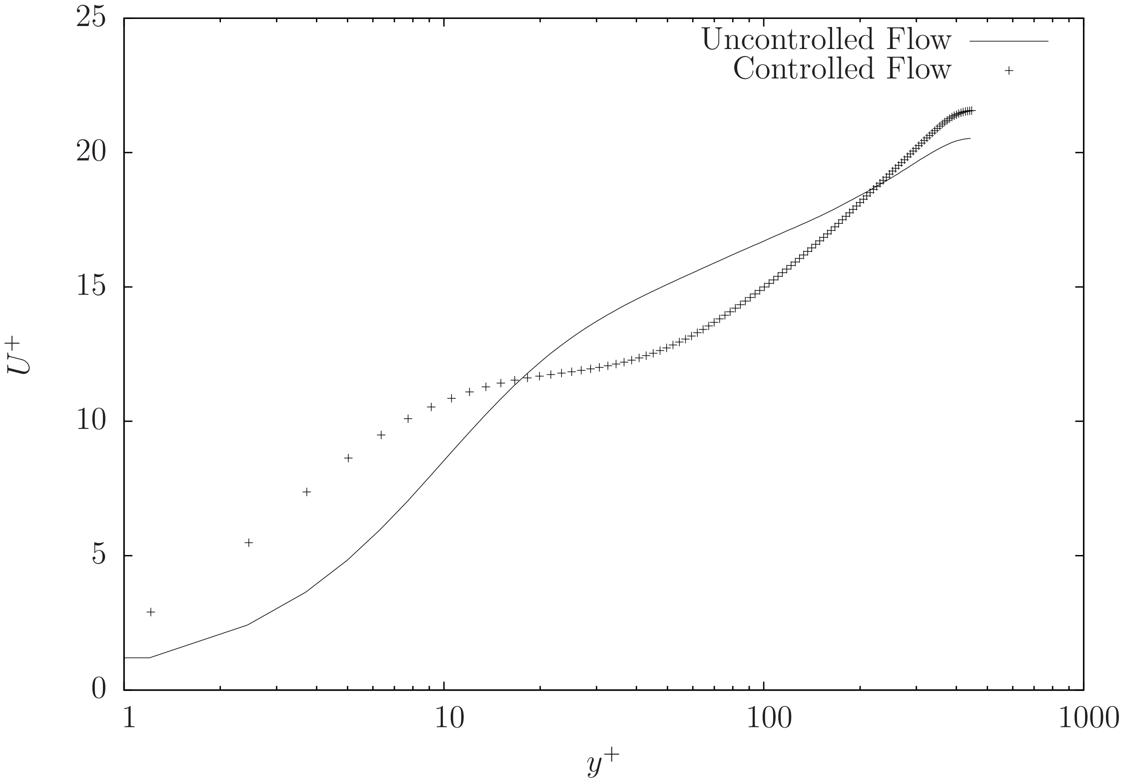

Figure 5.13: Mean velocity profile of the turbulent channel flow that undergoes spanwise traveling wave generated by DBD plasma actuators. The quantities are non-dimensionalized by the canonical $u_{\tau,0}$.

reducing cases are chosen and the simulations with traveling waves generated by the DBD plasma actuator model will be performed. The simulations are performed under exactly the same condition as in the study of SpTW_bf except that the forcing of ideal sinusoidal traveling wave is replaced by the DBD plasma actuators model and the traveling waves in each case are generated by 5 different actuator densities for comparison.

The first case examined is with frequency $\omega = 2$, wave number $\kappa_z = 1.96$ (one wave length in the spanwise direction) and wave amplitude $A_f = 15$. Fig. 5.14 shows the time history of the drag coefficient C_f of the DBD plasma actuator generated traveling waves with 5 different actuator densities. Along spanwise direction, the waves are generated by 4, 8, 16, 32 and 64 actuators, respectively. At any instant, only two actuators that are $\lambda/2$ away from each other will be activated in different directions. It is clear that the drag diminishes as the actuator density increases and only in the 64 phases (64 actuators) case the drag is slightly below that of the uncontrolled case.

Fig. 5.15 visualizes the near wall streamwise velocity on the wall-parallel $(x - z)$ plane at wall distance $y^+ = 4$ (scaled by $u_{\tau,0}$) for the 16 actuator case. The flow field exhibits regular distributed elongated streaks, which are the 'footprint' of the activation of the DBD plasma actuators. One could see instead of weakening the streaky structures as the ideal traveling wave does, the discretized wave further generates drag inducing structures, which would explain the escalated turbulence drag.

The second case studied correspond to the special case of traveling wave, i.e. the spanwise oscillatory forcing case with frequency $\omega = 1$, and wave amplitude $A_f = 5$. The time histories of the friction coefficient C_f are summarized in Fig. 5.16. In this case, as the number of actuator increases from 4 towards 64, the DBD plasma actuators will perform gradually more closely to the ideal sinusoidal wave. However, this is not what has been shown in the drag coefficient C_f where the performance deteriorates first as the number of actuators increases from 4 to 8 and 16 and then the performance improves with the number of actuators. This could be caused by the fact that in the 4 phase oscillatory forcing, the spanwise velocity created by the actuators is significantly less than that of the 8 phase case and 16 phase case. From Fig. 2.2 one can observe that once the wave is working at reducing the drag, larger forcing is normally associated larger R. However, when the wave works at increasing the drag, a larger forcing will even further increase the drag. As the number of actuators continue to increase, eventually they perform close to the ideal oscillatory forcing, where large R is reported. When the wave is generated by less than 64 DBD plasma actuators, the time history shows wild oscillations which is certainly caused by the extremely localized

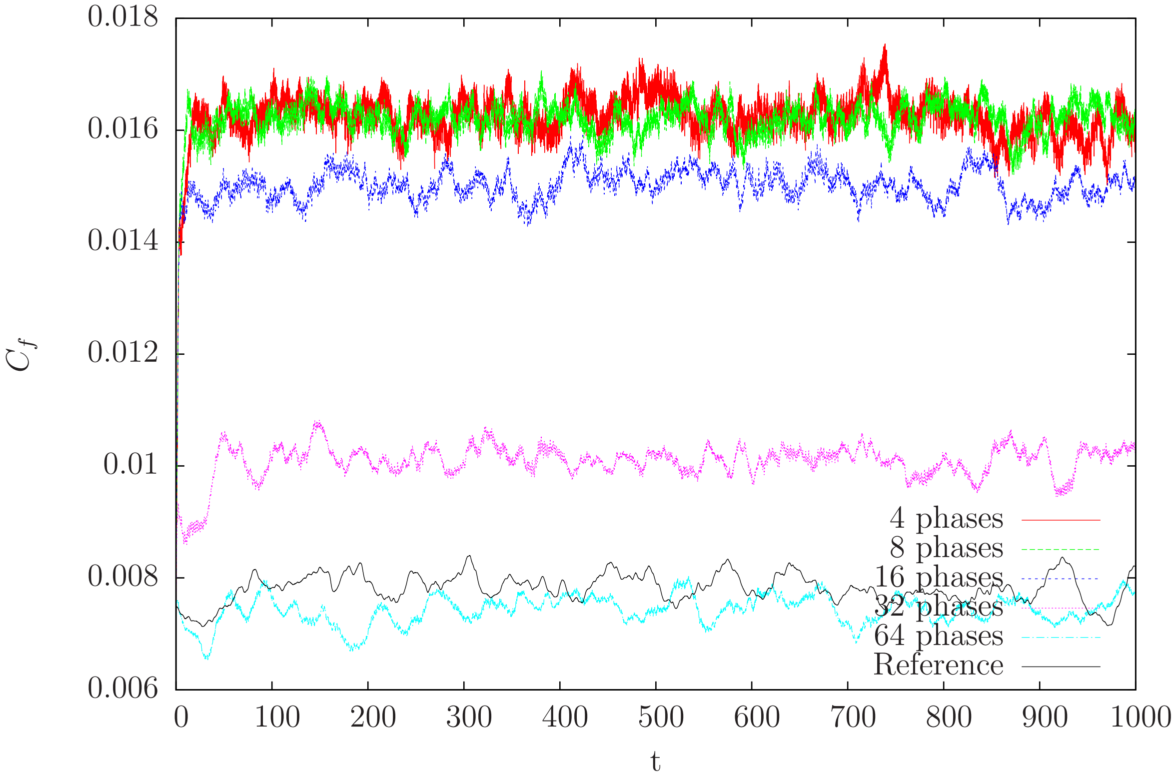

Figure 5.14: Time histories of drag coefficient C_f from the non-ideal traveling wave cases. All cases are with the same parameters $\omega = 2$, $\kappa_z = 1.96$ and $A_f = 15$.

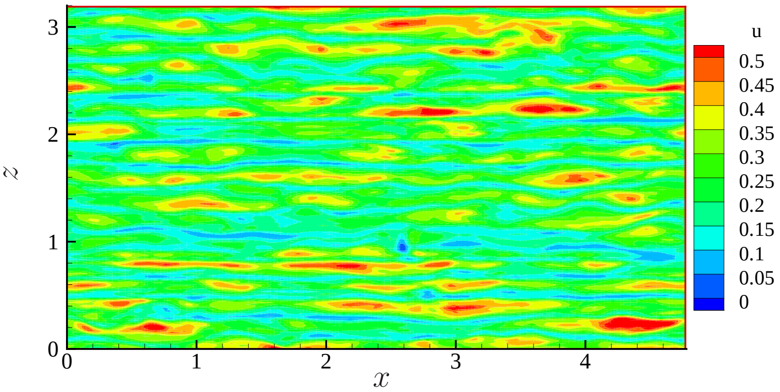

Figure 5.15: Contour of the streamwise velocity component u in a wall parallel cut of the computational domain at $y^+ = 4$ for the case with 16 DBD plasma actuators.

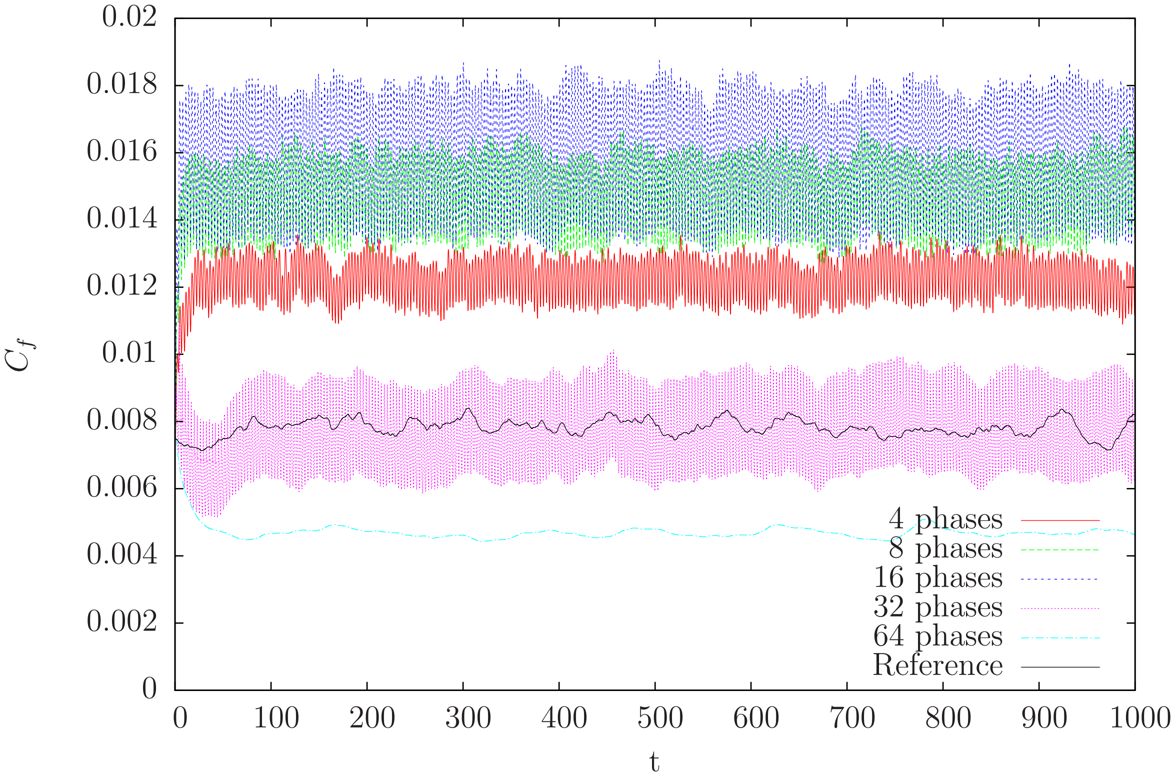

Figure 5.16: Time histories of drag coefficient C_f from the non-ideal spanwise oscillatory forcing.

effect, which only dies out when that effect deceases and the wave approaches the ideal sinusoidal SpTW_bf.

In spite that only two cases of DBD plasma actuator generated spanwise traveling wave are examined for drag reduction performances, we could already see that the continuous sinusoidal spanwise traveling wave is always preferred since the R value increases with the number of actuators in most of the simulations. In DNS, it is quite simple to increase the number of actuators along the spanwise direction. Nevertheless, experimentally that might become impossible because that means one has to almost put one actuator next to another with almost no space in between. For example, if we assume an actuator with width $b^+ = 10$ in wall unit, fitting 64 of them in the domain $L_z = 3.2$ or $L_z^+ = 640$ means that the space between the actuators is exactly 0. Therefore, obtaining drag reduction by DBD plasma actuators could be technically challenging.

Chapter 6

CPI

The traveling wave based turbulence drag reduction techniques are also suitable for the control problems in pipe flow. Choi and Graham [CG98] investigated in the drag reduction by circular-wall oscillation in turbulent pipe flow and 25% drag reduction was found. Quadrio and Sibilla [QS00] confirmed the drag reducing capacity of the oscillating wall technique in turbulent pipe flow and obtained drag reducing values similar to that associated with the oscillating wall control technique in channel flow, which is nearly 40%. Auteri et al. [ABB$^+$10] experimentally investigated in the traveling wave technique in turbulence pipe flow drag reduction and reported 33% drag reduction for slowly forward traveling waves. The work in this chapter for the first time employs the newly proposed CPI (Constant Power Input) concept to study the turbulence skin-friction problem in a pipe flow via StTW_w, which is the most efficient drag reduction method discussed in this dissertation.

6.1 Introduction of CPI

In previous chapters, the turbulence control performances of the streamwise and spanwise traveling waves were discussed. The assessment of the drag reduction is based on keeping Constant Flow Rate (CFR) in the streamwise direction and measuring the variation of the pumping power required to sustain the level of the given flow rate, and hence the friction drag. An alternative approach of maintaining a turbulent duct flow is to keep Constant Pressure Gradient (CPG) and the flow rate will adjust accordingly. In the case of CPG, the pressure gradient is prescribed and therefore so is the friction drag. The 'drag reduction' in CPG is embodied by the change in flow rate at a prescribed value of friction drag.

The power input into the system in a duct flow is given by the product

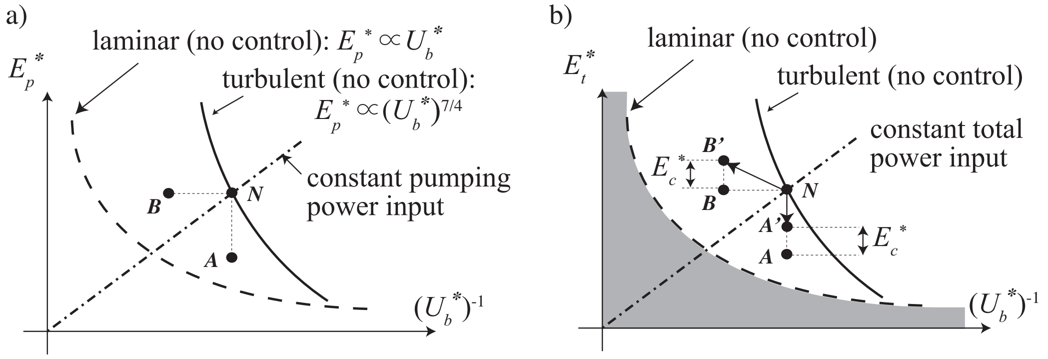

Figure 6.1: Pumping energy E_p^* (a), and total energy, $E_t^* = E_p^* + E_c^*$ (b), plotted versus the inverse of the dimensional bulk mean velocity, U_b^*, for fully developed turbulent flow (solid line) and laminar flow (dashed line). Taken from [HQF14]

of the pressure gradient and the flow rate. In the study of turbulent drag reduction, the mean energy flux is not constant in either CFR or CPG. CFR keeps the flow rate fixed and reduces the pressure gradient thus the energy flux decreases whereas CPG keeps pressure gradient fixed and increases the flow rate thus the energy flux increases. Both two scenarios cause difficulties to make any definite statement about the behaviour of dissipation because the sign of the global change of dissipation is prescribed by the simulation strategy [HQF14].

Almost all previous studies on turbulent drag reduction in channel or pipe flow are based on either the CFR ([JMA92, CMK94]) or the CPG (exemplified in [QR11]) condition, via either numerical simulations or experiments until very recent. Frohnapfel et al. [FHQ12] constructed a novel framework by imposing constant power input (CPI) condition instead of the conventional CFR or CPG. The CFR approach keeps the flow rate constant, the value of which is denoted as *convenience* in their work. In the CPG approach, the constant pressure gradient has a direct relationship with the energy consumption, denoted as *money* required to achieve certain convenience. The optimal flow control should maximize the convenience while minimize the energy consumption. The CPI framework assesses the flow control techniques by considering the two factors, i.e. energy consumption and convenience simultaneously and explicitly. They also proposed the money-versus-time plane in [FHQ12], a graphical tool for the assessment of flow control techniques for skin-friction drag reduction in the paper as shown in Fig. 6.1, which is taken from [HQF14], a newer paper recently published by the same authors.

The money-versus-time plane is obtained by following two steps. First one plots the pumping energy versus the inverse of the bulk velocity. When a drag reducing flow control is applied to the flow, the uncontrolled fully turbulent flow originally at point N shifts to point A under the CFR condition or to point B under the CPG condition. All the points on the straight line connecting the origin and point N have the same power input as at point N, thus a control under CPI condition will move along this straight line towards the origin into a third, different final state. Next, change the ordinate from the pumping energy to the sum of pumping and control energy, in order to account for the energetic cost of active flow control techniques. On the money-versus-time plane, both point A under CFR and point B under CPG will shift upwards by the control energy supplied into the system E_c^*. And now, the points on the straight line connecting the origin and point N have the same total power input.

As reasoned in [HQF14], the constant pumping power input (CpPI) and constant total power input (CtPI) are distinguished in the following sections. The CpPI approach is considered as a more practical alternative of simulation strategy which describes how a pump works. On the other hand, the CtPI is more suitable tool for the evaluation of active flow control techniques.

6.1.1 CtPI for flow control

The CtPI framework requires the total power input P_t^* into the flow system to be a constant. If no flow control is applied, all of P_t^* is used as the pumping power in the flow, therefore $P_p^* = P_t^*$, where P_p^* is the pumping power. If the flow is controlled by external forcing, P_c^* will be supplied to enforce the flow control and the pumping power becomes $P_p^* = P_t^* - P_c^*$.

If we express the power consumed by the flow control P_c^* as a fraction of the total power P_t^* as $P_c^* = \gamma P_t^*$, the pumping power is therefore $P_p^* = (1-\gamma)P_t^*$. By adjusting the parameter γ, one may control how much of the total energy is to be supplied to enforce the flow control and how much is to be used to pump the flow. In order to compare the effect of different choices of the parameter γ, one could simply compare the maximum flow rate could be achieved for a certain value of γ (Fig. 6.7). The result of CPI directly offers the optimal choice of control settings by choosing the γ that gives the largest flow rate [HQF14].

6.2 Canonical turbulent pipe flow under CpPI

As discussed before, the power input into the system in a pipe flow is given by the product of the pressure gradient and the flow rate. The exact mathematical relation between these three quantities needed to satisfy CpPI condition is derived in this section.

According to the streamwise force balance, the time averaged pressure gradient $-\dfrac{\mathrm{d}p^*}{\mathrm{d}x^*}$ and the wall shear stress τ_w^* are related as:

$$-\frac{\mathrm{d}p^*}{\mathrm{d}x^*}A^* = \tau_w^* C^*, \tag{6.1}$$

in which, A^* is the duct cross-sectional area and C^* is the wetted perimeter. For a cylindrical pipe flow, the wall shear stress τ_w^* is expressed as:

$$\tau_w^* = \frac{R^*}{2}\left(-\frac{\mathrm{d}p^*}{\mathrm{d}x^*}\right) \tag{6.2}$$

P_p^* denotes the pumping power per unit wetted area, therefore:

$$P_p^* = -\frac{\mathrm{d}p^*}{\mathrm{d}x^*}\frac{A^*}{C^*}U_b^* \tag{6.3}$$

in which, A^* and C^* are the area and perimeter of the channel cross-section and for a cylindrical pipe: $A^* = \pi R^{*2}$ and $C^* = 2\pi R^*$. U_b^* is the bulk velocity, i.e. the volume-averaged streamwise velocity. For a pipe flow, the pumping power is simplified as:

$$P_p^* = -\frac{R^*}{2}U_b^*\frac{\mathrm{d}p^*}{\mathrm{d}x^*} \tag{6.4}$$

The bulk velocity for a laminar flow in a pipe can be calculated by integrating in the wall-normal direction the expression of the parabolic velocity profile:

$$u^*(r^*) = \frac{1}{4\mu^*}\left(-\frac{\mathrm{d}p^*}{\mathrm{d}x^*}\right)(R^{*2} - r^{*2}). \tag{6.5}$$

We denote this particular value of the bulk velocity with U_Π^* (the subscript Π stands for power units):

$$U_\Pi^* = \frac{1}{\pi R^{*2}}\int_0^{R^*} u^*(r^*)2\pi r^*\mathrm{d}r^* = \frac{R^{*2}}{8\mu^*}\left(-\frac{\mathrm{d}p^*}{\mathrm{d}x^*}\right). \tag{6.6}$$

In a fully developed flow, the pumping power should balance the dissipation rate. The dissipation rate per unit volume ε^* is written as:

$$\varepsilon^* = \mu^*\left(\frac{\mathrm{d}u^*}{\mathrm{d}r^*}\right)^2. \tag{6.7}$$

If one takes a control volume in the pipe of length $\mathrm{d}L^*$, the total dissipation rate in the control volume is then:

$$\epsilon^* = \int_{V^*} \varepsilon^* \mathrm{d}V^* = \int_0^{\mathrm{d}L^*} \int_0^{R^*} \varepsilon^* 2\pi r^* \mathrm{d}r^* = 2\pi\mu^* \mathrm{d}L^* \int_0^{R^*} \left(\frac{\mathrm{d}u^*}{\mathrm{d}r^*}\right)^2 r^* \mathrm{d}r^* \tag{6.8}$$

In parabolic velocity profile, the wall normal derivative of the axial velocity is:

$$\frac{\mathrm{d}u^*}{\mathrm{d}r^*} = \frac{r^*}{2\mu^*}\frac{\mathrm{d}p^*}{\mathrm{d}x^*} = -\frac{4r^*}{{R^*}^2}U^*_\Pi. \tag{6.9}$$

By substituting the Eq. 6.9 into Eq. 6.8, we have:

$$\epsilon^* = 2\pi\mu^* \mathrm{d}L^* \int_0^{R^*} \left(-\frac{4r^*}{{R^*}^2}U^*_\Pi\right)^2 r^* \mathrm{d}r^* = 8\pi\mu^* \mathrm{d}L^* {U_\Pi}^2. \tag{6.10}$$

In fully developed turbulent pipe flow, the total dissipation per unit wetted area should balance the pumping power per unit wetted area, thus the following equation holds:

$$P^*_p = \frac{\epsilon^*}{2\pi R^* \mathrm{d}L^*}, \tag{6.11}$$

from which it is not difficult to obtain that the pressure gradient could be written in the form:

$$-\frac{\mathrm{d}p^*}{\mathrm{d}x^*} = \frac{8{U^*_\Pi}^2 \mu^*}{{R^*}^2 U^*_b}. \tag{6.12}$$

The Eq. 6.12 can be non-dimensionalized by:

$$-\frac{\mathrm{d}p}{\mathrm{d}x} = -\frac{\mathrm{d}(p^*/(\rho^* {U^*_p}^2))}{\mathrm{d}(x^*/R^*)} = \frac{8\mu^*}{\rho^* U^*_b R^*}, \tag{6.13}$$

in which, the reference velocity scale is the bulk velocity in power unit U^*_Π and the reference length scale is the radius of the cylindrical pipe R^*.

We define the Reynolds number based on the bulk velocity in power unit U^*_Π and the non-dimensional pressure gradient is related with non-dimensionalized bulk velocity U_b:

$$-\frac{\mathrm{d}p}{\mathrm{d}x} = \frac{8\mu^*}{\rho^* U^*_\Pi R^*}\frac{U^*_\Pi}{U^*_b} = \frac{8}{Re_\Pi U_b}. \tag{6.14}$$

It is easy to verify that the non-dimensional pumping power which is proportional to the product of the pressure gradient and the bulk velocity U_b is constant and this is a necessary condition for the CPI control:

$$P_p = \frac{P^*_p}{\rho^* {U^*_\Pi}^3} = \frac{4}{Re_\Pi}. \tag{6.15}$$

Therefore, under the CpPI framework, there exists a one-to-one relation between the pumping power P_p and the Reynolds number in power unit Re_Π. If one would like to make the turbulent pipe flow under constant pumping power, Eq. (6.14) has to be satisfied. In other words, the pressure gradient has to be adjusted for variations in the bulk velocity according to the nominal pumping power, which depicts how a pump works in reality.

6.2.1 CpPI in DNS

The implementation of the CpPI concept in the DNS simulation is not straight forward. It is not easy to guarantee the validity of the relationship between the pressure gradient and mean flow rate (Eq. 6.14) in the code, because at each time step, the mean flow rate is calculated a-posteriori. Nevertheless, when the time-discretization is fine and the computational time step is much smaller than the time scale of variation of both U_b and $\dfrac{\mathrm{d}p}{\mathrm{d}x}$, we can employ the bulk velocity at time step n to determine the pressure gradient at time step $n+1$:

$$\left(-\frac{\mathrm{d}p}{\mathrm{d}x}\right)^{(n+1)} = \frac{8}{Re_\Pi U_b^{(n)}}, \tag{6.16}$$

from which, we can advance to the solution by one step to compute $U_b^{(n+1)}$, the bulk velocity at time step $n+1$.

CpPI simulation of canonical turbulent pipe flow

A DNS simulation is carried out to simulate the uncontrolled turbulent pipe flow under the CpPI strategy. The Navier-Stokes equations in cylindrical coordinate system written in terms of radial velocity and radial vorticity enables employing the numerical techniques already developed for the Cartesian geometry [LQ06], which are used in the channel flow DNS in previous chapters. The number of Fourier modes in the azimuthal direction θ varies with the radial position r, by such a parsimonious approach, the problems of the computing resources and numerical stability are solved. A sketch of the cylindrical coordinate system used in this study is shown in Fig. 6.2.

The size of the pipe is set to $L_x = 20$, which is the length of the pipe and $R = 1$ which is the radius of the cross section, note that these quantities are non-dimensionalized by the radius of the pipe cross section R^*. The Reynolds number based on total power input is $Re_\Pi = 5352$, which gives the friction velocity based Reynolds number $Re_\tau \approx 200$. The number of Fourier modes in the streamwise, radial and azimuthal directions are $N_x = 384$, $N_r = 100$

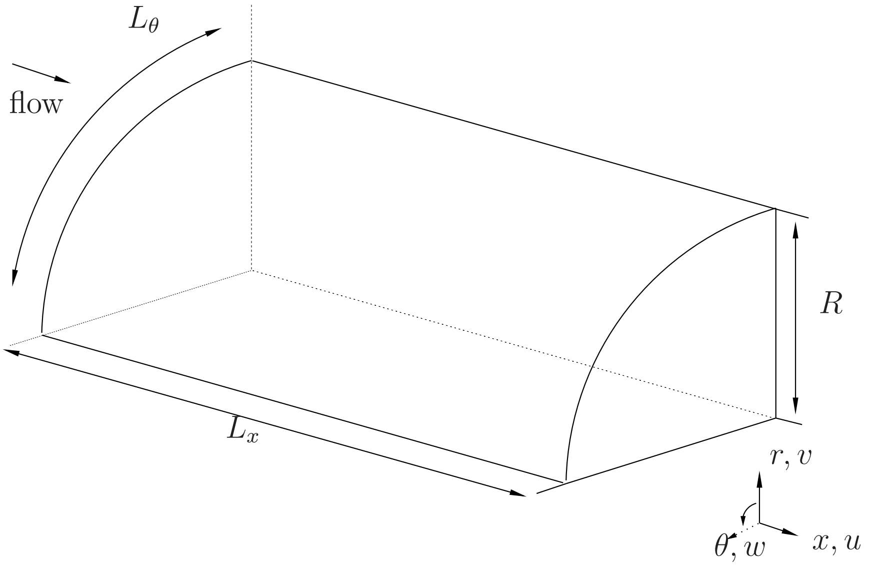

Figure 6.2: The sketch of cylindrical coordinate system in the pipe. x is the streamwise direction, θ is the azimuthal direction and r is the radial direction. The corresponding velocities are u, v and w, respectively.

and $N_\theta = 256$. The corresponding resolution in the streamwise direction is $\Delta x^+ = 10.4$, in the azimuthal direction $R\theta^+ \leq 4.9$ and in the radial direction varies from $\Delta r^+_{\text{min}} = 0.75$ at the wall to $\Delta r^+_{\text{max}} = 2.43$ at the centerline.

The time histories of the mean streamwise bulk velocity U_b and the mean pressure gradient $\left\langle \frac{\partial p}{\partial x} \right\rangle$ are plotted in Fig. 6.3. They are both normalized by their time averaged values. During the whole integration time, the product of the spatial mean bulk velocity and mean pressure gradient is kept constant, which is indicated by the solid horizontal line in the figure and therefore, so is the total power input.

The DNS simulation was performed at $Re_\Pi = 5352$, which roughly correspond to $Re_b = 2950$ (based on bulk velocity U_b) or $Re_\tau = 200$. Therefore, the current turbulent pipe flow under CPI condition should behave identical to the turbulent pipe flow under CFR condition at $Re_b = 2950$, or under CPG condition at $Re_\tau = 200$. Fig. 6.4 and Fig. 6.5 demonstrate the mean streamwise velocity profiles U^+ and the profile of the turbulence fluctuation component u_{rms} of the CPI, CFR and CPG simulations which are carried out at the same Reynolds number. The three curves in both figures collapse with each other quite well, which suggests the validity and correctness of the simulation under CPI condition. Moreover, both Fig. 6.4 and 6.5 agree very well with the previous works, e.g. [WM08, EUW+94] in spite of the fact that

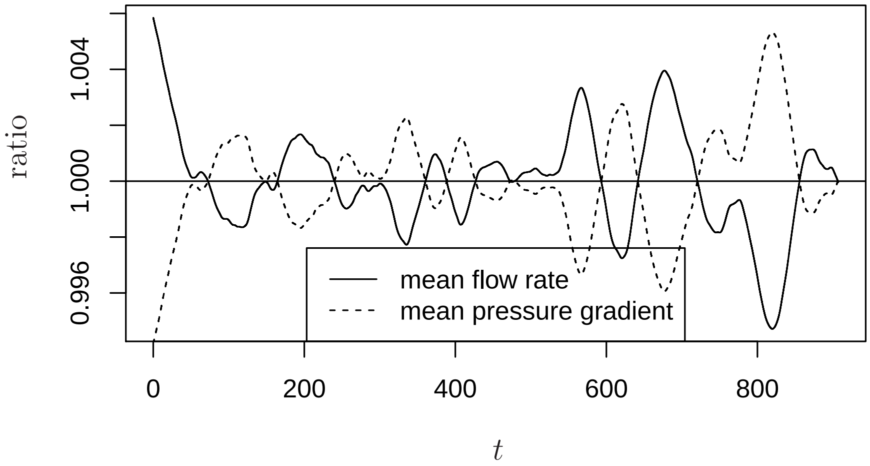

Figure 6.3: Time history of the normalized spatial mean streamwise bulk velocity (continuous curve) and the normalized spatial mean streamwise pressure gradient (dashed curve). The horizontal solid line is the product of the two quantities, which is actually remained constant.

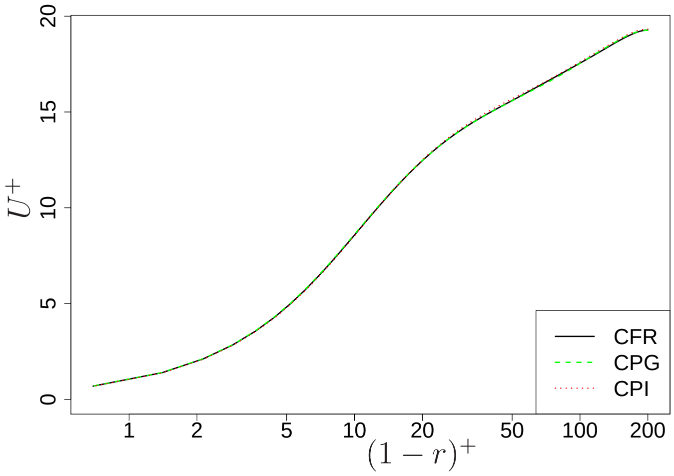

Figure 6.4: The mean velocity profiles for CPI, CFR and CPG simulations which correspond to the same Reynolds number.

they used a slightly smaller Reynolds number $Re_b = 2650$.

6.3 Controlled turbulent pipe flow under CPI

As accentuated along the establishment of the dissertation, it is crucial to take the power required by the flow control into consideration for the evaluation of a particular flow control method. This idea could naturally fits in the CPI concept by keeping the total power input a constant. When we would like to have the flow controlled, a certain amount of power $P_c^* = \gamma P_t^*$ will have to be taken away from the total power available P_t^*, which is a constant under the CPI concept by design. Due to this constraint, the power for pumping the fluid is lessened $P_p^* = P_t^* - P_c^* = (1-\gamma)P_t^*$. In order to assess the flow control technique, it is necessary only to measure the change in the streamwise mean velocity. As long as the ratio between the mean velocity in the controlled flow and that of the uncontrolled flow is greater than one, the flow control technique contributes positively to the drag reducing performance.

In the case where total power is kept constant, some of the equations derived for CpPI are not valid until slight modifications are applied. Since the total power is no longer the same as the pumping power, it is very important to be aware that the power unit should be based on the total power but not the pumping power. The highest bulk velocity achievable U_Π^*

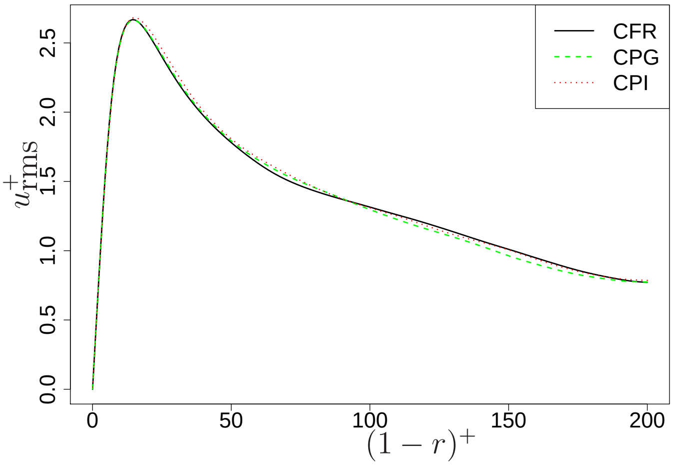

Figure 6.5: The profiles of the root mean square of the streamwise turbulence fluctuation velocity u'^{+} for CPI, CFR and CPG simulations which correspond to the same Reynolds number.

in this scenario only happens when the pipe flow is laminar and all the power available (P_t^*) is served as the pumping power to the flow. U_Π^* is termed as the velocity in power unit and could be expressed as:

$$U_\Pi^* = \sqrt{\frac{R^* P_t^*}{4\mu^*}} \tag{6.17}$$

After proper non-dimensionalization, the dimension-less expression for the total power could be written as:

$$P_t = \frac{4}{Re_\Pi}, \tag{6.18}$$

and by subsequently, it is easy to obtain the expressions for the dimensionless pumping power and control power:

$$P_p = \frac{4(1-\gamma)}{Re_\Pi} \tag{6.19}$$

$$P_c = \frac{4\gamma}{Re_\Pi} \tag{6.20}$$

In order to keep the total power input as a constant in the DNS simulation, both Eq. (6.19) and (6.20) have to be guaranteed. The Eq. (6.19) is ensured by adjusting the pressure gradient according to the bulk velocity at each time step:

$$\left(-\frac{\mathrm{d}p}{\mathrm{d}x}\right)^{(n+1)} = \frac{8(1-\gamma)}{Re_{\Pi}U_b^{(n)}}, \tag{6.21}$$

while Eq. (6.20) is kept validated by adapting the ratio γ according to the ratio control power (from the previous step) to the total power $P_t = \frac{4}{Re_{\Pi}}$:

$$\gamma^{(n+1)} = \frac{P_c^{(n)}}{\frac{4}{Re_{\Pi}}} \tag{6.22}$$

6.3.1 Drag reduction by StTW_w

One of the most important conclusions in the dissertation is that among the four types of traveling waves discussed, the StTW_w is the most favorable because of its large drag reducing and net energy saving capacities and relatively simple experimental implementation. Naturally, StTW_w is the most interesting flow control method to investigate under the CPI concept.

The turbulence skin-friction drag reduction of turbulent pipe flow by StTW_w under the CFR concept has been studied by M. Biggi [Big12]. In her work, it is reported that the maximum drag reduction value R could reach 0.7 at $Re_\tau = 200$. Fig. 6.6 illustrates the R value versus the wave frequency ω at fixed value of wavenumber $\kappa_x = 0.9425$, $A^+ = 12$ and $Re_\tau = 200$. The red curve represents the cylindrical pipe flow while the dark blue curve represents the channel flow. In a big range of different ω, the drag reducing performance of the streamwise traveling wave is similar in the pipe and the channel flow. However, when ω is of a very small positive value (≈ 0.1), the drag reducing performance in the pipe significantly outnumbers that of the channel flow and the maximum $R = 0.7$ indicates that the pipe flow is relaminarized.

Our aim in this study is to be able to present a plot similar to Fig. 6.7, which is taken directly from [HQF14], on which the maximum achievable ratio between the flow rate of controlled flow and that of the uncontrolled flow $\frac{U_b}{U_{b,0}}$ is plotted against the choice of the energy split parameter γ. The underlying problem studied in [HQF14] was the turbulence drag reduction by wall oscillation in channel geometry. And based on the figure to be obtained, the optimal choice of γ will be directly available so that one may make an optimal decision how the total power should be allocated to pumping and control.

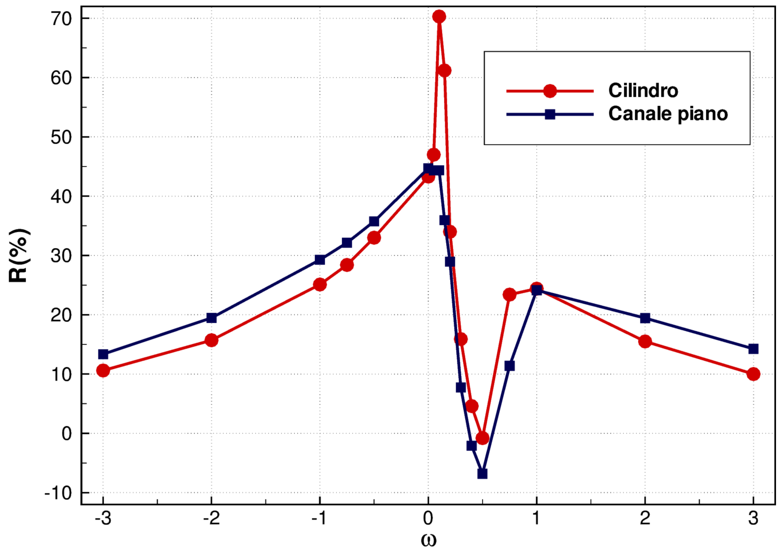

Figure 6.6: The turbulence skin-friction drag reduction $R(\%)$ versus the wave frequency ω at $Re_\tau = 200$. $\kappa_x = 0.9425$, $A^+ = 12$. The red curve represents the cylindrical pipe flow while the dark blue curve represents the channel flow. (Taken from [Big12])

As argued before, it is not straightforward to calculate the maximum achievable $\frac{U_b}{U_{b,0}}$ at a given energy split γ since the control power P_c and therefore γ are not prescribed in the simulation, but instead, they are a-posteriori quantities which are only computed after the simulation is performed. Thus the search for maximum $\frac{U_b}{U_{b,0}}$ is an iterative procedure. However, based on the information available in the previous mentioned thesis [Big12] and the parametric study of the StTW_w for channel flow under CFR [QRV09], the probable parameter combinations that gives the maximum (at least close to maximum) $\frac{U_b}{U_{b,0}}$ at given γ are already available.

The calculation of control power

The power required associated with the wall based traveling wave in a channel flow is given in Eq. (2.2). The control power required in the pipe flow could be derived with slight modifications:

$$P_{in,pipe} = \frac{L_x 2\pi R}{t_f - t_i} \int_{t_i}^{t_f} \tau_\theta \bigg|_{r=R} w\mathrm{d}t, \tag{6.23}$$

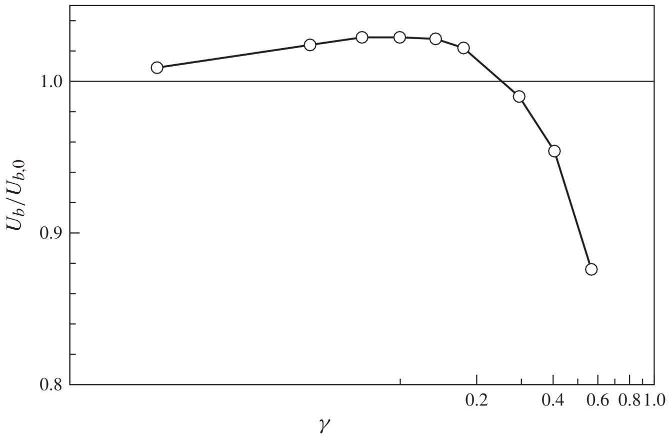

Figure 6.7: Variation of the flow rate over the flow rate of the uncontrolled flow, as a function of the share γ of the available power between pumping power and control power provided the oscillating walls. Taken from [HQF14].

in which, the spanwise length L_z in Eq. 2.2 has been replaced by the perimeter of the pipe's cross section $2\pi R$ and there exists only one wall instead of the upper and lower wall in the case of channel flow.

It is also worthwhile to clarify a detail in the calculation of the wall-shear stress τ_θ, which could be easily overlooked. Since we analyze the pipe flow in a cylindrical coordinate system, there exists an extra term in the expression of τ_θ which does not appear in the Cartesian coordinate system:

$$\tau_\theta\bigg|_{r=R} = \frac{\partial w}{\partial r}\bigg|_{r=R} - w\bigg|_{r=R}. \tag{6.24}$$

Results

Based on previous experience on the StTW_w control of the turbulent pipe flow and channel flow, the big picture of the performance of the StTW_w on drag reduction exists. It is suggested that for different values of wave amplitude A, the largest R is always found near a certain value of wave frequency ω and wave number κ_x. Therefore, the searching for the optimal parameters at a given γ becomes simpler. Once the optimal ω and κ_z are found, these values should be unchanged and there exists a one-to-one relationship between the wave amplitude A and the parameter γ. By this means, the 3-D optimization problem becomes 1-D and traversing different values of A enables the exploration for optimum γ.

Fig. 6.6 features a relaminarization occurs under condition $\kappa_x = 0.9452$,

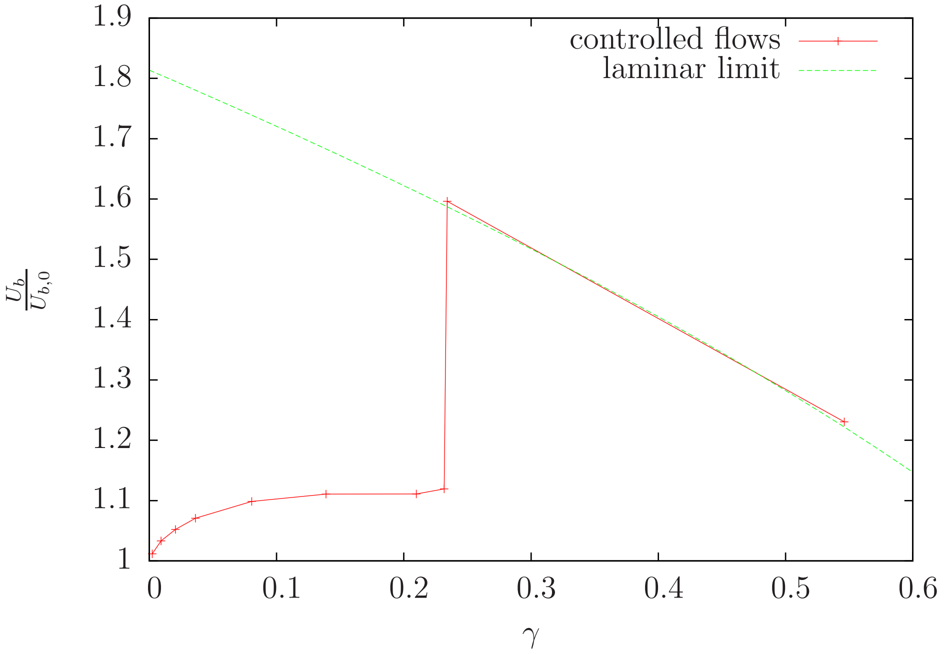

Figure 6.8: The ratio between flow rates of the controlled flows (under CPI) and the uncontrolled flow as a function of γ in turbulent pipe flow at canonical $Re_\tau = 200$. The laminar limit curve is shown for reference.

$A^+ = 12$ and $\omega = 0.11$ at $Re_\tau = 200$. That is already the largest Reynolds number under which relaminarization has ever been occurring to the author's knowledge. It is reasonable to regard the combination $\kappa_z = 0.9452$ and $\omega = 0.11$ as the optimal choice, and the next step only requires a number of DNS cases with different wave amplitude A. The final curve of $\dfrac{U_b}{U_{b,0}}$ obtained as a function of γ is presented in Fig. 6.8. The symbols on the curve represent the simulations carried out.

The most prominent feature one may notice in Fig. 6.8 is that at around $\gamma = 0.23$, the ratio between the flow rates suddenly peaks at a value near 1.6, and falls down as γ further increases. It is strongly suspected that that sudden increase is a result of relaminarization. In order to verify the conjecture, one will have to calculate the laminar limit of the flow rate, which is given γP_t^* as the pumping power to a laminar pipe flow, the flow rate eventually achieved over the flow rate of a fully turbulent pipe flow pumped with power P_t^* [HQF14].

The Prantl's friction law for smooth pipe [Pop00] suggests:

$$\frac{1}{\sqrt{f}} = 2.0\log_{10}(\sqrt{f}Re_b) - 0.8, \tag{6.25}$$

in which, f is called friction factor that satisfies $f = 4C_f$ and the Reynolds number used in Eq. (6.25) is based on bulk velocity.

The pumping power P_p^* in a fully developed turbulent pipe flow could be written in the form:

$$P_t^* = P_p^* = \tau_w^* U_b^* = \frac{1}{2}\rho^* U_b^{*3} C_f. \tag{6.26}$$

Once the SpTW_w is activated, a part of the total power P_t^* in Eq. (6.26) is spent on generate the traveling wave and the rest is left to continue pumping the fluid. Therefore, in controlled flow, the pumping power satisfies:

$$P_p = \frac{4}{Re_\Pi} = \frac{\frac{1}{2}\rho^* U_b^{*3} C_f}{\rho^* U_\Pi^{*3}}(1-\gamma) = \frac{1}{2}\left(\frac{Re_b}{Re_\Pi}\right) C_f(1-\gamma), \tag{6.27}$$

where the term $1-\gamma$ on the right hand side of the equation accounts for deduction of the power spent on enforcing the flow control, Re_Π stands for the Reynolds number in pumping power unit.

After several steps of simple operations, the Re_Π and Re_b are related by:

$$Re_\Pi = \frac{1}{2\sqrt{2}} Re_b^{3/2} \sqrt{C_f(1-\gamma)}. \tag{6.28}$$

With the assistance of Eq. (6.25), it is possible to derive the ratio between the flow rate of the laminar pipe flow and that of the fully developed turbulent pipe flow, both with the same pumping power:

$$\frac{U_\Pi}{U_b} = \frac{Re_\Pi}{Re_b} = \frac{1}{2\sqrt{2}}\sqrt{Re_b C_f(1-\gamma)}. \tag{6.29}$$

Under condition $Re_b = 2950$ (correspond to $Re_\tau = 200$) and $\gamma = 0.23$, it is possible to obtain the laminar limit:

$$\frac{U_\Pi}{U_b} = 1.59, \tag{6.30}$$

which corresponds exactly to the maximum $\dfrac{U_b}{U_{b,0}}$ found in Fig. 6.8. Therefore, it is confirmed that the SpTW_w is capable of relaminarize the turbulent pipe flow at $Re_\tau = 200$ under the CPI framework. The laminar limit over a larger range of γ from 0 to 0.6 is plotted in Fig. 6.8.

If γ continue to increase, more power is allocated for the flow control while less is left for pumping the fluid and the flow rate will decrease due to the decline of pumping power P_p^*. In the extreme case where $\gamma = 1$, i.e. no pumping power, the flow will eventually completely stop. In this whole process, the flow stays in the laminar state.

Chapter 7

Conclusion and future work

7.1 Conclusion

This dissertation addresses the turbulence skin-friction drag reduction problem by traveling wave approaches. The traveling wave approaches are distinguished according to the waves' traveling direction (streamwise/spanwise) and forcing type (wall velocity/body force). The StTW_w has been assessed thoroughly by parametric study in [QRV09]. Global maps for drag reduction and net energy saving in the parameter space were obtained, which are still missing in the study of the other three members in the traveling wave family. Du & Karniadakis [DK00] and Du et al. [DSK02] were the first to show the drag-reduction capabilities of SpTW_bf, reporting a maximum reduction of turbulent skin-friction drag of about 30%, with a significantly altered structure of the near-wall turbulence. Zhao et al. [ZWL04] studied a similar wave based on wall velocity, which is referred as SpTW_w in this dissertation. They concluded that qualitatively, the wall based SpTW_w and body force based SpTW_bf are comparable. However, both [DSK02] (10 simulations) and [ZWL04] (only 2 simulations) do not provide a conclusive evaluation for either SpTW_bf or SpTW_w. Apart from the limited number of simulations performed, the energetic performance is completely left out from the scope of their works, which nowadays is realized to be a crucial factor in flow control applications. The other type of traveling wave, namely the SpTW_bf, has not yet been discussed by any author before.

This dissertation retrospects SpTW_w, SpTW_bf and starts the assessment on StTW_bf, based on extensive 3-D or 4-D parametric study. The similarities between SpTW_w and SpTW_bf are confirmed by the comparable drag reducing, net saving performances and the near-wall structure modifications. Nevertheless, since SpTW_bf is based on body force, there is one more wave parameter to tune, which is known as the penetration length Δ depicting how deep the body force is affecting in the bulk flow. The maximum drag reduction R values obtained for SpTW_w and SpTW_bf controlled flows are 38% and 47%, respectively. It is found that the larger R in body force based case benefits from that extra degree of freedom on Δ. However, the net savings are 10% and 12%, respectively, the difference of which is marginal. This indicates the energy for flow control is price has to be paid for that extra degree of freedom. On the other hand, the study of StTW_bf does not reveal its advantage over the wall based StTW_w in both drag reduction R and net saving S. Nevertheless, the 3-D map of drag reduction suggests that while the force amplitude A and penetration length Δ become large, the 'ridge' of large R gradually moves towards low frequency region and the global maximum R is found at $\omega = -0.1$, i.e. the wave travels upstream. The most surprising result learned from the study is that in both SpTW_w and SpTW_bf, the global maximum drag reduction and net energy saving always occur under condition $\kappa_z = 0$ which is a special case of the traveling wave: spanwise oscillatory forcing. The fact that spanwise wall oscillation is nowadays considered a rather inefficient flow control technique from an energetic viewpoint implies that also the spanwise traveling wave should be considered as such.

An interesting outcome of the present study, that to the author's knowledge was not previously reported, is the finding that spanwise traveling wave produce a spanwise net mass flux in the spanwise direction, although the pressure gradient in that direction is zero. The spanwise flow takes place in the opposite direction compared to the direction of the traveling wave, and this is consistent with the interpretation that, owing to the modifications induced at the wall by the wall forcing through the continuity equation, a wall normal blowing/suction wave is created that travels along the spanwise direction. Such wave is known [HF09] to induce a mass flux whose direction is opposite to its traveling direction. Both SpTW_w and SpTW_bf are found producing a spanwise net mass flux even when they are stationary in space (phase velocity equal to zero), although the direction in this case exhibits stochastic characteristics. This behaviour is linked to the asymmetry in the initial flow field employed for the numerical simulations; the symmetry (which in this case requires no net mass flux at all) is re-established after proper ensemble averaging over different initial conditions.

Experimentally, the DBD plasma actuators have been used in turbulence control, which are potential candidates for traveling wave control. The DBD plasma actuator creates extremely local effect in the flow and in order to generate a drag reducing traveling wave, one will have to increase the number of

DBD plasma actuators along the direction of the traveling wave. However, the increasing number of actuators could be both technically and economically impractical in real experimental applications. Du et al. [DSK02] has reported that by increasing the wave frequency, the non-ideal sinusoidal traveling wave may regain the drag reducing capability as the slowly traveling ideal wave. However, their work is based on a experimental Lorentz force model, where the body force ”bump” is of the order of several hundreds wall units width. However, the ”bumps” in the body force profile in the DBD plasma actuator model are only of the order of 10 wall units width. The extreme localization of the DBD plasma actuator model makes it impossible to simply recover the drag reducing capability by simply increasing the wave frequency since the gap between the ”bumps” is too large.

A recently proposed [FHQ12] new framework for flow control, named CPI, is applied to a turbulent pipe flow skin-friction reduction problem by StTW_w, which is considered as the most efficient control method in the methods discussed in this dissertation. The CPI concept offers the optimal management of the power budget available by finding the optimal share of power between the pump and the flow control device that provides the largest flow rate [HQF14]. It is found that when 23% of the total power available is allocated to implement the StTW_w control, a 59% flow rate increase is secured under the optimal parameter choice. The laminar limit calculation suggests that the turbulent pipe flow is already relaminarized, which confirms the relaminarization capability of StTW_w. Under $Re_\tau = 200$, StTW_w is currently the only flow control technique that is able to relaminarize the turbulent flow.

7.2 Future work

In spite of the low efficiency associated with the spanwise traveling wave concluded, the drag reducing mechanism is not fully understood yet. From the near-wall flow visualization, it is observed that the streaks are eliminated in the drag reducing flow and low speed ’ribbons’ are formed. Fig. 2.7 suggests the ’ribbon’ is generated by lifting up the low speed fluid by the traveling wave. It is conjectured that the favored phase velocity of the wave will keep the low speed fluid being lifted up and move it with the wave. If such mechanism is at work, the drag reduction should scale with the wave parameters. One possible future work is to understand deeper the mechanism of the formation of the ’ribbon’ and discover its quantitative relationship with the drag reduction. The unexpected spanwise flow rate was explained by the ’streaming’ effect. This byproduct in the current flow control approach is completely wasted. It would be quite interesting to see if the 'streaming' effect could be working together with the traveling wave control in the same direction to further increase the drag reduction.

It was shown that the turbulent pipe flow is successfully relaminarized by StTW_w, under both CPI and CFR conditions, at $Re_\tau = 200$. However, at such a Reynolds number, the turbulent channel flow will not experience relaminarization with the same control technique applied. The role played by the geometry becomes critical in understanding the different control effects in the pipe and channel flow. Seeking the root that prevents or promotes relaminarization in different geometries would be highly inspiring, yet highly challenging.

Bibliography

[ABB$^+$10] F. Auteri, A. Baron, M. Belan, G. Campanardi, and M. Quadrio. Experimental assessment of drag reduction by traveling waves in a turbulent pipe flow. *Phys. Fluids*, 22(11):115103/14, 2010.

[BE79] R.F. Blackwelder and H. Eckelmann. Streamwise vortices associated with the bursting phenomenon. *J. Fluid Mech.*, 94:577–594, 1979.

[Big12] M. Biggi. Riduzione di resistenza in flussi turbolenti di parete: confronto tra esperimenti e simulazione numerica diretta. Laurea Thesis, Politecnico di Milano, Dip. Ing. Aerospaziale, 2012.

[BQ96] A. Baron and M. Quadrio. Turbulent drag reduction by spanwise wall oscillations. *Appl. Sci. Res.*, 55:311–326, 1996.

[Can86] B. J. Cantwell. Viscous starting jets. *J. Fluid Mech.*, 173:159–189, 1986.

[CB05] S.I. Chernyshenko and M.F. Baig. The mechanism of streak formation in near-wall turbulence. *J. Fluid Mech.*, 544:99–131, 2005.

[CDAC13] A. Cimarelli, E. De Angelis, and C.M. Casciola. Paths of energy in turbulent channel flows. *J. Fluid Mech.*, 715:436–451, 2013.

[CEW10] T. C. Corke, C. L. Enloe, and S. P. Wilkinson. Dielectric barrier discharge plasma actuators for flow control. *Annu. Rev. Fluid Mech.*, 42:505–529, 2010.

[CG98] K-S. Choi and M. Graham. Drag reduction of turbulent pipe flows by circular-wall oscillation. *Phys. Fluids*, 10(1):7–9, 1998.

[Cho00] Kwing-So Choi. European drag-reduction research – recent developments and current status. *Fluid Dynamic Research*, 26:325–335, 2000.

[Cho02] K.-S. Choi. Near-wall structure of turbulent boundary layer with spanwise-wall oscillation. *Phys. Fluids*, 14(7):2530–2542, 2002.

[CJW11] K.-S. Choi, T. Jukes, and R. Whalley. Turbulent boundary-layer control with plasma actuators. *Phil. Trans. R. Soc. A*, 369(1940):1443–1458, 2011.

[CL01] K.-S. Choi and J.L. Lumley. The return to isotropy of homogeneous turbulence. *J. Fluid Mech.*, 436:59–84, 2001.

[CMK94] H. Choi, P. Moin, and J. Kim. Active turbulence control for drag reduction in wall-bounded flows. *J. Fluid Mech.*, 262:75–110, 1994.

[DCISO02] G.M. Di Cicca, G. Iuso, P.G. Spazzini, and M. Onorato. PIV investigation of turbulent boundary layer manipulated by spanwise wall oscillations. *J. Fluid Mech.*, 467:41–56, 2002.

[DK00] Y. Du and G. E. Karniadakis. Suppressing wall turbulence by means of a transverse traveling wave. *Science*, 288:1230–1234, 2000.

[DS99] M.R. Dhanak and C. Si. On reduction of turbulent wall friction through spanwise oscillations. *J. Fluid Mech.*, 383:175–195, 1999.

[DSK02] Y. Du, V. Symeonidis, and G. E. Karniadakis. Drag reduction in wall-bounded turbulence via a transverse travelling wave. *J. Fluid Mech.*, 457:1–34, 2002.

[Ela12] D. Elam. *A direct numerical simulation of dielectric barrier discharge (DBD) plasma actuators for turbulent skin-friction control.* PhD thesis, University of Warwick, 2012.

[EUW$^+$94] J.G.M. Eggels, F. Unger, M.H. Weiss, J. Westerweel, R.J. Adrian, R. Fiedrich, and F.T.M. Nieuwstadt. Fully developed turbulent pipe flow: a comparison between direct numerical simulation and experiment. *J. Fluid Mech.*, 268:175–209, 1994.

[FHQ12] B. Frohnapfel, Y. Hasegawa, and M. Quadrio. Money versus time: evaluation of flow control in terms of energy consumption and convenience. *J. Fluid Mech.*, 700:406–418, 2012.

[FIK02] K. Fukagata, K. Iwamoto, and N. Kasagi. Contribution of Reynolds stress distribution to the skin friction in wall-bounded flows. *Phys. Fluids*, 14(11):L73–L76, 2002.

[GeH00] M. Gad-el Hak. *Flow Control – Passive, Active and Reactive Flow Management*. Cambridge University Press, Cambridge, 2000.

[GMJ11] R. Garcia-Mayoral and J. Jiménez. Drag reduction by riblets. *Phil. Trans. R.Soc. A*, 369(1940):1412–1427, 2011.

[GQ13] D. Gatti and M. Quadrio. Performance losses of drag-reducing spanwise forcing at moderate values of the Reynolds number. *Phys. Fluids*, 25:125109(17), 2013.

[HF09] J. Hœpffner and K. Fukagata. Pumping or drag reduction? *J. Fluid Mech.*, 635:171–187, 2009.

[HQF14] Y. Hasegawa, M. Quadrio, and B. Frohnapfel. Numerical simulation of turbulent duct flows at constant power input. *J. Fluid Mech.*, 2014.

[ITYT06] M. Itoh, S. Tamano, K. Yokota, and S. Taniguchi. Drag reduction in a turbulent boundary layer on a flexible sheet undergoing a spanwise traveling wave motion. *J. Turbulence*, 7(27):1–17, 2006.

[JCJS06a] T. Jukes, K.-S. Choi, G. Johnson, and S. Scott. Turbulent drag reduction by surface plasma through spanwise flow oscillation. In *3rd AIAA Flow Control Conference*, 2006.

[JCJS06b] T. N. Jukes, K. S. Choi, G. A. Johnson, and S. J. Scott. Characterization of surface plasma-induced wall flows through velocity and temperature measurements. *AIAA Journal*, 44(4):764–771, 2006.

[JG77] J. L. Lumley and G. R. Newman. The return to isotropy of homogeneous turbulence. *J. Fluid Mech.*, 1977.

[JH95] J. Jeong and F. Hussain. On the identification of a vortex. *J. Fluid Mech.*, 285:69–94, 1995.

[Jim94] J. Jiménez. On the structure and control of near wall turbulence. *Physics of Fluids*, 6:944–953, 1994.

[JM91] J. Jiménez and P. Moin. The minimal flow unit in near-wall turbulence. *J. Fluid Mech.*, 225:213–240, 1991.

[JMA92] W.J. Jung, N. Mangiavacchi, and R. Akhavan. Suppression of turbulence in wall-bounded flows by high-frequency spanwise oscillations. *Phys. Fluids A*, 4 (8):1605–1607, 1992.

[JP99] J. Jiménez and A. Pinelli. The autonomous cycle of near-wall turbulence. *J. Fluid Mech.*, 389:335–359, 1999.

[KC03] G.E. Karniadakis and K.-S. Choi. Mechanisms on transverse motions in turbulent wall flows. *Ann. Rev. Fluid Mech.*, 35:45–62, 2003.

[KCM93] A.G. Kravchenko, H. Choi, and P. Moin. On the relation of near-wall streamwise vortices to wall skin-friction in turbulent boundary layers. *Phys. Fluids A*, 5(12):3307–3309, 1993.

[KHF09] N. Kasagi, Y. Hasegawa, and K. Fukagata. Towards cost-effective control of wall turbulence for skin-friction drag reduction. volume 132 of *Advances in Turbulence XII*, pages 189–200. Springer, 2009.

[KMM87] J. Kim, P. Moin, and R. Moser. Turbulence statistics in fully developed channel flow at low Reynolds number. *J. Fluid Mech.*, 177:133–166, 1987.

[KRSR67] S. J. Kline, W. C. Reynolds, F. A. Schraub, and P. W. Runstadler. The structure of turbulent boundary layers. *J. Fluid Mech.*, 30:741–773, 1967.

[KSF09] N. Kasagi, Y. Suzuki, and K. Fukagata. MEMS-based feedback control of turbulence for drag reduction. *Annu. Rev. Fluid Mech.*, 41:231–251, 2009.

[Lig63] M.J. Lighthill. *Laminar Boundary Layers*, page 99. Oxford: Clarendon Press, 1963.

[LQ06] P. Luchini and M. Quadrio. A low-cost parallel implementation of direct numerical simulation of wall turbulence. *J. Comp. Phys.*, 211(2):551–571, 2006.

[LSM94] F. Laadhari, L. Skandaji, and R. Morel. Turbulence reduction in a boundary layer by a local spanwise oscillating surface. *Phys. Fluids*, 6 (10):3218–3220, 1994.

[Mar09] F. Martinelli. *Feedback control of turbulent wall flows*. PhD thesis, Politecnico di Milano, 2009.

[MKSK06] T. Min, S.M. Kang, J.L. Speyer, and J. Kim. Sustained sub-laminar drag in a fully developed channel flow. *J. Fluid Mech.*, 558:309–318, 2006.

[OJ94] P. Orlandi and J. Jiménez. On the generation of turbulent wall friction. *Phys. Fluids*, 6(2):634–641, 1994.

[Pop00] S.B. Pope. *Turbulent Flows*. Cambridge University Press, Cambridge, 2000.

[QR04] M. Quadrio and P. Ricco. Critical assessment of turbulent drag reduction through spanwise wall oscillation. *J. Fluid Mech.*, 521:251–271, 2004.

[QR11] M. Quadrio and P. Ricco. The laminar generalized Stokes layer and turbulent drag reduction. *J. Fluid Mech.*, 667:135–157, 2011.

[QRV09] M. Quadrio, P. Ricco, and C. Viotti. Streamwise-traveling waves of spanwise wall velocity for turbulent drag reduction. *J. Fluid Mech.*, 627:161–178, 2009.

[QS00] M. Quadrio and S. Sibilla. Numerical simulation of turbulent flow in a pipe oscillating around its axis. *J. Fluid Mech.*, 424:217–241, 2000.

[Qua11] M. Quadrio. Drag reduction in turbulent boundary layers by in-plane wall motion. *Phil. Trans. R. Soc. A*, 369(1940):1428–1442, 2011.

[Rob91] S. K. Robinson. Coherent motions in the turbulent boundary layer. *Ann. Rev. Fluid Mech.*, 23:601–639, 1991.

[RW04] P. Ricco and S. Wu. On the effects of lateral wall oscillations on a turbulent boundary layer. *Exp. Therm. Fluid Sci.*, 29(1):41–52, 2004.

[Sch06] G. Schrauf. Key Aerodynamic Technologies for Aircraft Performance Improvement. In 5th Community Aeronautics Days, 2006.

[SH00] W. Schoppa and F. Hussain. Coherent structure dynamics in near-wall turbulence. *Fluid Dyn. Res.*, 26:119–139, 2000.

[SJA02] W. Shyy, B. Jayaraman, and A. Andersson. Modelling of glow discharge-induced fluid dynamics. *Journal of Applied Physics*, 92(11):6434–6443, 2002.

[TL12] E. Touber and M.A. Leschziner. Near-wall streak modification by spanwise oscillatory wall motion and drag-reduction mechanisms. *J. Fluid Mech.*, 693:150–200, 2012.

[Vir75] P.S. Virk. Drag reduction fundamentals. *AIChE Journal*, 21:625–656, 1975.

[WC11] R.D. Whalley and K.-S. Choi. Turbulent boundary-layer control with spanwise travelling waves. In *Journal of Physics: Conference Series*, volume 318, 2011.

[WC12] R.D. Whalley and K.-S. Choi. The starting vortex in quiescent air induced by dielectric-barrier-discharge plasma. *J. Fluid Mech.*, 703:192–203, 2012.

[WCF$^+$13] J.-J. Wang, K.-S. Choi, L.-H. Feng, T.N. Jukes, and R.D. Whalley. Recent developments in DBD plasma flow control. *Prog Aerospace Sciences*, 62:52–78, 2013.

[WM08] X. Wu and P. Moin. A direct numerical simulation study of the mean velocity characteristics in turbulent pipe flow. *J. Fluid Mech.*, 608:81–112, 2008.

[XH05] C.-X. Xu and W.-X. Huang. Transient response of Reynolds stress transport to spanwise wall oscillation in a turbulent channel flow. *Phys. Fluids*, 17(018101):1–4, 2005.

[ZWL04] H. Zhao, J.-Z. Wu, and J.-S. Luo. Turbulent drag reduction by traveling wave of flexible wall. *Fluid Dyn. Res.*, 34:175–198, 2004.